Study of Nonlinear Dynamics of Intense Charged Particle Beams in the Paul Trap Simulator Experiment

Hua Wang

A Dissertation

Presented to the Faculty

of Princeton University

in Candidacy for the Degree

of Doctor of Philosophy

Recommended for Acceptance

by the Department of

Astrophysical Sciences Program in Plasma Physics

Adviser: R. C. Davidson

November 2014

Abstract

The Paul Trap Simulator Experiment (PTSX) is a compact laboratory device that simulates the nonlinear dynamics of intense charged particle beams propagating over a large distance in an alternating-gradient magnetic transport system. The radial quadrupole electric field forces on the charged particles in the Paul Trap are analogous to the radial forces on the charged particles in the quadrupole magnetic transport system. The amplitude of oscillating voltage applied to the cylindrical electrodes in PTSX is equivalent to the quadrupole magnetic field gradient in accelerators. The temporal periodicity in PTSX corresponds to the spatial periodicity in magnetic transport system. This thesis focuses on investigations of envelope instabilities and collective mode excitations, properties of high-intensity beams with significant space-charge effects, random noise-induced beam degradation and a laser-induced-fluorescence diagnostic.

To better understand the nonlinear dynamics of the charged particle beams, it is critical to understand the collective processes of the charged particles. Charged particle beams support a variety of collective modes, among which the quadrupole mode and the dipole mode are of the greatest interest. We used quadrupole and dipole perturbations to excite the quadrupole and dipole mode respectively and study the effects of those collective modes on the charge bunch. The experimental and particle-in-cell (PIC) simulation results both show that when the frequency and the spatial structure of the external perturbation are matched with the corresponding collective mode, that mode will be excited to a large amplitude and resonates strongly with the external perturbation, usually causing expansion of the charge bunch and loss of particles. Machine imperfections are inevitable for accelerator systems, and we use random noise to simulate the effects of machine imperfection on the charged particle beams. The random noise can be Fourier decomposed into various frequency components and experimental results show that when the random noise has a large frequency component that matches a certain collective mode, the mode will also be excited and cause heating of the charge bunch. It is also noted that by rearranging the order of the random noise,

the adverse effects of the random noise may be eliminated. As a non-destructive diagnostic method, a laser-induced-fluorescence (LIF) diagnostic is developed to study the transverse dynamics of the charged particle beams. The accompanying barium ion source and dye laser system are developed and tested.

Acknowledgements

First of all, I would like to thank my thesis advisor, Professor R. C. Davidson, whose deep physical insights and tremendous experience constantly guided me through this work. He provided me with a unique opportunity of working on a variety of interesting projects in the areas of beam physics, and taught me the invaluable skills of multitasking. He is a great mentor, as well as a wonderful friend. His outstanding work ethic set an example for me to follow. I am also greatly thankful to Erik Gilson for the pleasure of working with and learning from him. I have benefitted enormously from his brilliant scientific intuition and his broad range of knowledge. He taught me tremendous experiment skills and I can't thank him enough for devoting time to the reading of this thesis, and providing constructive suggestions. I am also greatly indebted to Andy Carpe, a fantastic technician and a lifelong friend. It was impossible to finish this thesis without his excellent technical support and congenial conversations. I am also grateful to Dick Majeski for his scientific expertise and devoting time to the reading of my thesis.

I also extend my gratitude to Barbara Sarfaty for her tireless effort on making my stay in PPPL an enjoyable experience. I would like to offer my sincere thanks and appreciation to Hong Qin for his continuous interest in my research, as well as his encouragement and strong support.

It was a pleasure to be a member of the Beam Physics and Nonneutral Plasma Division of PPPL. In addition to Ron, Erik and Hong, i would like to acknowledge other past and present group members. I am grateful to Edward Starsev for the fruitful discussions about beam dynamics. I would like to thank Mikhail Dorf for his insightful suggestions during my learning of the Warp 3D code. I also extend my heartfelt gratitude to Moses Chung for his constant encouragement and strong support in my research. Finally, I also learned a lot from Phil Efthimion, Larry Grisham who shared scientific expertise at group meetings.

My years at Princeton were made more pleasant by my fellow graduate students, Martin, Katie, Anton, Clayton, Paul, Filippo, John, who were always there for cheerful talks. Special

thanks go to my former officemates Erik Grandstedt and Eisung Yoon for their spiritual support.

Finally, this work is impossible to be finished without the unconditional love and support from my family: my parents, Yuexiu and Zhiwu, my sister Liqin, to all of whom I dedicate this thesis.

Dedicated to

Yuexiu Zeng,

Zhiwu Wang,

Yiqiao Tang,

and Liqin Zeng,

for their unconditional love and support.

Contents

List of Tables

List of Figures

Chapter 1

Introduction

An improved understanding the dynamics of intense charged particle beams would have a great impact on the design and stable operation of the next-generation of high-intensity accelerators and beam transport systems [1]. In this thesis, the Paul Trap Simulator Experiment (PTSX) is used to experimentally study charged particle beams with strong space-charge fields [2–12]. The PTSX apparatus is a cylindrical compact Paul trap [13] used to simulate the transverse dynamics of intense charged particle beams in alternating-gradient transport systems [14] based on the analogy between intense charged particle beams propagating in the magnetic transport system and the nonneutral plasma confined in the Paul trap configuration [15]. The PTSX device consists of one two-meter long central cylindrical electrode and two short 40-cm long cylindrical electrodes at each end of the central electrode. Each cylinder is sliced into four azimuthal 90° sectors. The charge bunch is confined transversely by applying oscillating voltage $\pm V(t)$ on the central electrodes. A DC positive bias voltage, $+\hat{V}$, applied to the short electrodes, confines the charge bunch axially.

1.1 Nonneutral Plasma VS. Intense Charged Particle Beams

1.1.1 Nonneutral Plasma

A nonneutral plasma is a many-body collection of charged particles in which there is not overall charge neutrality [16]. Like electrically neutral plasmas [17–25], nonneutral plasmas shield electric fields on a scale of the Debye length (Debye shielding) [18] and support various collective motions of the charged particles such as plasma oscillations, plasma waves, and instabilities [12]. However, there are inherent differences between electrically neutral plasmas and nonneutral plasmas. Nonneutral plasmas are characterized by intense self-electric fields, and, in high-current configurations, by intense self-magnetic fields [16]. Moreover, the intense self fields in a nonneutral plasma can have a large influence on detailed plasma behavior and stability properties [16]. Experimental studies of the basic equilibrium and stability properties of nonneutral plasmas have ranged from investigations of plasma waves in a pure electron plasma [26], to studies of plasma waves in a pure ion plasma column [27], to the identification of collective modes in a two-dimensional, nonneutral ion layer confined below a liquid-helium suface [28,29], to observations of the transport of magnetically confined pure electron plasmas to global thermal equilibrium [30], to mention a few examples. Experimental devices for the study of nonneutral plasmas include Malmberg-Penning traps [26,31] for investigation of basic plasma properties (e.g. precision measurement of the magnetic moment of the antiproton), and Paul Traps which can be used as a mass spectrometer, and can be utilized to trap antimatter such positrons and antiprotons for the basic atomic and molecular physics and gamma-ray astronomy [32].

Theoretical studies of the basic equilibrium, stability and transport properties of nonneutral plasmas have ranged from analytical investigations of the influence of intense self fields on the filamentation instability [33], to development of a confinement theorem for a low-density nonneutral plasma column [34], to quasilinear studies of the nonlinear evolution

of the diocotron instability for multimode excitation in a nonneutral electron layer [35], to determination of the influence of intense self fields on the cyclotron maser instability in a relativistic, nonneutral electron beam [36].

1.1.2 Intense Charged Particle Beams

A charged particle beam is defined as a many-body collection of charged particles propagating in nearly same direction with nearly the same speed [1, 37]. A charged particle beam propagating in a periodic alternating-gradient magnetic transport system has a wide range of applications such as basic scientific research in high energy and nuclear physics, heavy ion fusion, spallation neutron sources, tritium production, nuclear waste treatment, and high-gain X-ray free electron lasers [1, 38–40]. Of particular importance, for purpose of designing high intensity charged particles beams for the present and the next-generation accelerators and transport systems, are the effects of strong self fields produced by the beam space charge and current on determining the detailed equilibrium, stability and transport properties, and the nonlinear dynamics of the system [1]. Both intense charged particle beams and nonneutral plasmas [16] exhibit a broad range of collective phenomena, such as plasma waves and instabilities.

Many theoretical models have been developed to improve the theoretical understanding collective processes that affect intense beam propagation through periodic focusing systems [41–50]. One important statistical framework for describing the intense beam propagation is based on the nonlinear Vlasov-Maxwell equation. This kinetic model describes the self-consistent nonlinear evolution of the beam distribution function $f_b(\mathbf{x}, \mathbf{p}, t)$ in the six-dimensional phase space $(\mathbf{x}, \mathbf{p})$ as the beam particles interact with the focusing field and the self-generated electric and magnetic fields, $\mathbf{E}^s(\mathbf{x}, t)$ and $\mathbf{B}^s(\mathbf{x}, t)$, produced by the beam space charge and current. Through analytical studies based on the nonlinear Vlasov-Maxwell equations [51–56], and numerical simulations using particle-in-cell (PIC) models and nonlinear perturbative simulations techniques (e.g. 3D Warp code) [57–61], considerable progress

has been made in developing an improved understanding of the collective progresses and nonlinear beam dynamics of high-intensity beam propagation in periodic and uniform focusing systems. The nonlinear Vlasov-Maxwell framework constitutes a complete theoretical description of the nonlinear dynamics and collective processes in intense charged particle beams, and is extremely useful in describing phenomena depending on detailed properties of $f_b(\mathbf{x}, \mathbf{p}, t)$.

Another important theoretical framework, based on the macroscopic fluid-Maxwell equations [15, 33, 62–65], has been developed over the last few decades, and it is usually applied to investigate collective oscillations and instabilities driven by pressure anisotropy. Such a macroscopic model treats the charged particle beams as a fluid, and follows the nonlinear evolution of the macroscopic beam properties including the number density of beam particles, $n_b(\mathbf{x}, t) = \int d^3p f_b(\mathbf{x}, \mathbf{p}, t)$, and the average flow velocity, $\mathbf{V}_b(\mathbf{x}, t) = \left(\int d^3p f_b\right)^{-1} \int d^3p \mathbf{v} f_b(\mathbf{x}, \mathbf{p}, t)$, where $\mathbf{v} = \mathbf{p}/\gamma m_b$ is the velocity and $\gamma = (1 + \mathbf{p}^2/m_b^2c^2)^{1/2}$ is the relativistic mass factor. The effects of heat flow are generally neglected to achieve the closure of the coupled fluid equations. Compared to the kinetic model, the macroscopic model is simpler but contains less information, such as detailed information regarding the beam distribution function in phase space. However, a macroscopic fluid model proves useful in providing insights into collective processes occurring in intense charged particle beams.

1.1.3 Analogy Between Nonneutral Plasmas and Charged Particle Beams

The physics of charged particle beams is analogous to the physics of nonneutral plasmas, since in the reference frame of the charged particle beams, a charged particle beam can be considered as a nonneutral plasma. They both exhibit a broad range of collective phenomena, such as plasma waves and instabilities. The study of intense charged particle beams includes using many theoretical models and techniques developed for investigation of noneu-

tral plasmas [1]. By comparing the Hamiltonians for the transverse particle motion in both charged particle beams and nonneutral plasmas, R. C. Davidson *et al.* have shown that the transverse dynamics of an intense charged particle beam propagating through a periodic focusing qudrupole magnetic field (see Sec. 2.2.1) is fully equivalent to the transverse dynamics of a nonneutral plasma trapped in an oscillating quadrupole electric field [15], such as a pure ion plasma trapped in the a linear Paul Trap (see Sec. 2.2.2). An alternative method of showing the equivalence of the charged particle beams and nonneutral plasmas using Lorentz transformation is discussed in detail in Sec. 2.2.

1.2 Thesis Motivation

Intense charged particle beams propagating through a periodic magnetic transport system have a wide range of applications from basics scientific research in high energy physics and nuclear physics to heavy ion fusion, spallation neutron sources, tritium production, nuclear waste treatment, and high-gain X-ray free electron lasers. Over the last two decades, high intensity charged particle beams have been used extensively in both scientific research and industrial applications [1, 37–40, 66–69]. For example, the Large Hadron Collider (LHC), the world's largest and most powerful particle accelerator, consists of a 27-kilometer circumference ring of superconducting magnets with a number of accelerating structures to boost the energy of the particles. Thousands of magnets of different varieties and sizes are used to direct beams around the accelerator. For these 7 TeV beams, it is critical to have a thorough understanding of the equilibrium, instability and other collective properties of intense charged particle beams propagating long distances with the presence of self-generated electric and magnetic fields. Through analytical investigations based on Vlasov-Maxwell equations and fluid-Maxwell equations, numerical simulations using particle-in-cell (PIC) models and nonlinear perturbative simulation techniques, advanced beam instrumentations and diagnostics [70,71], considerable progress has been made in improving the understanding

of the collective process and the nonlinear beam dynamics of the charged particle beams. However, due to the lack of experimental devices dedicated to fundamental beam property studies, those theoretical and simulation results are hard to verify in order to apply them to the design of new accelerators with confidence. There are also many limitations for existing accelerators and in terms of high operating cost, limited beam time and beam parameter range. An alternative effective method to study the charged particle beam properties is urgently needed.

Over the last few decades, some well known devices have been developed to study the fundamental beam properties in general, or for specific beam applications. These include the University Maryland Electron Ring (UMER) [72], the Spallation Neutron Source (SNS) at Oakridge National Laboratory, Neutralized Drift Compression Experiment (NDCX) at Lawrence Berkeley National Laboratory [73], and the Paul Trap Simulator Experiment (PTSX) at the Princeton Plasma Physics Laboratory [14]. UMER and PTSX provide research opportunities for fundamental studies of collective processes on long time scales such as beam mismatch, beam halo formation, and emittance growth. SNS is a user facility focusing on the beam application. UMER, SNS, and NDCX are all laboratory-frame experiments, while PTSX is a beam-frame experiment based on the equivalence between an charged particle beam and a trapped nonneutral pure ion plasma. The following section will present some highlights of each experiment.

1.3 Overview of Intense Beam Experiments

1.3.1 University of Maryland Electron Ring (UMER)

The University of Maryland Electron Ring (UMER) is a low-energy, high current recirculator for beam physics research [72] using nonrelativistic ($\sim$10 keV) electron beam created within a Pierce-type thermionic gun. Beams with a broad range of intensities and initial conditions circulate many times around the ring. UMER is an extremely versatile platform

with a beam current of up to 100 mA and a pulse length as long as 100 ns. The beam current profiles are adjustable in both space and time. Intercepting and nonintercepting diagnostic equipment is in position, every 20° of the ring, which allows time-resolved measurements of position, beam current density, and emittance. The UMER electron beam is created with a Pierce-type thermionic gun. The total current may be adjusted by the use of apertures placed in a rotating wheel adjacent to the anode. The beam shape, quality and duration may be modified via the gun electronics, i.e., the applied high-voltage pulse or grid bias. Custom beam current density profiles can be easily created, and each of these custom beams requires its own matching and steering solution. The beam is controlled in the recirculating ring with a regular lattice of 35 dipole and 72 quadrupole magnets mounted as shown in Fig. 1.1. Fourteen ring chambers are mounted in UMER. Four quadrupoles (Q), equivalent to two focusing/defocusing (FODO) periods, and two dipoles (D) are on each chamber. Thus, there are 36 full FODO quadruple lattice periods in total. Each dipole provides a nominal 10° of bend to keep the beam traveling around the ring. The quadrupole magnets are wired to allow independent control of any of the four individual magnetic pole faces for scanning purposes. In addition, Helmholtz coils have been mounted on each ring chamber to cancel the horizontal component of the earth's magnetic field. Additionally, the conventional measure of the space charge effect on the beam, the normalized intensity χ (or equivalently $\hat{s}$ defined in the next section), which is the ratio of the space-charge force to the external focusing force, introduced in [38], varies from 0.2 to 0.9 for UMER, which covers the range from the emittance-dominated regime to the space-charge-dominated regime. It is noted that χ ranges from 0 to 1, with 0 corresponding to emittance-dominated regime and 1 corresponding to space-charge-dominated regime. Research topics investigated on UMER include transverse beam dynamics (matching, halo formation, strongly asymmetric beams, space-charge waves, etc.), longitudinal dynamics (bunch capture/shaping, evolution of energy spread, longitudinal space-charge waves, etc.), beam diagnostics development, and computer simulation benchmarking and refinement. Modeling of heavy-ion-fusion (HIF-relevant longitudinal dy-

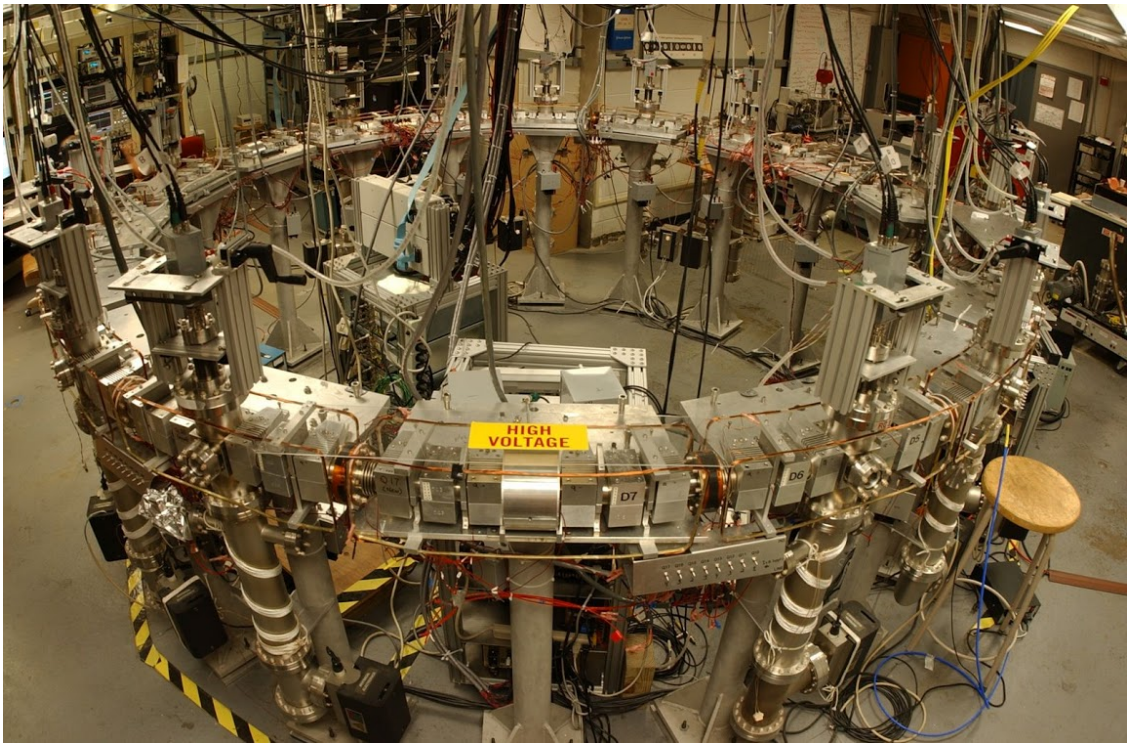

Figure 1.1: An electron beam is injected into the 36-FODO lattice circulation ring of UMER.

namics was carried out in UMER and the results have shown that the longitudinal self-fields in these intense beams are continually evolving. A particle-in-cell (PIC) simulation code has shown excellent agreement [74] with experimental measurements and allows them to develop the necessary experimental hardware needed to generate waveforms to longitudinally shape real beams [75–77]. The first experimental observation of soliton wave trains on an electron beam resulting from deliberately introducing large-amplitude density perturbations has also been reported [78].

1.3.2 Spallation Neutron Source (SNS)

The Spallation Neutron Source (SNS) is a one-of-a-kind research facility that provides the most intense pulsed neutron beams in the world for scientific research and industrial development. SNS produces neutrons with an accelerator-based system that delivers short (microsecond) proton pulses to a target/moderator system, where neutrons are produced by

a process called spallation. With its more intense, brighter source of neutrons and world-class instrumentation, SNS provides the neutron scattering community with unprecedented research opportunities. SNS allows for measurements of greater sensitivity, higher speed, higher resolution, and in more complex sample environments than have been possible at other neutron facilities. The SNS consists of an ion source, a linear accelerator, a proton accumulator ring, target and instrument stations shown in Fig. 1.2. The ion source produces negative hydrogen (H^-) ions that are formed into a pulse beam and accelerated to an energy of 2.5 MeV, then delivered to a large linear accelerator. The linear accelerator accelerates the H^- beam from 2.5 MeV to 1000 MeV by a series of normal-conducting and superconducting radio-frequency cavities that accelerate the beam and a magnetic lattice that provides focusing and steering. Diagnostic elements provide information about the beam current, shape and timing, as well as other information necessary to ensure that the beam is suitable for injection into the accumulator ring and to allow the high-power beam to be controlled safely. The accumulator ring structure bunches and intensifies the ion beam for delivery onto a mercury target to produce the pulsed neutron beams. Inside the target vessel, when a high-energy proton hits the nucleus of a mercury atom, 20 to 30 neutrons are "spalled" or thrown off. Those neutrons are guided out of the target vessel into beam guides that lead directly to instrument stations. The neutrons are slowed down by passing them through cells filled with water or through containers of liquid hydrogen at a temperature of 20 K. The pulsed, moderated neutrons are guided through a beam tube to specially designed instrument stations. The SNS has been used by researchers all over the world across a broad range of disciplines, such as physics, chemistry, material science, and biology [79–81]. A better understanding of the beam equilibrium and stability properties in the linear accelerator has direct impact on the neutron source quality.

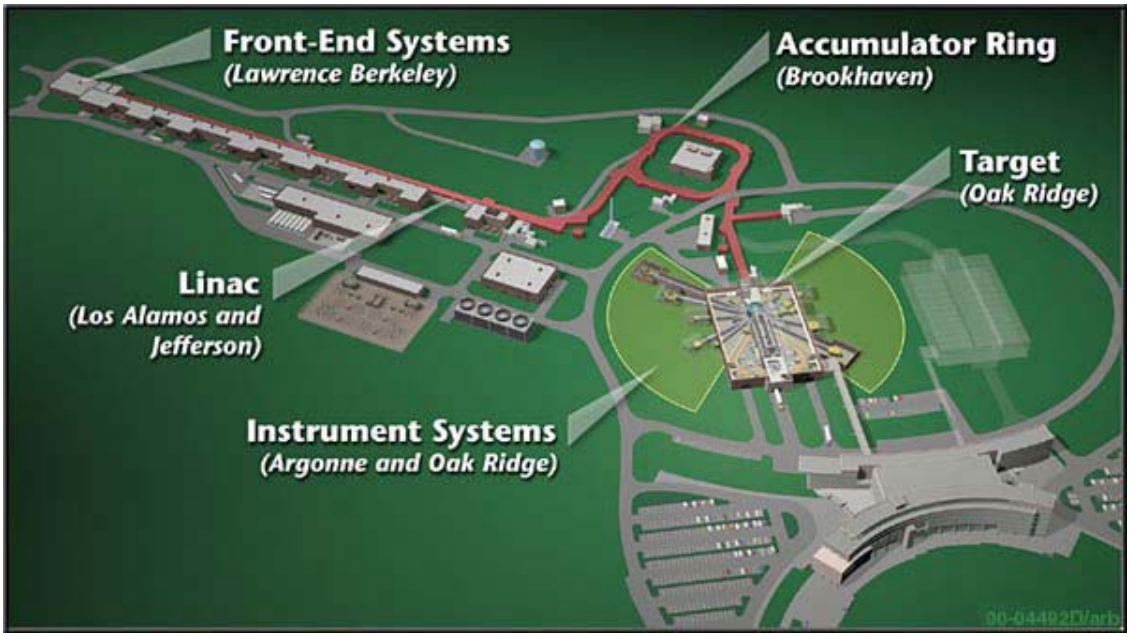

Figure 1.2: Conceptual layout of the SNS facility. At full power, SNS will deliver 1.4 million watts (1.4 MW) of beam power onto the target. SNS was designed from the start with the flexibility to provide additional scientific output in the future by increasing the power output to 3 MW and by the addition of a second target station.

1.3.3 Neutralized Drift Compression Experiment (NDCX-II)

The Neutralized Drift Compression Experiment (NDCX-II) is a new induction accelerator facility designed to facilitate user experiments in high energy density laboratory physics, intense beam physics, and materials processing and testing with intense, pulsed ion beams [82] shown in Fig. 1.3. It is the successor of NDCX-I. For more information about NDCX-I, see Roy et.al [83]. The injector, 27-cell solenoid transport lattice, induction accelerator modules and nonneutral pulse compression section produce space-charge-dominated Li^+ beams carrying 20-50 nC. These beams start as 133 kV pulsed, $\sim$ 1.0 microsecond (FWHM), 65-mA beams from the injector, and are compressed to 20-30 ns with 0.75-1.3 A peak currents and amplification factors of 10-20. The 27-cell beamline consists of 21 identical induction cells and 6 diagnostic cells. Only 7 of the induction cells are active, with the remaining inactive cells having only transport solenoids providing drift length for longitudinal compression for those commissioning exercises. The 7 active induction cells function to impress

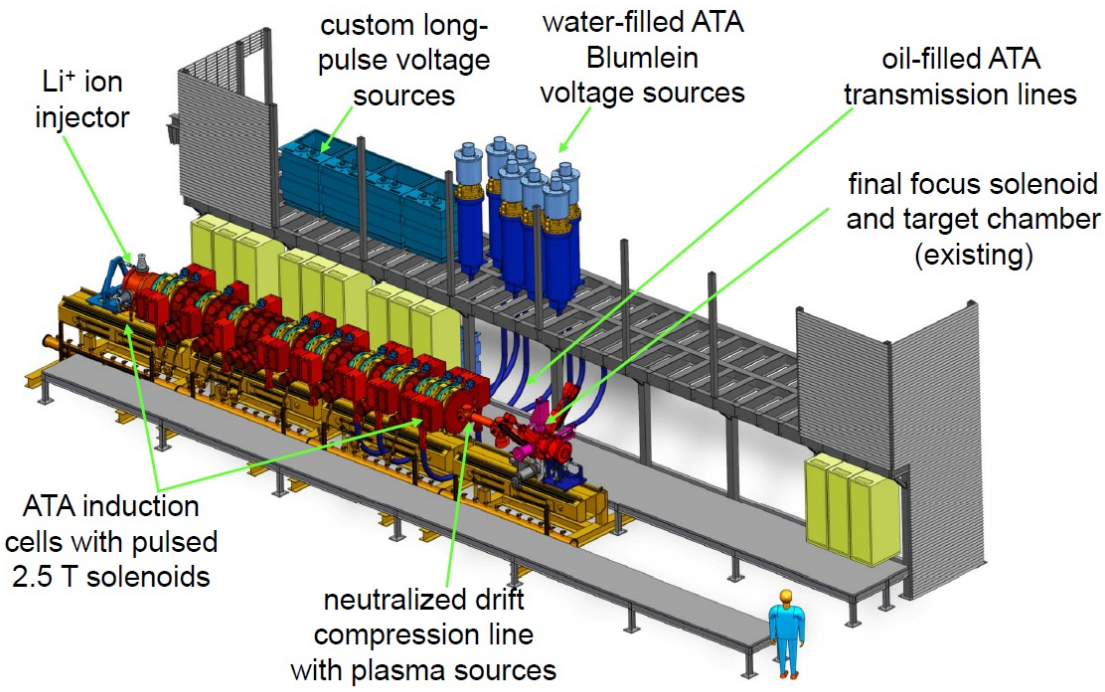

Figure 1.3: Schematic of NDCX-II [84].

a time-varying energy (or velocity) ramp on the beam and, with the additional drift lengths between them, to allow the beam to compress longitudinally with concurrent increase in the peak current. During initial acceleration, the overall pulse length shortens to less than 70 nanoseconds. After further acceleration, the pulse enters a drift tube filled with plasma, which neutralizes the mutually repulsive charge of the positive ions and allows the pulse the compress, as its faster-moving tail closes the final distance to the head while focusing on the target. This process of neutralized drift compression gives the machine its name. By utilizing neutralized drift compression, the beam is optimized to deposit most of its energy in the thin target, heating it rapidly to warm dense matter conditions. Recent experiments on NDCX-II include examining the pulse length and peak fluence dependence on lattice defect generation and recovery in single crystal silicon and metals, as well as utilizing a thin (1 μm) single crystal silicon (100) membrane to intercept the beam. The membrane thickness is chosen to block the randomly scattered ions while allowing the channeled ion flux to pass. See Schenkel *et.al* [82] for detailed discussion.

1.3.4 Paul Trap Simulator Experiment (PTSX)

The Paul Trap Simulator Experiment (PTSX) at Princeton Plasma Physics Laboratory (PPPL) is a compact linear Paul trap that simulates the collective processes and nonlinear transverse dynamics of intense charged particle beams propagating through a periodic focusing quadrupole magnetic field shown in Fig. 1.4. The idea of using PTSX to study beam dynamics was proposed by Davidson *et al.* [15]. The equivalence between charged particle beams and pure ion plasmas confined in PTSX is discussed in detail in **Chapter 2**. Initial experiments carried out by Gilson *et al.* have successfully demonstrated quiescent beam propagation over equivalent distances of tens of kilometers, and accessing a wide operating range with stable confinement of the charge bunch [14]. A radially scanned charge collector was used to the measure the radial density profiles of the plasmas, and the experimental results were in good agreement with a simple force balance model [1], for a wide range of system parameters. Values of the normalized intensity parameter $\hat{s} = \omega_p^2(0)/2\omega_q^2$ up to 0.8 were achieved, where $\omega_p(r)$ is the local plasma frequency and ω_q is the average smooth focusing frequency [1]. Like χ in UMER, the normalized intensity parameter $\hat{s}$ indicates where the beam is emittance dominated ($\hat{s} \ll 1$) or space-charge dominated ($\hat{s} \to 1$). Details of the PTSX configuration and the diagnostic tools will be discussed in **Chapter 3**.

1.4 Thesis Outline

This thesis focuses on the investigation of the transverse dynamics of the charged particle beams. **Chapter 2** presents the derivation of the Lorentz transformations of the external focusing field and self-generated electric and magnetic fields by the charged particle beams from the laboratory frame to the beam frame. The equivalence between the Paul trap configuration and the charged particle beams is discussed in detail, including a discussion of the limitations of the analogy. In support of the experimental data obtained from PTSX, several beam dynamics models are presented. Single-particle orbits are first introduced, with

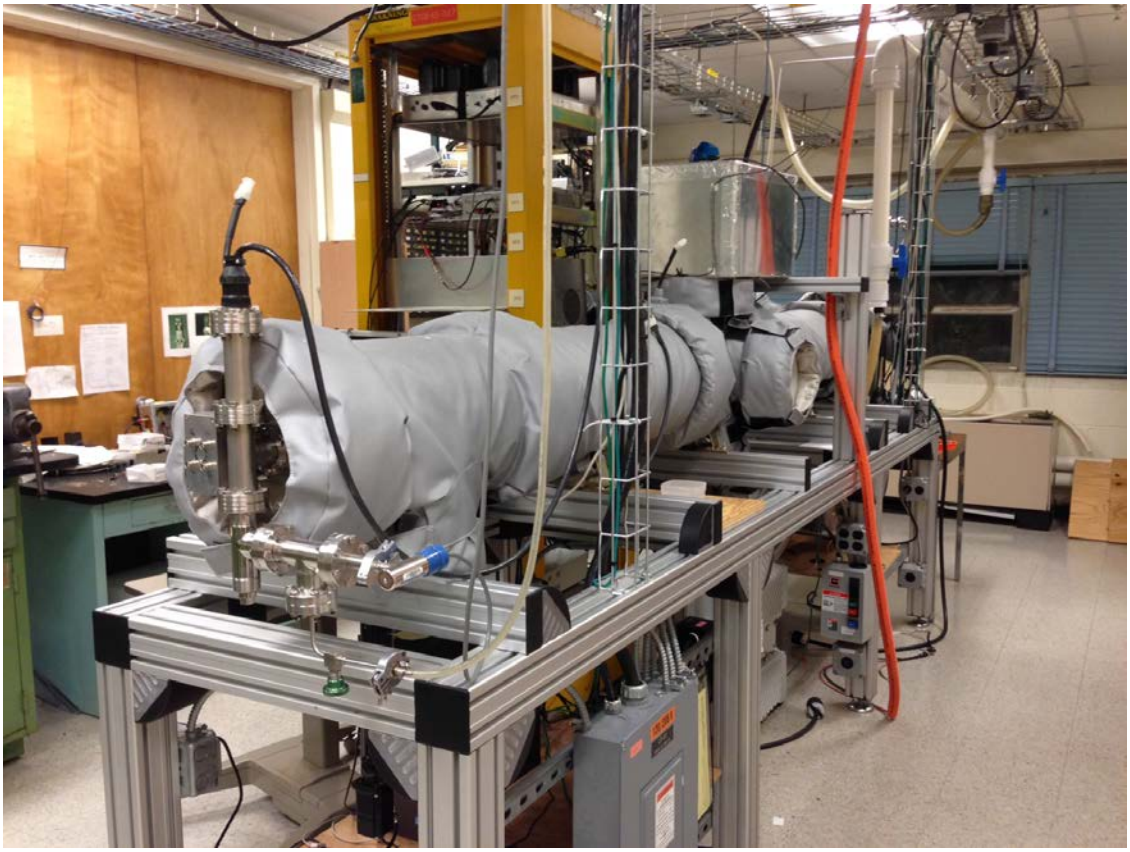

Figure 1.4: The PTSX device consists of one 2m long central cylinder and two 40cm long end cylinders.

a brief discussion of the smooth focusing model. To describe an ensemble of particles, the envelope equations derived using the Kapchinskij-Vladimirskij (KV) distribution function are presented. The beam equilibrium is presented in the smooth-focusing approximation, and the corresponding global force balance equation is derived accordingly.

Chapter 3 gives a complete description of the PTSX apparatus. A detailed description of the PTSX electrodes, the cesium ion source, the vacuum system, and the electrode control system is presented. The operation of the PTSX device is described, together with the characteristic operating parameters. The cesium ion source which is used for most of the experiments conducted in the PTSX device is described in detail. The design and the data collecting mechanism of the radially scanning charge collector is presented. The charge collector has successfully measured the radial charge density profiles with measurement res-

olution as low as 1 fC range, which is sufficient enough to detect the formation of halo particles. As a non-destructive diagnostic, the design of the laser-induced-fluorescence (LIF) diagnostic is presented, as well as the development of the accompanying barium ion source.

Chapter 4 addresses the investigation of collective processes of charged particle beams and their interaction with the external perturbations. The excitation of quadrupole and dipole modes is studied experimentally and the experimental data are compared with the particle-in-cell (PIC) simulation results and the theoretical results using the simple Kapchinskij-Vladimirskij (KV) smoothing focusing model. It is demonstrated that, in order to see a significant resonance effect, not only does the frequency of the external perturbation need to match the mode frequency, but also the spatial structure of the external perturbation must match the collective mode structure. The effects of machine imperfection such as random noise are discussed extensively. It is shown that the random noise will cause beam degradation in general, and some effective measures can be taken to prevent these negative effects.

Chapter 5 presents the development of the laser-induced-fluorescence (LIF) diagnostic and the accompanying new barium source. An overview of the LIF system is presented, including the excimer and the dye laser system, the laser coupling and transmission system, the barium ion source and the CCD camera system. It is demonstrated that the combination of an excimer laser and a dye laser is able to provide the laser light for LIF measurements. The design and the test of the barium ion source is discussed in detail. The initial test results of the ion source have verified its ability to provide a stable and high-density pure ion plasma. The test results of the laser system are presented, together with the initial results on reconstructing the radial density profiles using the LIF diagnostics.

Chapter 6 summarizes the thesis work and proposes interesting topics for future research.

Chapter 2

Theoretical Background

2.1 Introduction

Periodic focusing transport systems have a wide range of applications ranging from basic scientific research in high energy and nuclear physics to applications such as nuclear-waste treatment, neutron spallation source, heavy ion fusion. Understanding the nonlinear dynamics of the intense charged particle beams with strong space-charge effects is of great importance. Thanks to the equivalence of the transverse dynamics between the intense charged particle beams in a periodic focusing transport system and the long thin non-neutral plasma bunch in the Paul Trap Simulation Experiment (PTSX), we can use PTSX to study the beam dynamics of the charged particle beams.

In Sec. 2.2, we present a brief discussion of the analogy of the transverse dynamics in the periodic focusing transport system to that in PTSX from the perspective of a Lorentz transformation. It is shown that when the laboratory reference frame is transferred to the beam reference frame, the forms of the electromagnetic forces on the charged particles in the periodic transport system are equivalent to those on the plasma bunch in PTSX. In Sec. 2.3, the orbits of a single particle and the envelope equations are briefly reviewed. It is shown that the single particle orbit can be seen as a combination of a slow smooth-focusing motion

and a fast motion when the phase advance is small enough. Envelope equations are used to describe the evolution of the transverse beam envelopes and they provide significant insights in understanding the collective processes of the charged particle beams. Sec. 2.4 gives a brief summary and discussion of this chapter.

2.2 Paul Trap Simulator Experiment (PTSX)

In this section, we present a concise theoretical description that illustrates the equivalence between the Paul trap configuration and intense beam propagation through a periodic magnetic quadrupole focusing field.

2.2.1 Intense Charged Particle Beams

We consider an intense charged particle beam consisting of a single charge species propagating in the z-direction with average axial velocity $V_b = \beta_b c$ through a periodic magnetic quadrupole focusing field, and characteristic directed kinetic energy $(\gamma_b - 1)m_b c^2$ in the laboratory frame. Here m_b is the rest mass of a beam particle, c is the speed of light *in vacuo*, $\gamma_b = (1 - \beta_b^2)^{-1/2}$ is the relativistic mass factor.

Before we move on to discuss the physics of the intense charged particle beam and the analogy between intense charged particle beams and nonneutral plasma in a Paul Trap configuration, we briefly introduce the Lorentz transformations that relate the time and space coordinates between the two different inertial reference frames.

Consider two inertial reference frames K and K' with a relative velocity $V_b = \beta_b c$ in the z direction between them. The time and space coordinates of a point are (ct, x, y, z) and (ct', x', y', z') in the frames K and K', respectively. Then, the time and space coordinates in K' are related to those in K by [85]

$$
\begin{aligned}
x'_0 &= \gamma_b(x_0 - \beta_b x_3) \\
x'_1 &= x_1 \\
x'_2 &= x_2 \\
x'_3 &= \gamma_b(x_3 - \beta_b x_0),
\end{aligned} \tag{2.1}
$$

where we have introduced the notation $x_0 = ct, x_1 = x, x_2 = y, x_3 = z$. If we define a Lorentz transformation matrix A such that $x_\alpha = A^{\alpha\beta}x_\beta$, the Lorentz transformation matrix A for a specific transformation from frame K to K' is a 4×4 matrix takes the following form:

$$
\begin{pmatrix}
\gamma_b & 0 & 0 & -\gamma_b\beta_b \\
0 & 1 & 0 & 0 \\
0 & 0 & 1 & 0 \\
-\gamma_b\beta_b & 0 & 0 & \gamma_b
\end{pmatrix} \tag{2.2}
$$

The evolution of electromagnetic field is described by the Maxwell equations

$$
\begin{aligned}
\nabla \cdot \mathbf{E} &= \frac{\rho}{\epsilon_0} \\
\nabla \times \mathbf{B} - \frac{1}{c^2}\frac{\partial \mathbf{E}}{\partial t} &= \mu_0 \mathbf{J}
\end{aligned} \tag{2.3}
$$

$$
\begin{aligned}
\nabla \cdot \mathbf{B} &= 0 \\
\nabla \times \mathbf{E} - \frac{\partial \mathbf{B}}{\partial t} &= 0
\end{aligned} \tag{2.4}
$$

If we define two 4-vectors J^α and A^α as

$$\begin{aligned} J^\alpha &= (\mathrm{c}\rho, \mathbf{J}) \\ A^\alpha &= (\frac{\mathbf{\Phi}}{\mathrm{c}}, \mathbf{A}) \end{aligned} \tag{2.5}$$

where $\mathbf{A}$ is the vector potential while $\mathbf{\Phi}$ is the scalar potential, the inhomogeneous Maxwell equations Eq.(2.3) take on the covariant form [85],

$$\partial_\alpha F^{\alpha\beta} = \frac{4\pi}{\mathrm{c}}\mathrm{J}^\beta \tag{2.6}$$

and the homogeneous Maxwell equations Eq.(2.4) can be written as

$$\partial_\alpha \mathcal{F}^{\alpha\beta} = 0 \tag{2.7}$$

where $\mathbf{F}^{\alpha\beta}$ and $\mathcal{F}^{\alpha\beta}$ are the elements of a second-rank, antisymmetric field-strength tensor and a dual field-strength tensor, respectively. $\mathbf{F}^{\alpha\beta}$ is defined as

$$F^{\alpha\beta} = \partial^\alpha \mathrm{A}^\beta - \partial^\beta \mathrm{A}^\alpha \tag{2.8}$$

where $\partial^\alpha = (\partial/\partial x_0, -\nabla)$ and $\mathcal{F}^{\alpha\beta}$ is defined as

$$\mathcal{F}^{\alpha\beta} = \frac{1}{2}\epsilon^{\alpha\beta\gamma\delta}\mathrm{F}_{\gamma\delta} \tag{2.9}$$

where $\epsilon^{\alpha\beta\gamma\delta}$ is the Levi-Civita symbol and $F_{\alpha\beta} = g_{\alpha\gamma}F^{\gamma\delta}g_{\delta\beta}$. The matric tensor $g_{\alpha\beta}$ is a square 4×4 matrix

$$g = \begin{pmatrix} 1 & 0 & 0 & 0 \\ 0 & -1 & 0 & 0 \\ 0 & 0 & -1 & 0 \\ 0 & 0 & 0 & -1 \end{pmatrix} \tag{2.10}$$

Therefore, $\mathbf{F}^{\alpha\beta}$ in matrix form is

$$\mathbf{F}^{\alpha\beta} = \begin{pmatrix} 0 & -E_x/c & -E_y/c & -E_z/c \\ E_x/c & 0 & -B_z & B_y \\ E_y/c & B_z & 0 & -B_x \\ E_z/c & -B_y & B_x & 0 \end{pmatrix} \tag{2.11}$$

and $\mathcal{F}^{\alpha\beta}$ in matrix form is

$$\mathcal{F}^{\alpha\beta} = \begin{pmatrix} 0 & -B_x/c & -B_y/c & -B_z/c \\ B_x/c & 0 & E_z & -E_y \\ B_y/c & -E_z & 0 & E_x \\ B_z/c & E_y & -E_x & 0 \end{pmatrix} \tag{2.12}$$

Since the fields $\mathbf{E}$ and $\mathbf{B}$ are the elements of a second-rank tensor $\mathbf{F}^{\alpha\beta}$, their values in one inertial frame can be expressed in terms of the values in another inertial frame K' according to

$$F'^{\alpha\beta} \;=\; \frac{\partial \mathrm{x}'^{\alpha}}{\partial \mathrm{x}^{\gamma}}\; \mathrm{F}^{\gamma\delta}\; \frac{\partial \mathrm{x}'^{\beta}}{\partial \mathrm{x}^{\delta}} \tag{2.13}$$

In a matrix notation, the above equation can be written

$$\mathbf{F'} \;=\; \mathbf{A}\;\mathbf{F}\;\mathbf{A^T} \tag{2.14}$$

where $\mathbf{F}$ and $\mathbf{F'}$ are 4×4 matrices(2.11) and $\mathbf{A}$ is the Lorentz transformation matrix of. A^T is the transpose of A. For the specific Lorentz transformation(2.2), corresponding to a boost along the z axis with speed $c\beta_b$ from the unprimed frame to the primed frame, the explicit transformation equations are

$$
\begin{aligned}
E_1' &= \gamma\left(E_1 - \beta \mathrm{cB}_2\right) \qquad & B_1' &= \gamma\left(\mathrm{B}_1 + \frac{\beta}{\mathrm{c}}\mathrm{E}_2\right) \\
E_2' &= \gamma\left(E_2 - \beta \mathrm{cB}_1\right) \qquad & B_2' &= \gamma\left(\mathrm{B}_2 + \frac{\beta}{\mathrm{c}}\mathrm{E}_1\right) \\
E_3' &= \mathrm{E}_3 & \mathrm{B}_3' &= \mathrm{B}_3
\end{aligned} \tag{2.15}
$$

(2.16)

Now consider the electric and magnetic fields of an intense charged particle beam propagating in the z-direction with average axial velocity $V_b = \beta_b c$ through a periodic magnetic quadrupole focusing field. We assume a thin beam with $a,\ \mathrm{b} \ll \mathrm{S}$, where S is the axial periodicity of the quadrupole focusing field, a and b are the characteristic $x-$ and $y-$ dimensions of the beam. Under such assumption, we can approximate the continuous thin beam as an infinitely long thin conducting wire carrying current $I = \lambda V_b$, where λ is the electric charge per unit length, in the $z-$ direction. The electric and magnetic fields associated with the conducting wire in the polar coordinate (r, θ, z) can be written

$$
\mathbf{E}(\mathbf{r},\theta)^s = \mathrm{E}_\mathrm{r}^\mathrm{s}\hat{\mathbf{e}}_\mathrm{r} = \frac{\lambda}{2\pi \mathrm{r}\epsilon_0}\hat{\mathbf{e}}_\mathrm{r} \tag{2.17}
$$

$$
\mathbf{B}(\mathbf{r},\theta)^s = \mathrm{B}_\theta^\mathrm{s}\hat{\mathbf{e}}_\theta = \frac{\mu_0 \lambda \mathrm{V_b}}{2\pi \mathrm{r}}\hat{\mathbf{e}}_\theta \tag{2.18}
$$

Then change the polar coordinate to the Cartesian coordinate using $\hat{\mathbf{e}}_r = \cos(\theta)\hat{\mathbf{e}}_x + \sin(\theta)\hat{\mathbf{e}}_y$, $\hat{\mathbf{e}}_\theta = -\sin(\theta)\hat{\mathbf{e}}_x + \cos(\theta)\hat{\mathbf{e}}_y$ and $x = r\cos(\theta)$, $y = r\sin(\theta)$, we readily get

$$
\begin{aligned}
E_x^s &= \frac{\lambda x}{2\pi\left(x^2+y^2\right)\epsilon_0} \qquad & B_x^s &= -\frac{\mu_0 \lambda V_b y}{2\pi\left(x^2+y^2\right)} \\
E_y^s &= \frac{\lambda y}{2\pi\left(x^2+y^2\right)\epsilon_0} \qquad & B_y^s &= \frac{\mu_0 \lambda V_b x}{2\pi\left(x^2+y^2\right)}
\end{aligned} \tag{2.19}
$$

We also note that $B_y^s/E_x^s = V_b/c^2$, $B_x^s/E_y = -V_b/c^2$, making use of $\mu_0\epsilon_0 = \frac{1}{c^2}$. Bear in mind that as the beam particles become more and more energetic, the ratio of self magnetic field to self electric field is getting larger and larger. So far we have done thorough analysis on the self fields due to the charged particle beams. As for the external quadrupole focusing field, consistent with the thin beam assumption ($a, b \ll S$), the external quadrupole field can be Taylor expanded about the beam axis at $(x, y) = (0, 0)$. Near the beam axis, the magnetic quadrupole field is approximated to leading order by [16]

$$\mathbf{B}_q(\mathbf{x}) = B_q'(z)(y\mathbf{e_x} + x\mathbf{e_y}) \tag{2.20}$$

where x and y are the transverse displacement of a particle from the beam axis,and the field gradient coefficient $B_q'(z)$ is defined by

$$B_q'(z) \equiv \left(\frac{\partial B_x^q}{\partial y}\right)_{(x,y)=(0,0)} = \left(\frac{\partial B_y^q}{\partial x}\right)_{(x,y)=(0,0)}, \tag{2.21}$$

and $B_q'(z) = B_q'(z + S)$ has axial periodicity length S.

Then we compare the electric and magnetic fields in the laboratory frame K and those in the beam frame K' which is moving in the positive z direction. And also we only focus on the transverse beam dynamics and currently ignore any axial beam physics. The E and B fields in the K frame are as follow

$$\begin{aligned}
E_x &= E_x^s \qquad B_x = B_x^s + B_q'(s)y = \frac{V_b}{c^2}E_y^s + B_q'(s)y \\
E_y &= E_y^s \qquad B_y = B_y^s + B_q'(s)x = \frac{V_b}{c^2}E_x^s + B_q'(s)x \\
E_z &\approx 0 \qquad \mathrm{B_z} \approx 0
\end{aligned} \tag{2.22}$$

while in the K' frame the E and B fields are

$$
\begin{aligned}
E'_x &= \gamma(E^s_x - V_b B_y) = \gamma\left(\frac{E^s_x}{\gamma^2} - V_b B'_q(s')x'\right) \qquad B'_x = \gamma B'_q(s')y' \\
E'_y &= \gamma(E^s_y + V_b B_x) = \gamma\left(\frac{E^s_y}{\gamma^2} + V_b B'_q(s')y'\right) \qquad B'_y = \gamma B'_q(s')x' \qquad (2.23) \\
E'_z &\approx 0 \qquad B'_z \approx 0
\end{aligned}
$$

Note the E'_x in the beam frame has two components, one is from self fields and the other one is from the external focusing field. And the $\frac{1}{\gamma^2}$ factor in the self fields reflect the fact that the self electric force is canceled out by the self magnetic force. As the beam particles become more and more energetic ($\gamma \to \infty$), the self field becomes negligible. To conclude, in the beam frame K', for the transverse motions of charged particles, the transverse forces decompose to a combination of self fields and quadrupole focusing force. This simplification not only allows us to study the beam dynamics in a much more convenient frame of reference, but also permits us to use the analogy between the physics of intense charged particle beams and that of nonneutral plasma column to study beam dynamics in Paul Trap Simulator Experiment(PTSX) which will be described in the next section.

2.2.2 Paul Trap Configuration

From the previous section, we note that the particle motion in the beam frame is nonrelativistic, and we can use Lorentz transformation to transform the magnetic fields in the laboratory frame into electric fields in the beam frame. This enables us to study the nonlinear transverse beam dynamics in a compact Paul trap configuration [15, 86, 87].

To simulate an axially continuous intense charged particle beam, we consider a long nonneutral plasma column with length $\sim 2L$ and characteristic radius $r_p \ll 2L$, confined axially by applied DC voltages $+\hat{V} = const.$ on end cylinders at $z = \pm L$. The particles constituting the nonrelativistic pure ion plasma have charge q and mass m. With respect to transverse confinement of the particles in the $x - y$ plane, there is no applied axial magnetic

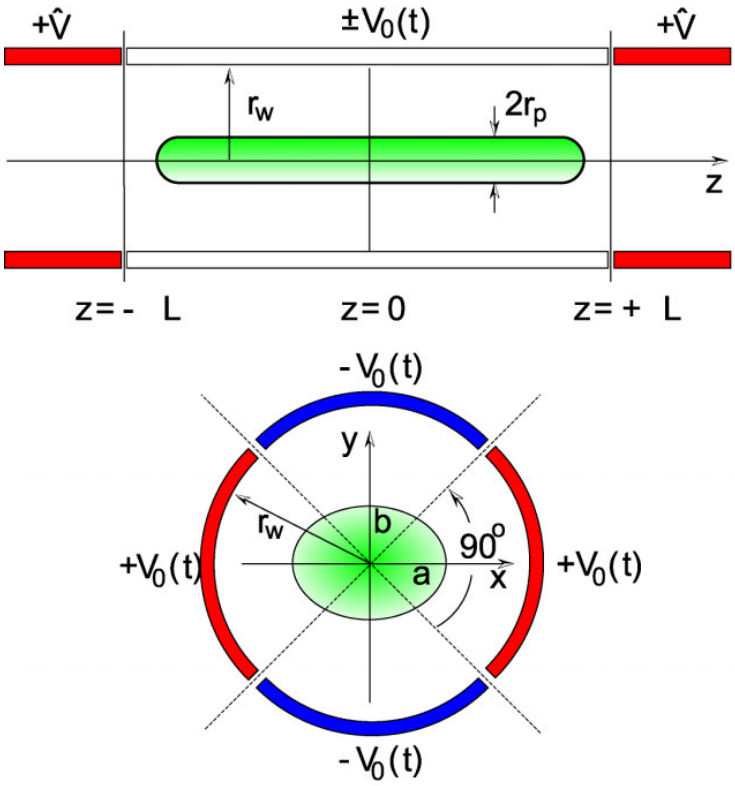

Figure 2.1: (a) Side view and (b) end view of the Paul trap configuration [1].

field ($\mathbf{B}_0 = B_0\hat{\mathbf{e}}_z = 0$). Rather, segmented cylindrical electrodes at radius r_w have applied oscillatory voltage $\pm V_0(t)$ with alternating polarity on adjacent segments. Here, the applied voltage $V_0(t)$ is oscillatory with $V_0(t+T) = V_0(t)$ and $\int_0^T dt V_0(t) = 0$, where $T = const.$ is the period, and $f_0 = 1/T$ is the oscillation frequency. For the typical operating conditions in the Paul trap ($r_w f_0 \ll c$), inductive electromagnetic effects are negligible. Neglecting end effects ($\partial/\partial z = 0$), and representing the applied electric field by $\mathbf{E}_a = -\nabla_\perp \phi_q(x,y,t)$, where $\nabla_\perp \cdot \mathbf{E}_a = 0$ and $\nabla_\perp \times \mathbf{E}_a \simeq 0$, it is readily shown that the solution to $\nabla_\perp^2 \phi_q(x,y,t) = 0$ that satisfies the appropriate boundary conditions at $r = r_w$ is given by [15]

$$\phi_q(x,y,t) = \frac{4V_0(t)}{\pi} \sum_{l=1}^{\infty} \frac{\sin(l\pi/2)}{l} \left(\frac{r}{r_w}\right)^{2l} \cos(2l\theta) \tag{2.24}$$

for $0 \leq r \leq r_w$ and $0 \leq \theta \leq 2\pi$. Near the cylinder axis ($r \ll r_w$), Eq. (2.24) readily gives to lowest order

$$\phi_q(x, y, t) = \frac{1}{2}\frac{m}{q}\kappa_q(t)\left(x^2 - y^2\right), \tag{2.25}$$

where the time-dependent oscillatory quadrupole focusing coefficient $\kappa_q(t + T) = \kappa_q(t)$ is defined by

$$\kappa_q(t) \equiv \frac{8qV_0(t)}{m\pi r_w^2}, \tag{2.26}$$

which has dimensions of $[\mathrm{s}^{-2}]$ (note that the s-dependent focusing coefficient $\kappa_q(s)$ defined in the previous section has dimensions of $[\mathrm{m}^{-2}]$). Most importantly, from Eq. (4.6), the leading-order correction to Eq. (2.25) is of order $(1/3)(r/r_w)^6$. Hence, for sufficiently small r_p/r_w, the quadrupole potential in Eq. (2.25) is a very accurate representation of the applied focusing potential. The external quadrupole electric fields corresponding to Eq.(2.25) are

$$\begin{aligned} E_{qx} &= \frac{m}{q}\kappa_q(t)x \\ E_{qy} &= -\frac{m}{q}\kappa_q(t)y \end{aligned} \tag{2.27}$$

The total transverse electric fields including the self fields would be

$$\begin{aligned} E_x &= E_x^s + \frac{m}{q}\kappa_q(t)x \\ E_y &= E_y^s - \frac{m}{q}\kappa_q(t)y \end{aligned} \tag{2.28}$$

Comparing Eq.(2.28) with Eq.(2.24), we note that the transverse motion of the particles in both configurations are only subject to the electric fields, and both electric fields are a combination of an external quadrupole focusing field and self fields, where self fields can be solved consistently using Maxwell equations. Hence, using the Lorentz transformation, we have shown the analogy between charged particle beams propagating in the quadrupole

transport system and the charge bunch confined in PTSX device. Alternatively, in [88], Dr. Moses Chung analyzed the equivalence of these two systems by comparing Hamiltonians and Vlasov-Maxwell equations for the transverse particle motion. By making the replacement suggested by Table 2.1, he demonstrated that a charged particle beam propagating in a periodic quadrupole focusing system is equivalent to a one-component nonneutral plasma. This analogy between force forms enables us to study the nonlinear transverse dynamics of intense charged particle beams propagating in quadrupole transport systems using our PTSX device.

2.2.3 Limitations of Paul Trap Analogy

As noted earlier, the Paul trap analogy described above is intended to simulate the transverse dynamics of a *continuous* and *thin* beam propagating in a periodic magnetic quadrupole focusing field. Furthermore, we only focus on the the transverse dynamics of the long nonneutral plasma column ($2L \gg r_p$) in Fig. 2.1, and z-variation and axial particle motions are not included in the description. While such a model is expected to provide a good description of the transverse dynamics of the nonneutral plasma column for $2L \gg r_p$, there are important limitations on the range of applicability of the Paul trap analogy for simulating the propagation of a continuous beam through a periodic focusing lattice.

Most importantly, the nonneutral plasma column illustrated in Fig. 2.1 is confined axially, and the particles execute axial bounce motion between the ends of the plasma column (nearly at $z = \pm L$). If we denote the characteristic axial velocity of a particle with axial kinetic energy E_b by $v_b = (2E_b/m)^{1/2}$, then the characteristic bounce time is $\tau_b \sim 4L/v_b$. At low-to-moderate density, the characteristic period τ_q for transverse motion and characteristic plasma radius r_p are approximately related by $\tau_q \sim 2r_p/v_t$, where $v_t = (T_i/m)^{1/2}$ is the thermal speed of ions with temperature T_i. Therefore, in an approximate sense, the transverse and axial oscillation periods stand in the ratio $\tau_q/\tau_b \sim (r_p/2L)(v_b/v_t)$. On a time scale $\tau_q \sim \tau_b$, the finite-length effects of the axial bounce motion of a particle become important, and limit

	Intense relativistic beam	Nonneutral trapped plasma
Time variable	$s = V_b t = \beta_b c t$ [m]	t [s]
Velocity	$x' = \frac{dx}{ds}, y' = \frac{dy}{ds}$ [1]	$\dot{x} = \frac{dx}{dt}, \dot{y} = \frac{dy}{dt}$ [m/s]
Focusing field	$\mathbf{B}_q = B_q'(s)(y\hat{\mathbf{e}}_x + x\hat{\mathbf{e}}_y)$ [T]	$\mathbf{E}_q = -\frac{8V_0(t)}{\pi r_w^2}(x\hat{\mathbf{e}}_x - y\hat{\mathbf{e}}_y)$ [V/m]
Focusing coefficient	$\kappa_q(s) = \frac{q_b}{\gamma_b m_b}\frac{1}{\beta_b^2 c^2} V_b B_q'(s)$ [m^{-2}]	$\kappa_q(t) = \frac{q}{m}\frac{8V_0(t)}{\pi r_w^2}$ [s^{-2}]
Smooth focusing coefficient in sinusoidal lattice with amplitude $\hat{\kappa}_q$	$\kappa_{sf} = \frac{1}{2}\frac{\hat{\kappa}_q^2 S^2}{(2\pi)^2}$ [m^{-2}]	$\kappa_{sf} = \frac{1}{2}\frac{\hat{\kappa}_q^2}{(2\pi)^2 f_0^2}$ [s^{-2}]
Characteristic focusing frequency	$\omega_{\beta\perp} = \beta_b c\sqrt{\kappa_{sf}}$ [s^{-1}]	$\omega_q = \sqrt{\kappa_{sf}}$ [s^{-1}]
Self-field potential	$\psi(x,y,s) = \frac{q_b}{\gamma_b m_b}\frac{1}{\beta_b^2 c^2}\frac{\phi^s(x,y,s)}{\gamma_b^2}$ [1]	$\frac{q}{m}\phi^s(x,y,t)$ [m^2/s^2]
Plasma frequency	$\hat{\omega}_{pb} = \left(\frac{\hat{n}_b q_b^2}{\gamma_b m_b \epsilon_0}\right)^{1/2}$ [s^{-1}]	$\hat{\omega}_p = \left(\frac{\hat{n} q^2}{m\epsilon_0}\right)^{1/2}$ [s^{-1}]
Smooth-focusing vacuum phase advance	$\sigma_v^{sf} = \sqrt{\kappa_{sf}} S$ [1]	$\sigma_v^{sf} = \sqrt{\kappa_{sf}}/f_0$ [1]
Intensity parameter	$s_b = \frac{\hat{\omega}_{pb}^2/\gamma_b^2}{2\omega_{\beta\perp}^2}$ [1]	$\hat{s} = \frac{\hat{\omega}_p^2}{2\omega_q^2}$ [1]
Self-field perveance	$K_b = \frac{1}{4\pi\epsilon_0}\frac{2N_b q_b^2/\gamma_b^2}{\gamma_b m_b \beta_b^2 c^2}$ [1]	$K = \frac{1}{4\pi\epsilon_0}\frac{2Nq^2}{m}$ [m^2/s^2]
Transverse Hamiltonian	$\hat{H}_\perp(x,y,x',y',s) = \frac{1}{2}(x'^2 + y'^2)$ $+\frac{1}{2}\kappa_q(s)(x^2 - y^2) + \psi^s(x,y,s)$ [1]	$\frac{1}{m}H_\perp(x,y,\dot{x},\dot{y},t) = \frac{1}{2}(\dot{x}^2 + \dot{y}^2)$ $+\frac{1}{2}\kappa_q(t)(x^2 - y^2) + \frac{q}{m}\phi^s(x,y,t)$ [m^2/s^2]

Table 2.1: Equations for transverse dynamics of charged particle beams propagating in a periodic focusing quadrupole magnetic system and nonneutral plasmas confined in Paul Trap configuration [88].

the validity of the Paul trap analogy with the propagation of a continuous beam through a periodic focusing lattice. For sufficiently large $2L \gg r_p$ and moderate v_b, however, the axial bounce period τ_b can be very long. As illustrative parameters, consider the case where $r_p = 1$ cm, $2L = 200$ cm, and the frequency $f_0 = 1/T$ of the applied oscillatory voltage $V_0(t)$ is set to $f_0\tau_q \geq 4$ for stability. Further, we assume that particles are injected with axial kinetic energy $E_b = 5$ eV and ion temperature $T_i = 0.1$ eV. In this case, $\tau_b \sim 20\tau_q \sim 80T$. Hence, a typical particle in Fig. 2.1 experiences the effects of 80 oscillation periods of the quadrupole focusing potential (80 equivalent lattice periods) before it executes one axial bounce in the trap.

Another limiting factor of the Paul trap analogy is the effect of collisions. Collisional effects in high-energy beams in actual accelerators and transport lines are often negligible. Therefore, if collisional effects become significant for the nonneutral plasma in the trap, then the Paul trap analogy is no longer valid. The characteristic collision time for scattering of ions by background neutral atom is [89]

$$\tau_{in} \approx \frac{1}{n_n \sigma_s^{in} v_t}, \tag{2.29}$$

where n_n is the average neutral density, and σ_s^{in} is the ion-neutral collision cross section, typically $\sim 5 \times 10^{-15}$ cm^2 and weakly dependent on temperature. If we use the ideal gas law $n_n = P/T_r$, it is estimated that $\tau_{in} > 2$ sec when the base pressure P is kept below 10^{-7} Torr at room temperature $T_r = 300$ K. The characteristic collision time for ions colliding with other ions is given [21]

$$\tau_{ii} \approx \frac{12\pi^{3/2}\epsilon_0^2 m^2 v_t^3}{n_i q^4 \ln\Lambda}, \tag{2.30}$$

where n_i is the average ion density and $\ln\Lambda$ is Coulomb logarithm, to good approximation ~ 14 for the PTSX parameters. For the typical operating conditions for the PTSX, it is estimated that $\tau_{ii} > 0.5$ sec when $n_i < 10^6$ cm^{-3}. Hence, by limiting the trapping time of ions below several hundred milliseconds, we can avoid collisional effects.

2.2.4 Operating Parameters

The detailed transverse motion of individual particles in the PTSX is approximately composed of both a rapid oscillation with frequency f_0 and a slow oscillation with characteristic frequency ω_q. In the *smooth-focusing approximation* [1,16,38], where there is averaging over the rapid motion with frequency f_0, orbit equations with a constant focusing coefficient are often used to describe the average effects of the periodic focusing quadrupole field. The expression for the average focusing frequency ω_q in the smooth-focusing approximation is given by [1]

$$\omega_q = \sqrt{\left\langle \left(\int_{t_0}^{\tilde{t}} dt \kappa_q(t) \right)^2 \right\rangle_T - \left\langle \left(\int_{t_0}^{\tilde{t}} dt \kappa_q(t) \right) \right\rangle_T^2}, \tag{2.31}$$

where $\langle \cdots \rangle_T$ denotes the temporal average over one oscillation period.

$$\langle \cdots \rangle_T (t) = \frac{1}{T} \int_{t-T/2}^{t+T/2} d\tilde{t} \cdots . \tag{2.32}$$

Two illustrative examples of oscillatory waveforms for the quadrupole focusing coefficient $\kappa_q(t) = (8q/m\pi r_w^2)V_0(t)$ are shown in Fig. 2.2. Here, Fig. 2.2(a) corresponds to a sinusoidal waveform with $\kappa_q(t) = \hat{\kappa}_q \sin(2\pi t/T)$, where $\hat{\kappa}_q = (8q/m\pi r_w^2)\hat{V}_0$ and $\hat{V}_0 = |V_0(t)|_{\max}$. This sinusoidal waveform is least taxing on the bandwidth limit of the electronic system of the PTSX device [14] and is an approximation to a quadrupole lattice with short magnets with significant fringe fields. The smooth-focusing frequency for the case of the sinusoidal waveform is given approximately by

$$\omega_q = \frac{8q}{m\pi r_w^2} \left(\frac{\hat{V}_0}{f_0} \right) \frac{1}{2\pi\sqrt{2}}. \tag{2.33}$$

Figure 2.2(b) corresponds to a periodic step-function lattice with maximum amplitude $\hat{\kappa}_q$ and filling factor η. This FODO lattice (Focusing-Off-Defocusing-Off) has hard-edged quadrupole magnets and is an idealization of a magnetic alternating-gradient transport system. The smooth-focusing frequency for the case of a periodic step-function lattice is given approxi-

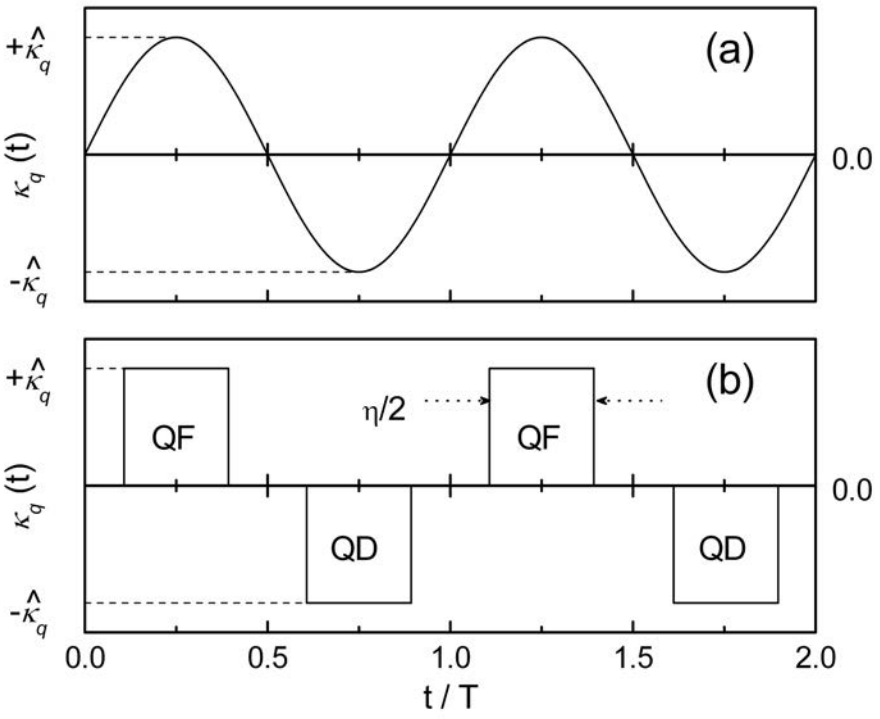

Figure 2.2: Illustrative oscillatory waveforms for the quadrupole focusing coefficient $\kappa_q(t)$ corresponding to (a) the sinusoidal waveform $\kappa_q(t) = \hat{\kappa}_q \sin(2\pi t/T)$, and (b) a periodic step-function waveform with maximum amplitude $\hat{\kappa}_q$ and filling factor η [1].

mately by

$$\omega_q = \frac{8q}{m\pi r_w^2}\left(\frac{\hat{V}_0}{f_0}\right)\frac{\eta}{4}\sqrt{\left(1-\frac{2}{3}\eta\right)}. \tag{2.34}$$

It is interesting to note that when $\eta = 0.572$, both the sinusoidal waveform and the periodic step-function lattice give the same value of the smooth-focusing frequency. Experiments performed to date using PTSX have employed a sinusoidal waveform [14].

The actual slow transverse oscillation frequency (depressed betatron frequency) is determined by including the net radial force. The self-electric field of the nonneutral plasma is repulsive and serves to depress the transverse oscillation frequency. For uniform density plasma, the depressed betatron frequency ν_b for slow transverse particle oscillations is approximately given by

$$\nu_b^2 = \omega_q^2 - \frac{\hat{\omega}_p^2}{2}. \tag{2.35}$$

Here, we denote the uniform plasma density by $\hat{n}$ and the corresponding plasma frequency by $\hat{\omega}_p = (\hat{n}q^2/\epsilon_0 m)^{1/2}$. An important dimensionless parameter $\hat{s}$ that measures the normalized beam intensity and self-field force on a particle is defined by

$$\hat{s} \equiv \frac{\hat{\omega}_p^2/2}{\omega_q^2}. \tag{2.36}$$

The factor $1/2$ associated with $\hat{\omega}_p^2$ in Eqs. (2.35) and (2.36) is a geometric factor which results when a rigorous calculation of the collective oscillation frequency is carried out [1]. For the transverse confinement of a beam particle by applied focusing field, we require that $\hat{s} < 1$, or equivalently $\nu_b^2 > 0$.

Particles in general travel for several oscillation periods of $V_0(t)$ before completing one slow transverse oscillation, and the advance in phase of the slow transverse oscillation that the particle undergoes per oscillation period T is called the *phase advance* σ. Due to the self-electric field, the phase advance σ is smaller than the *vacuum phase advance* σ_v that is computed in the absence of space-charge effects. The quantity σ/σ_v is a measure of the relative strength of space-charge effects as compared to the strength of the applied focusing field. In the smooth-focusing approximation which is valid for vacuum phase advance $\sigma_v \leq 2\pi/5 = 72^\circ$, The exact vacuum phase advance σ_v is approximately equal to σ_v^{sf}, which is defined as:

$$\sigma_v \sim \sigma_v^{sf} = \frac{\omega_q}{f_0}. \tag{2.37}$$

Further, for a uniform density profile, the depressed vacuum phase advance is related to $\hat{s}$ by the relation $\sigma^{sf} = \sigma_v^{sf}(1-\hat{s})^{1/2}$ in the smooth-focusing approximation.

In storage rings and circular accelerators, it is customary to introduce the tune ν (often, especially in the European literature, it is denoted by Q), which is defined as the number of slow transverse oscillations that a particle makes as it circulates once around the ring with circumference C. In the absence of the beam, the *undepressed tune* is approximately $\nu_0 = C\omega_q/2\pi V_b$, where V_b is the axial beam velocity. In the presence of the unform density

beam, however, the *depressed tune* ν is given by $\nu = \nu_0(1-\hat{s})^{1/2}$. The corresponding *tune shift* that results from the beam space charge is given by $\Delta\nu = \nu - \nu_0 = \nu_0\left[(1-\hat{s})^{1/2} - 1\right]$, and *tune depression* is given by

$$\frac{\nu}{\nu_0} = (1-\hat{s})^{1/2}. \tag{2.38}$$

The dimensionless parameter ν/ν_0 is complementary to the normalized intensity parameter $\hat{s}$ in the way in which it characterizes the relative strength of the space-charge effects. We also note that $\nu/\nu_0 = \sigma^{sf}/\sigma_v^{sf}$.

As mentioned earlier, transverse confinement of the nonneutral plasma column by the focusing field requires $\hat{s} < 1$ or $\hat{\omega}_p/\sqrt{2} < \omega_q$. On the other hand, to avoid so-called the single-particle orbit instability associated with an overly strong focusing field, the vacuum phase advance σ_v should be less than 180°. In the smooth-focusing approximation for a sinusoidal waveform of $V_0(t)$, this condition can be expressed as $\sigma_v^{sf} = \omega_q/f_0 < 0.9080\pi/\sqrt{2}$ (= 115.6°). Combining these inequalities gives

$$\frac{1}{\sqrt{2}}\left(\frac{\hat{n}q^2}{\epsilon_0 m}\right)^{1/2} < \frac{8q\hat{V}_0}{m\pi r_w^2 f_0}\frac{1}{2\sqrt{2}\pi} < 0.9080\frac{\pi}{\sqrt{2}} \times f_0. \tag{2.39}$$

The inequalities in Eq. (2.39) are expected to assure robust transverse confinement of the plasma particles in the PTSX. The PTSX device is capable of reaching and exceeding the right-most inequality in Eq. (2.39). Note that this limit can be expressed as a quadratic relationship between $\hat{V}_0$ and f_0 which are the parameters directly controlled in the laboratory. Due to electronics limitations, we normally operate the system in the parameter space ($f_0 <$ 100 kHz, $\hat{\mathrm{V}}_0 <$ 400 Volts). Combining these conditions and Eq. (2.39) for a singly ionized cesium ion yields $\omega_q \leq 100 \times 10^3$ s^{-1}, and $\hat{n} \leq 1.5 \times 10^6$ cm^{-3}. The density limit is consistent with the collisionless plasma condition discussed in Sec. 2.2.3.

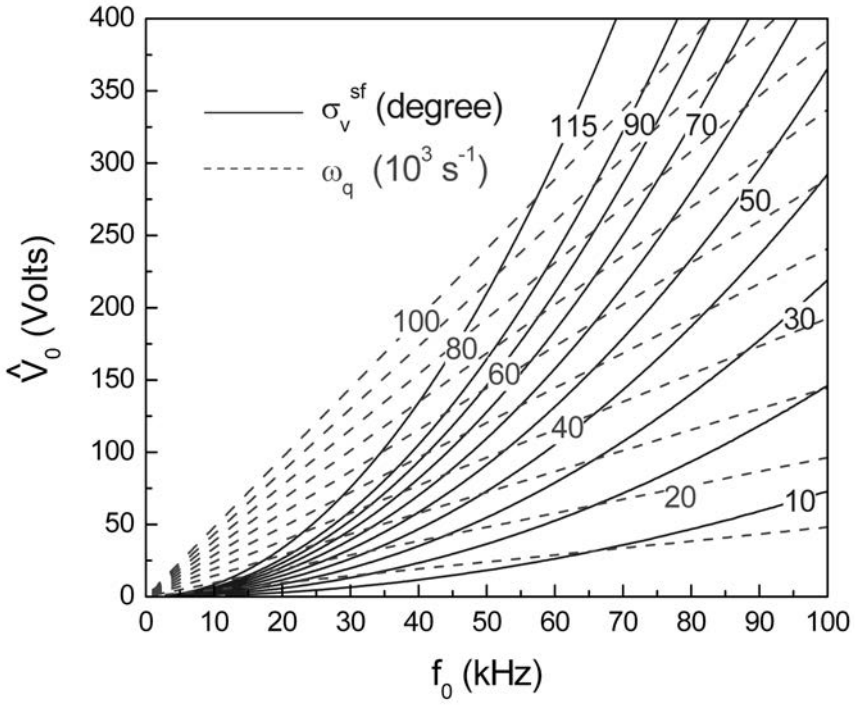

Figure 2.3: In the $(f_0, \hat{V}_0)$ parameter space, curves of constant vacuum phase advance σ_v^{sf} are parabolae, while the curves of constant average focusing frequency ω_q are straight lines [90].

2.3 Beam Dynamics in the Paul Trap Simulator Experiment (PTSX)

In this section, we present several beam dynamics models that are relevant to the analysis of the experimental results of the PTSX in the subsequent chapters. For the quadruple focusing field, a sinusoidal waveform

$$\kappa_q(t) = \hat{\kappa}_q \sin(2\pi f_0 t + \Phi) \tag{2.40}$$

is adopted. Here, an arbitrary constant phase Φ has been introduced in Eq. (2.40). When the initial beam is in the focusing (F) and defocusing (D) phases, then $2\pi f_0 t + \Phi = \pm\pi/2$, and when in the drift (O) phase, then $2\pi f_0 t + \Phi = 0$.

2.3.1 Single-Particle Orbits

For the quadrupole focusing field given in Eq. (2.40), the single-particle motion in the absence of space-charge effects and end effects is governed by a pair of uncoupled Mathieu equations,

$$\begin{aligned} \frac{d^2}{dt^2}x(t) + \hat{\kappa}_q \sin(2\pi f_0 t + \Phi)x(t) &= 0 \\ \frac{d^2}{dt^2}y(t) - \hat{\kappa}_q \sin(2\pi f_0 t + \Phi)y(t) &= 0 \end{aligned} \tag{2.41}$$

Detailed properties of the solutions for $x(t)$ to Mathieu's equation (2.41) have been extensively tabulated by Abramowitz and Stegun [91]. The first-order solution $\tilde{x}(t)$ can be approximated as follows:

$$\tilde{x}(t) = x_{sf}(t)\left[1 + \frac{\sigma_v^{sf}}{\pi\sqrt{2}}\sin(2\pi f_0 t + \Phi)\right], \tag{2.42}$$

with the smooth-focusing motion term $x_{sf}(t)$ given by (for $\cos\phi_0 \neq 0$)

$$x_{sf}(t) = \frac{x_0}{\cos\phi_0\left[1 + (\sigma_v^{sf}/\pi\sqrt{2})\sin\Phi\right]}\cos(\omega_q t + \phi_0). \tag{2.43}$$

Here, ω_q is the smooth-focusing frequency in Eq. (2.33), $\sigma_v^{sf} = \omega_q/f_0$ is the smooth-focusing vacuum phase advance, and x_0 and ϕ_0 are constants determined from the initial conditions $x(t=0) = \tilde{x}(t=0) = x_0$ and $\dot{x}(t=0) = \dot{\tilde{x}}(t=0)$. The smooth-focusing term represents a simple harmonic oscillation with spring constant $m\omega_q^2$, where the restoring force is the ponderomotive force associated with rapidly oscillating inhomogeneous electric fields [18]. The approximate solution Eq. (2.42) is valid only for sufficiently small σ_v^{sf}, and when $\sigma_v^{sf} > 115.6^\circ$ [90], the solutions for $x(t)$ to Eq. (2.41) are unstable (i.e., grow without bound). If one is near the stability limit, then the actual value of vacuum phase advance σ_v has to be obtained by integrating Eq. (2.41) numerically over several focusing periods.

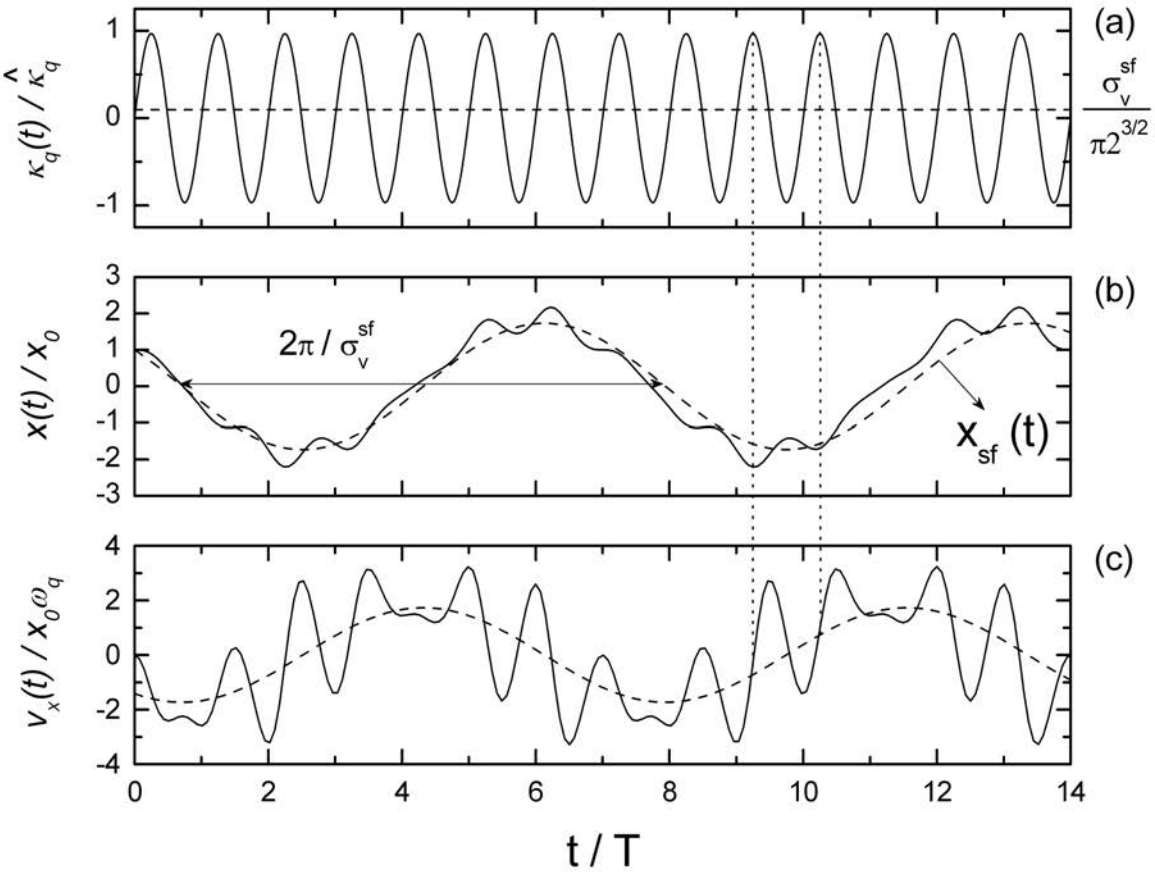

Figure 2.4: Illustrative examples of (a) focusing coefficient $\kappa_q(t)$, and time history of (b) position and (c) velocity of single-particle motion in the PTSX. Here, $\sigma_v^{sf} = 49.8°$, $\Phi = 0$, $x(t = 0) = x_0$, and $\dot{x}(t = 0) = 0$. The dashed lines correspond to the contributions from the smooth-focusing motion term in Eq. (2.42) with $\phi_0 = \tan^{-1}\sqrt{2}$. When σ_v^{sf} is too high, the single-particle motion is overfocused and becomes unstable (i.e., $\sigma_v^{sf} \to 115.6°$). When σ_v^{sf} is too low, the transverse focusing is too weak and single-particle motion becomes vulnerable to the defocusing space-charge force (i.e., $\hat{s} \to 1$) [88].

Making use of Floquet's theorem [40] allows us to determine the exact phase advance through the relation

$$\sigma_v = \cos^{-1}\left\{\frac{x(t)+x(t+2T)}{2x(t+T)}\right\}, \tag{2.44}$$

which is indeed independent of t, and the single-particle orbit remains stable for $\sigma_v < 180^\circ$. As shown in Fig. 2.5, the smooth-focusing vacuum phase advance σ_v^{sf} is in good agreement with the exact (numerically-calculated) vacuum phase advance σ_v for $\sigma_v \leq 2\pi/5 = 72^\circ$, suggesting that the smooth-focusing approximation is valid provided σ_v is sufficiently small. Possible effects on the single-particle orbits due to axial bouncing motions in the PTSX are discussed in **Appendix A** of [88].

The above discussions assume the absence of space-charge effects. But, for the next generation of high intensity accelerators, space charge effects are not negligible. When the self-field electrostatic potential $\phi^s(x,y,t)$ is considered, Eq.(2.41) becomes

$$\begin{aligned}
\frac{d^2}{dt^2}x(t) + \hat{\kappa}_q \sin(2\pi f_0 t + \Phi)x(t) &= -\frac{\partial\phi^s(x,y,t)}{\partial x} \\
\frac{d^2}{dt^2}y(t) - \hat{\kappa}_q \sin(2\pi f_0 t + \Phi)y(t) &= -\frac{\partial\phi^s(x,y,t)}{\partial y}
\end{aligned} \tag{2.45}$$

The solutions to Eq.(2.45) for the transverse orbits $x(t)$ and $y(t)$, also depend on the self-field electrostatic potential $\phi^s(x,y,t)$, which is determined self-consistently in terms of the beam number density $n(x,y,t)$ from Poission's equation. Generally, the force terms proportional to -$\partial\phi^s/\partial x$ and -$\partial\phi^s/\partial y$ couple the $x-$ and $y-$ motions, making a detailed analysis of the orbit equations for $x(t)$ and $y(t)$ difficult except in the case of a uniform focusing field with $\kappa_q(t) = const.$ However, for the special case of a uniform density beam, we will find (Sec. 2.3.2) that $\partial\phi^s/\partial x$ ($\partial\phi^s/\partial y$) is linearly proportional to x (y), in which case an analysis of the transverse orbit equations is relatively straighforward, even for the case of intense self-fields.

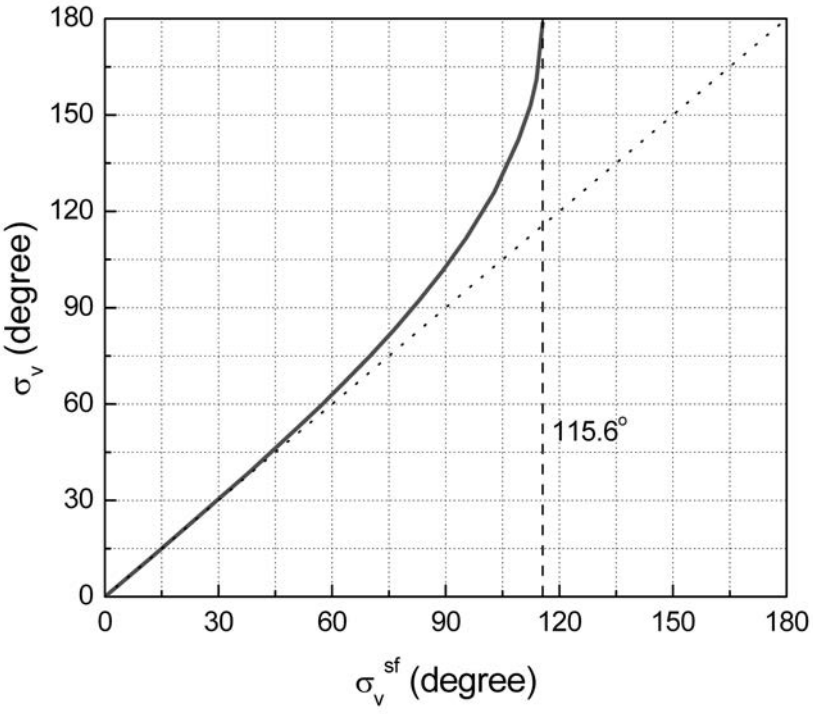

Figure 2.5: Plot of the (exact) vacuum phase advance σ_v calculated numerically from Eq. (2.44) versus the vacuum phase advance σ_v^{sf} determined using ω_q as calculated in the smooth-focusing approximation for the sinusoidal lattice function. The agreement is very good for $\sigma_v \leq 2\pi/5 = 72°$.

2.3.2 Envelope Equations

To describe an ensemble of particles in a periodic focusing quadrupole field with self-field force, we consider an axially-uniform long charge bunch with uniform number density $n(x, y, t) = \hat{n}(t)$ within the elliptical cross-section $0 \leq x^2/a^2(t) + y^2/b^2(t) \leq 1$, and zero density outside. Here, $a(t)$ and $b(t)$ are the x- and y-direction envelopes (or half-widths) of the beam. Such a periodically-focused uniform-density beam is obtained self-consistently for the choice of the Kapchinskij-Vladimirskij (KV) distribution function [1, 48], which is the only known exact, periodically-focused equilibrium solution to the nonlinear Vlasov-Poisson equations, including intense self-field effects. In this KV beam, the line density

$N = \int dx\ dy\ n(x,y,t) = \hat{n}\pi ab = const.$, and the self-field potential is given by [1,16]

$$\frac{q}{m}\phi^s(x,y,t) = -\frac{2K}{a+b}\left[\frac{1}{a}x^2 + \frac{1}{b}y^2\right], \tag{2.46}$$

in the beam interior. where K is the dimensional self-field perveance indicating the relative strength of the space-charge effects and is defined by $K = \frac{1}{4\pi\epsilon_0}\frac{2Nq^2}{m}$. Here, we have taken $\phi^s = 0$ at $(x,y) = (0,0)$ without loss of generality, and assumed $a, b \ll r_w$, which means that image-charge effects [92,93] from the conducting wall at radius r_w are neglected.

Even though the KV beam is singular and unphysical because it has a highly-inverted distribution in phase space, it can describe the root-mean-squared (rms) behavior of a beam with a more realistic transverse phase-space distribution, when the two beams have the same line density and rms beam qualities (such as rms emittance defined later). This concept of *equivalent beams* was first introduced by Lapostolle [94] and Sacherer [95] in 1971 and has been a useful approximation for beam dynamics analysis. Important parameters in the concept of equivalent beams include the rms x and y dimensions of the beam, $\langle x^2\rangle^{1/2}$ and $\langle y^2\rangle^{1/2}$, and the x and y rms beam velocities, $\langle \dot{x}^2\rangle^{1/2}$ and $\langle \dot{y}^2\rangle^{1/2}$. Here, the statistical average of a phase function $\xi(x,y,\dot{x},\dot{y},t)$ over the four-dimensional phase space is denoted by $\langle\xi\rangle(t)$ and is defined by

$$\langle\xi\rangle = \frac{\int dx\ dy\ d\dot{x}\ d\dot{y}\ \xi\ f}{\int dx\ dy\ d\dot{x}\ d\dot{y}\ f}, \tag{2.47}$$

where $f(x,y,\dot{x},\dot{y},t)$ is the distribution function. Note that for a KV beam, $\langle x^2\rangle^{1/2} = a(t)/2$ and $\langle y^2\rangle^{1/2} = b(t)/2$.

To quantitatively describe the beam quality, the concept of rms emittance [94, 95] is introduced. The rms emittance is not only related to the phase-space volume occupied by the beam particles (which should be conserved by Liouville's theorem), but also dependent on the distortion (filamentation) produced by nonlinear forces [38,39]. If the motions in the x and y directions are decoupled, as often happens in beam transport systems [71], we can define two transverse phase planes $(x,\dot{x})$ and $(y,\dot{y})$, and corresponding x- and y-transverse

emittances, $\epsilon_x(t)$ and $\epsilon_y(t)$, which are given by [38, 96]

$$\epsilon_x(t) = 4\left[\left\langle x^2\right\rangle\left\langle \dot{x}^2\right\rangle - \left(\frac{1}{2}\frac{d}{dt}\left\langle x^2\right\rangle\right)^2\right]^{1/2}, \tag{2.48}$$

$$\epsilon_y(t) = 4\left[\left\langle y^2\right\rangle\left\langle \dot{y}^2\right\rangle - \left(\frac{1}{2}\frac{d}{dt}\left\langle y^2\right\rangle\right)^2\right]^{1/2} \tag{2.49}$$

Because these emittances are defined in the beam frame (i.e., laboratory frame of the PTSX), and are not affected by the axial motion, they are said to be *normalized*. If both transverse focusing and space-charge forces are linearly proportional to transverse displacement (such as for the KV beam), the emittances defined by Eqs. (2.48) and (2.49) can be shown to be conserved by Liouville's theorem [1]. For the KV beam, the transverse rms emittance is directly proportional to the phase-space area *uniformly* occupied by the beam particles by factor $1/\pi$, and its value is invariant in the smooth-focusing approximation [1].

Making use of Eq. (2.46) to express self-field forces and following the procedures in Davidson and Qin [1, 97] readily gives

$$\frac{d^2}{dt^2}a(t) + \kappa_q(t)a(t) - \frac{2K}{a(t)+b(t)} = \frac{\epsilon_x^2}{a^3(t)}, \tag{2.50}$$

$$\frac{d^2}{dt^2}b(t) - \kappa_q(t)b(t) - \frac{2K}{a(t)+b(t)} = \frac{\epsilon_y^2}{b^3(t)}, \tag{2.51}$$

which describe the evolutions of x- and y-direction envelopes of the KV beam, $a(t)$ and $b(t)$, in periodic focusing quadruple field $\kappa_q(t)$. The envelope equations (2.50) and (2.51) represent a system of two nonlinear, second-order coupled differential equations which, in general, must be solved numerically for given initial conditions $\Big(a(0), \dot{a}(0), b(0), \dot{b}(0)\Big)$. If two beams have the same perveance (or equivalently, line density or current), rms emittances, and initial conditions as the equivalent KV beam, then the transverse rms dimensions of the two beams evolve identically according to Eqs. (2.50) and (2.51). However, there is an implicit assumption in this model that the rms emittance of the two beams being compared remains

the same or that the emittance change in time is known a priori [38]. This assumption is in general not correct, especially when there is a free energy source for emittance growth such as charge nonuniformity [96] and rms mismatch [98].

When the rms dimensions of a beam have the same oscillation frequency as the focusing field, the beam is said to be *rms-matched* and emittance growth is minimized [38]. For a KV beam, the rms matching condition can be expressed as $a(t+T) = a(t)$ and $b(t+T) = b(t)$, resulting in $f(x, y, \dot{x}, \dot{y}, t+T) = f(x, y, \dot{x}, \dot{y}, t)$ and $\langle a(t)b(t)\rangle_T = \bar{r}_b^2 = const.$ On the other hand, if the beam is rms-mismatched, nonlinear forces can give rise to a filamentation in phase space causing the rms emittance to increase [39, 94]. This process cannot be described solely by the envelope equations for the equivalent KV beam. When the beam is mismatched in a quadrupole focusing channel, the two transverse degrees of freedom in Eqs. (2.50) and (2.51) yield two fundamental oscillation modes, which are the breathing mode and the quadrupole mode. For the breathing mode, the evolution of $\langle a(t)\rangle_T$ and $\langle b(t)\rangle_T$ are in-phase body-wave perturbations, and the frequency is approximately given by [1, 38]

$$\omega_B \approx 2\omega_q \left[1 - \frac{1}{2}\left(\frac{K}{\bar{r}_b^2 \omega_q^2}\right)\right]^{1/2}. \tag{2.52}$$

On the other hand, for the evolution of $\langle a(t)\rangle_T$ and $\langle b(t)\rangle_T$ for the out-of-phase surface-wave perturbations of the quadrupole mode, the frequency is approximately given by [1, 38]

$$\omega_Q \approx 2\omega_q \left[1 - \frac{3}{4}\left(\frac{K}{\bar{r}_b^2 \omega_q^2}\right)\right]^{1/2}. \tag{2.53}$$

Note that $\omega_q \leq \omega_Q \leq \omega_B \leq 2\omega_q$ and $\omega_Q = \omega_B = 2\omega_q$ for $K \to 0$. Generally, beam mismatch produces a mixed mode composed of both breathing and quadrupole modes. In the mixed mode, there often appears a slow amplitude modulation in the oscillations of the mean radius $\sqrt{a(t)b(t)}$ [see Fig. 2.6(b)].

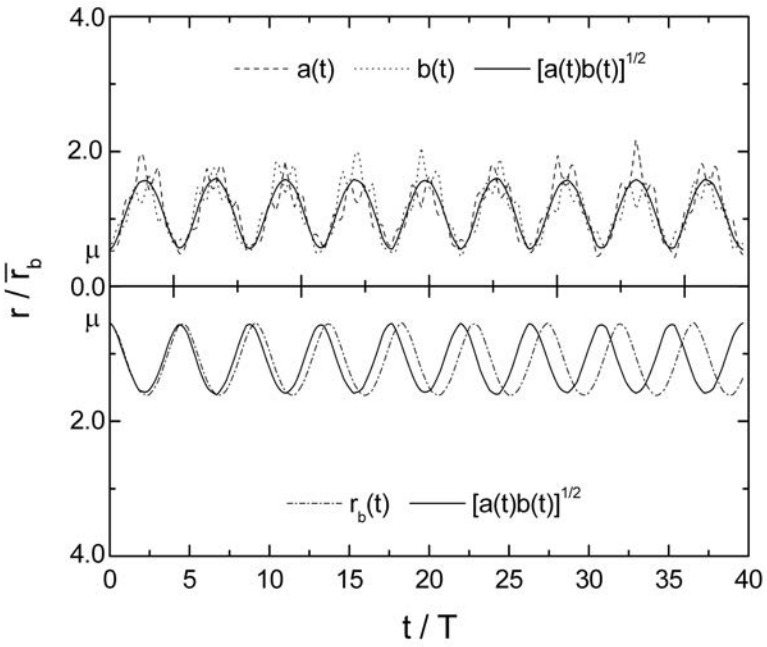

(a) $\Phi = \pi/2$. A pure breathing mode is excited.

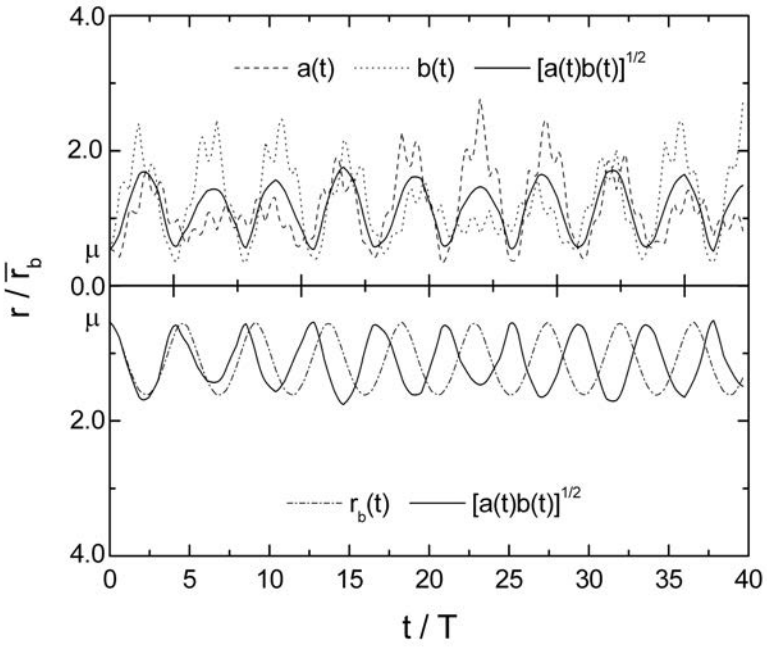

(b) $\Phi = 0$. A mixed mode is excited.

Figure 2.6: Time evolutions of the x- and y-beam envelopes, $a(t)$ and $b(t)$, mean radius $[a(t)b(t)]^{1/2}$, and beam radius $r_b(t)$ in the smooth-focusing approximation. Here, we consider a KV beam with strong injection mismatch for $\mu = 0.54$, $\bar{s} = 0.85$, $\sigma^{sf} \approx 49.8^\circ(1-\bar{s})^{1/2}$, and $\sigma \approx 51.4^\circ(1-\bar{s})^{1/2}$. Initially, $\Big(a(0), \dot{a}(0), b(0), \dot{b}(0)\Big) = (\mu\bar{r}_b, 0, \mu\bar{r}_b, 0)$ and $\epsilon_x = \epsilon_y = \epsilon = \bar{r}_b^2\omega_q(1-\bar{s})^{1/2}$ [88].

2.3.3 Beam Equilibrium

A nonneutral collection of ions confined by an external periodic focusing potential will relax to a quasi-equilibrium state. In this section, we follow the derivations in Sec. 7.3 of [1]. In equilibrium, local radial force balance on a fluid element of ions with charge q and mass m in the smooth-focusing approximation is given by [1]

$$\frac{\partial}{\partial r}P_\perp(r) = -qn(r)\frac{\partial}{\partial r}\phi^s(r) - m\omega_q^2 n(r)r, \tag{2.54}$$

where $n(r)$ is the equilibrium radial density profile, ω_q is the applied smooth-focusing frequency, and r is the radial distance from the beam axis. Here, the space-charge potential $\phi^s(r)$ is determined self-consistently from Poisson's equation $r^{-1}\partial_r\left(r\partial_r\phi^s\right) = -qn(r)/\epsilon_0$, and $P_\perp(r) = n(r)T_\perp(r)$ is the perpendicular pressure profile which is proportional to transverse temperature profile $T_\perp(r)$. A necessary condition for transverse confinement of the ions is that the applied focusing force in Eq. (2.54) should be sufficiently strong to exceed the defocusing self-field force, i.e., $m\omega_q^2 n(r)r > qn(r)E_r^s$, where $E_r^s = -\partial\phi^s/\partial r = (q/\epsilon_0 r)\int_0^r dr\; r\; n(r)$ is the radial space-charge field. For present purposes, we assume that $n(r)$ is a monotonically decreasing function of r from the on-axis value $n(r=0) = \hat{n}$. Then, for small r, we obtain $E_r^s = (q/2\epsilon_0)\hat{n}r$, and have the requirement

$$\hat{s} \equiv \frac{\hat{\omega}_p^2/2}{\omega_q^2} < 1. \tag{2.55}$$

Here, $\hat{\omega}_p^2 = \hat{n}q^2/\epsilon_0 m$ is the on-axis ($r=0$) plasma frequency-squared.

We now consider an anisotropic equilibrium distribution function f^0 in the smooth-focusing approximation of the form

$$f^0 = F(H_\perp)G(p_z), \tag{2.56}$$

where the perpendicular Hamiltonian $H_\perp$ can be expressed as

$$H_\perp = \frac{p_x^2 + p_y^2}{2m} + V(r), \tag{2.57}$$

with effective potential for the transverse particle motion $V(r)$ being defined by

$$V(r) = \frac{1}{2} m\omega_q^2 r^2 + q\phi^s(r). \tag{2.58}$$

Here, equilibrium properties ($\partial/\partial t = 0$) are assumed to be azimuthally symmetric ($\partial/\partial\theta = 0$) and independent of axial coordinate ($\partial/\partial z = 0$). Assuming the axial momentum distribution $G(p_z)$ to be normalized according to $\int_{-\infty}^{\infty} dp_z G(p_z) = 1$, it follows that

$$n(r) = \int dp_x dp_y dp_z f^0 = \int_0^\infty \pi dp_\perp^2 F\left(\frac{p_\perp^2}{2m} + V(r)\right), \tag{2.59}$$

and

$$\begin{aligned} P_\perp(r) &= n(r) T_\perp(r) \\ &= \frac{1}{2}\int dp_x dp_y dp_z (p_x \dot{x}_{sf} + p_y \dot{y}_{sf}) f^0 \\ &= \int_0^\infty \pi dp_\perp^2 \left(\frac{p_\perp^2}{2m}\right) F\left(\frac{p_\perp^2}{2m} + V(r)\right). \end{aligned} \tag{2.60}$$

Here, $(p_x, p_y) = m(\dot{x}_{sf}, \dot{y}_{sf})$, $p_\perp^2 = p_x^2 + p_y^2$, and use has been made of $\int_{-\infty}^{\infty} dp_x \int_{-\infty}^{\infty} dp_y \cdots = \int_0^\infty \pi dp_\perp^2 \cdots$. We now operate on Eq. (2.54) with $2\pi \int_0^{r_w} dr r^2 \cdots$, and carry out an integration by parts assuming $P_\perp(r = r_w) = 0$. This gives the exact global force balance equation [1]

$$m\omega_q^2 R_b^2 = 2\bar{T}_\perp + \frac{Nq^2}{4\pi\epsilon_0}, \tag{2.61}$$

which is valid for the entire class of anisotropic equilibrium functions $f^0 = F(H_\perp)G(p_z)$ expressed in Eq. (2.56). Here, $N = 2\pi \int_0^{r_w} dr r n(r)$ is the line density, $R_b^2 = (2\pi/N)\int_0^{r_w} dr\, r\, r^2\, n(r)$ is the mean-square radius of the beam, and $\bar{T}_\perp$ is the effective transverse temperature defined

by

$$\bar{T}_\perp = \frac{2\pi}{N}\int_0^{r_w} drr \left\langle \frac{p_\perp^2}{2m} \right\rangle_{p_x,p_y} n(r). \tag{2.62}$$

The notation $\langle \cdots \rangle_{p_x,p_y}$ denotes the statistical average over the equilibrium distribution function in the transverse momentum subspace. Note that the effective transverse temperature $\bar{T}_\perp$ measures the kinetic energy per particle averaged over the transverse phase space (i.e., $\bar{T}_\perp = m\left\langle \dot{x}_{sf}^2 + \dot{y}_{sf}^2 \right\rangle_0 /2$) in the smooth-focusing equilibrium, where fast micromotion associated with quadrupole focusing frequency f_0 has been averaged out, and there is no drift motion of the fluid element ($dR_b/dt = 0$). In the Paul Trap Simulator Exepriment, the smooth-focusing frequency ω_q can be calculated using the amplitude and the frequency of the oscillating voltage waveforms. The rms radius R_b and line charge density N can be calculated from the radial density profiles of the charge bunch. Then we can use the global force equation Eq. 4.7 to compute the effective transverse temperature $\bar{T}_\perp$.

2.4 Summary and Discussion

In this chapter, the analogy between the transverse dynamics of intense charged particle beams propagating through a magnetic alternating-gradient focusing system and that of a charge bunch in a Paul Trap configuration were investigated using the Lorentz transformation. In Sec. 2.2, it is shown that when the laboratory reference frame is transferred to the beam reference frame which moving together with the beam, the forms of electromagnetic forces on the charged particles in the periodic transport system are equivalent to those on the charge bunch in the PTSX. Therefore, the PTSX provides a convenient and cost-effective way to study the transverse dynamics of the intense charged particle beams. For the transverse confinement of a charged particle, we required that the normalized beam intensity $\hat{s} < 1$. Typically, we choose $\hat{s} \sim 0.2$. To avoid the so-called single-particle orbit instability associated with overly strong focusing field, we require $\sigma_v^{sf} < 115.6°$. In Sec. 2.3, we discussed several simplified beam dynamics models including single particle orbit model(Sec. 2.3.1),

envelop equation model based on a KV beam (Sec. 2.3.2) and thermal equilibrium model (Sec. 2.3.3) to gain some insights on the characteristics of the intense charge particle beams. To describe the evolution of the intense charge particle beams self-consistently, one needs to solve the nonlinear Vlasov-Maxwell equations numerically employing particle-in-cell (PIC) models and nonlinear perturbative simulation techniques [59, 60, 99].

Chapter 3

Experimental Setup

3.1 Introduction

Paul Trap Simulator Experiment (PTSX) is a compact Paul Trap simulating the propagation of intense charged particle beams in the periodic magnetic alternating-gradient transport systems. In this chapter, we briefly describe the working principles of the Paul Trap Simulator Experiment (PTSX) apparatus. Sec. 3.2 gives a general overview of the basic equipment and operation of the PTSX device, Sec. 3.3 describes the cesium ion source which has been used for the initial phase of PTSX experiments, Sec. 3.4 describes the charge collector diagnostic for measuring the radial ion density profile.

3.2 The Paul Trap Simulator Experiment Device

The Paul Trap Simulator Experiment (PTSX) device is a linear Paul Trap [13] constructed from a 2.8 m-long, $r_w = 10$ cm-radius, gold-plated stainless steel cylinder as shown in Figs. 3.1 and 3.2. The cylinder is divided into two 40 cm-long end cylinders and a $2L = 2$ m-long central cylinder. All cylinders are azimuthally divided into four 90° sectors so that when an oscillating voltage $V_0(t)$ is applied with alternating polarity on adjacent segments, the resulting electric field becomes an oscillating quadruple field near the trap axis. This

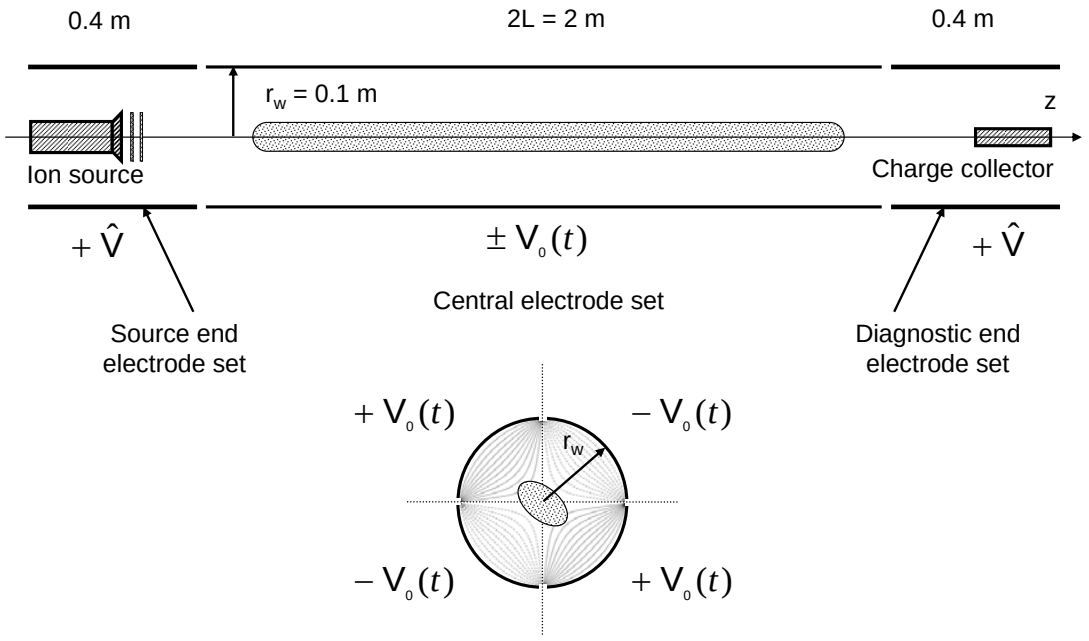

Figure 3.1: Schematic design of the PTSX device showing the electrodes, the charge collector and the cesium ion source [88].

quadrupole electric field exerts a ponderomotive force that confines the pure ion plasma radially. To trap the plasma axially, the two end electrodes are biased to a constant positive voltage $+\hat{V}$. The gold plating of the electrodes increases the surface conductivity so that small patches of charge do not build up on the surface and influence the behavior of the trapped plasma. Note that, to place the charge collector along the null of the quadrupole potential and to facilitate the laser-induced fluorescence (LIF) diagnostic set up (Sec. 5.3), the electrodes are installed after rotating 45° azimuthally from the configuration used in the theoretical analysis (compare Figs. 2.1 and 3.1). The aluminum rings and insulating spacers support the electrodes, and in-vacuum insulated wires are attached to each electrode surface using lead-free silver solder [Fig. 3.2(b)]. Adjustments of the set screws that move the ball-bearings on the aluminum rings together with the use of a theodolite, allow alignment of the center of the electrodes to within 1 mm.

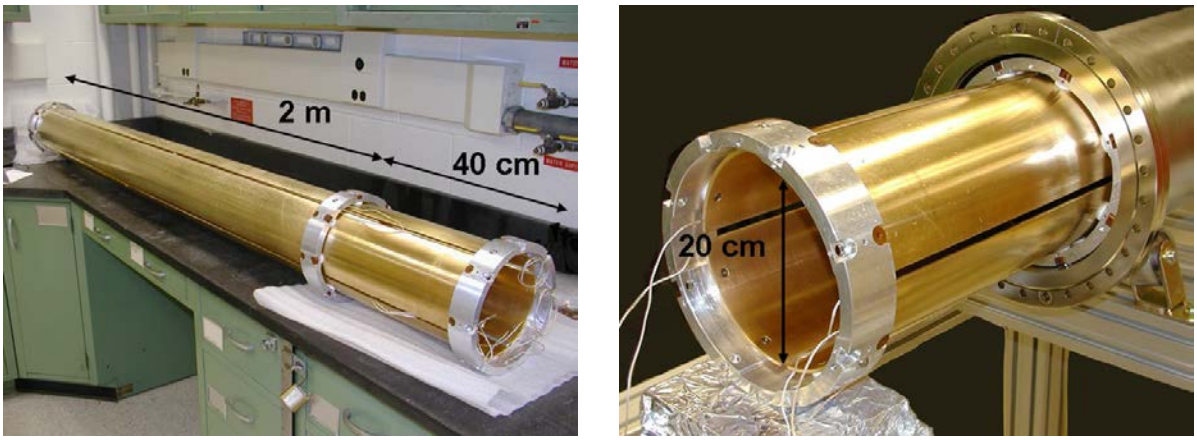

(a) Central and source end electrodes.

(b) Diagnostic end electrodes.

Figure 3.2: The gold-plated stainless-steel electrodes confine the cesium ions within the central electrode.

The cesium ion source is located on the trap axis near the center of one of the short electrode sets so that ion injection is not affected by the fringe fields (Sec. 3.3). The charge collector is mounted on a linear motion feedthrough at the other set of short electrodes, and moves in the transverse direction along a null of the applied potential in order to minimize the perturbation on the quadrupole potential configuration (Sec. 3.4). The construction of the PTSX device was completed in 2003 after a two-year construction period [7, 90], and initial experiments successfully demonstrated quiescent beam propagation over equivalent distances of tens of kilometers over a wide operating range [14].

3.2.1 Operation Principle

The PTSX device manipulates the plasma using an inject-trap-dump-rest cycle, and the one-component plasmas created in the trap are highly reproducible. The time duration of the injecting (t_i), trapping (t_t), dumping (t_d), and resting (t_r) phases can be varied independently, and the total cycle time is $t_{\text{cycle}} = t_i + t_t + t_d + t_r$. For the applied voltage waveform, a sinusoidal waveform $V_0(t) = \hat{V}_0 \sin(2\pi f_0 t)$ is used.

Figure. 3.3 represents a complete trapping cycle. Each stage is discussed in details as follows:

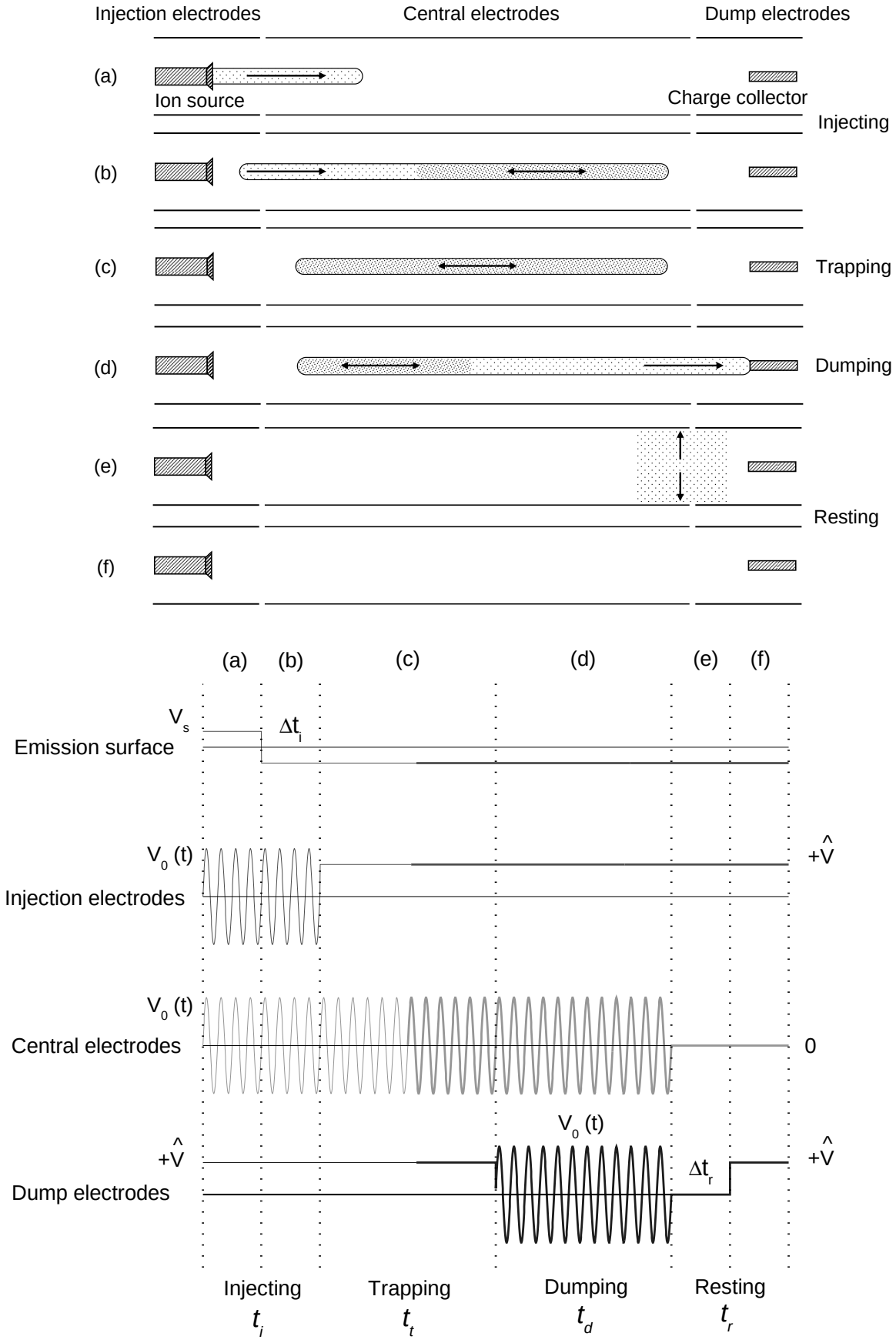

Figure 3.3: Operation sequence of the PTSX. The shaded regions in the plasma columns indicate the overlapping of two counter-streaming beams. [88]

Figure. 3.3 (a) shows that during injection, the short electrodes on the source end (injection electrodes) are made to oscillate with the same voltage waveform, $\pm V_0(t)$, as the central electrodes, which allows the ions to stream into the trap. Because ions are injected from the ion source with a circular, stationary cross section into a transverse focusing system in which the matched state has a pulsating elliptical beam envelope, the injected plasma column is always somewhat mismatched to the alternating-gradient (AG) focusing lattice (see Figs. 1.1 and 2.2). This type of mismatch is inherent and unavoidable with the ion source as presently configured. We can minimize this injection mismatch by setting $r_s \sim \sqrt{2}R_b$, where r_s is the radius of the emission surface and R_b is the rms radius of the matched beam.

Figure 3.3 (b) show that, during injection, the short electrodes on the diagnostic end (dump electrodes) are biased to a DC voltage $+\hat{V}$ so that the ions bounce off the potential barrier. In order to minimize the number of ions present in the vicinity of the injection electrodes when the injection electrodes are switched to their static trapping voltage $+\hat{V}$, the time duration of injecting (t_i) is kept less than the axial bounce time (τ_b) and ion injection is stopped a short time Δt_i before the end of the injecting stage. Although, the ion source is operated in a steady-state manner, ion injection can be controlled by adjusting the bias voltage on the emission surface (V_s). Hence, to stop the ion emission, V_s is switched to a negative bias voltage.

In Figure 3.3 (c), after injection is finished, the plasma is allowed to relax for several bounce periods so that the residual mismatch oscillation is damped away. The time duration of trapping (t_t) is $t_t \lesssim 300$ ms to prevent collisional effects from playing a significant role. Due to axial potential leak from the end electrodes into the central electrodes, the plasma length L_p is less than the trap length $2L$. The characteristic parameters of the typical trapped plasma in PTSX are summarized in Table 3.1.

The charge collector is a destructive diagnostic that requires dumping the plasma out of the trap each cycle. During dumping, the dump electrodes are made to oscillate with the same voltage waveform as the central electrodes, which allows the ions to stream out of the

Quantity	Symbol	Characteristic value
Background gas pressure	P	5×10^{-9} Torr
Applied AC focusing voltage	$\hat{V}_0$	150.4 V
Applied DC bias voltage	$\hat{V}$	36 V
Applied magnetic field	B_0	0 G
Plasma length	L_p	170 cm
Plasma rms radius	R_b	0.85 cm
Debye length (on-axis)	λ_D	0.88 cm
Plasma density (on-axis)	$\hat{n}$	0.89×10^5 ions/cm^3
Plasma line density	N	1.6×10^5 ions/cm
Plasma parameter	N_D	2.6×10^5 ions
Applied AC focusing frequency	f_0	60 kHz
Smooth-focusing frequency	$\omega_q/2\pi$	8.4 kHz
Plasma frequency (on-axis)	$\hat{\omega}_p/2\pi$	5.4 kHz
Breathing mode frequency	$\omega_B/2\pi$	15.8 kHz
Quadrupole mode frequency	$\omega_Q/2\pi$	15.3 kHz
Normalized intensity	$\hat{s}$	0.2
Phase advance in vacuum	σ_v^{sf}	48°
Ion-neutral collision time	τ_{in}	$\gtrsim 2.0$ sec
Ion-ion collision time	τ_{ii}	$\gtrsim 0.5$ sec
Axial bounce time	τ_b	1.9 msec
Axial beam energy	E_b	3 eV
Axial beam current	I_b	5.4 nA
Axial beam velocity	v_b	2.09×10^3 m/s
Ion thermal velocity	v_t	0.27×10^3 m/s
Ion temperature	T_i	0.1 eV
Space-charge potential	$\phi^s(0) - \phi^s(r_w)$	0.13 V

Table 3.1: Characteristic parameters of the PTSX pure ion plasma. The plasma parameter N_D is the number of particles in a Debye sphere [18].

trap through the axial drift motion. Due to the finite axial beam velocity, the collected charge signal is effectively averaged over dozens of oscillation periods $T = 1/f_0$. The reproducibility of this process allows us to construct a radial charge profile out of multiple measurements at different radial positions of the collector for each shot. In addition, by trapping the plasma with different time durations, the time evolution of the trapped plasma properties can also be measured. No bias voltage is applied to the collector plate, otherwise ion motion will be affected by the position of the charge collector. The time duration of dumping (t_d) should be longer than the axial bounce time (τ_b), and is normally set to $t_d \geq 15$ ms to make sure the trap becomes empty. In the dumping stage, the inherent beam mismatch is present when the charge bunch with line density $N/2$ is separated from the initially matched beam with line density N. The degree of beam mismatch can be given by $\mu = R_{bi}/R_{bf} \approx (1+\delta_b)/(1+\delta_b/2)$. Here, $R_{bi(f)}$ is the initial (final) rms beam radius, and δ_b is the thermal beam intensity parameter introduced in **Chapter 2**. For the case of moderately low space-charge density beams ($\hat{s} = 0.2 \sim 0.3$), it is estimated that $\mu \lesssim 10\%$ and the matched beam profile is projected onto the charge collector without significant perturbation.

Two resting stages are added at the end of the dumping stage to prepare a new cycle. Even though most of the ions have streamed out of the trap during the dumping process, it is observed that there remains a small number of residual ions with extremely low axial velocity. These residual ions are negligible in contributing to a radial charge profile. However, to get rid of any possible accumulated effect of these ions, we switch the voltages of the central and dump electrodes to ground for the time duration Δt_r. The residual ion cloud in the trap will expand toward the grounded electrodes at the thermal speed v_t, and will be neutralized at the room-temperature electrode surfaces [Fig. 3.3(e)]. Normally, we set $\Delta t_r = 5$ ms, which is much longer than the characteristic expansion time $r_w/v_t \sim 0.4$ ms.

Finally, we switch the voltage of the dump electrodes from ground to $+\hat{V}$ and make the system ready for the new cycle [Fig. 3.3(f)]. The time duration of resting (t_r) can be arbitrarily chosen for $t_r > \Delta t_r$, and is used to set the total cycle time t_{cycle} to a desired value.

Detailed analysis and further discussion of the injection process outlined here are presented in **Chapter 4** of this thesis.

3.2.2 Vacuum System

The PTSX vacuum chamber is 134.5 in. in overall length, and consists mainly of a 10 in. O.D. electropolished stainless-steel chamber with Conflat (CF) metal-seal flanges (Fig. 3.4). Aluminum rings with teflon and vespel insulating spacers support the electrodes while keeping them electrically isolated from the vacuum chamber. A centrally-located, six-way cross accommodates the laser-induced fluorescence (LIF) diagnostic described later in this chapter. The chamber is enclosed by custom-made baking jacket (Fig. 3.5) whose temperature is monitored by two thermocouples (TC) and adjusted by proportional-integral-derivative (PID) controllers. Considering the permissible temperature ranges of the lead-free solder ($\lesssim$ 220 °C) and insulating spacers ($\lesssim$ 260 °C) used inside the vacuum chamber, the maximum baking temperature is set to be 200 °C. The PTSX device is evacuated using a turbomolecular pump (TMP) with a pumping speed of 1000 ℓ/sec, which is backed by an oil-free (dry) scroll-type roughing pump (RP) with a pumping speed of 600 ℓ/min. The maximum forevacuum pressure of the TMP is 10 Torr, and the ultimate pressure is 7.5×10^{-11} Torr. The pumping utilizes a "T" section near the injection electrodes in order to ensure good conductance. Changes in operating pressure are measured with a nude ionization gauge (IG) near the dump electrodes. As shown in Fig. 3.6, the foreline and vent pressures are measured by convectron gauges (CG). In order to prevent neutral collisions from affecting the plasma behavior, the base pressure of PTSX is kept below 5×10^{-9} Torr after a week-long bake at 200 °C. When the ion source is on, the operating pressure rises up to $10^{-8} \sim 10^{-7}$ Torr. Even in this case, the characteristic ion-neutral collision time is $\tau_{in} \gtrsim 2$ sec, and the trapped plasma is collisionless to very good approximation.

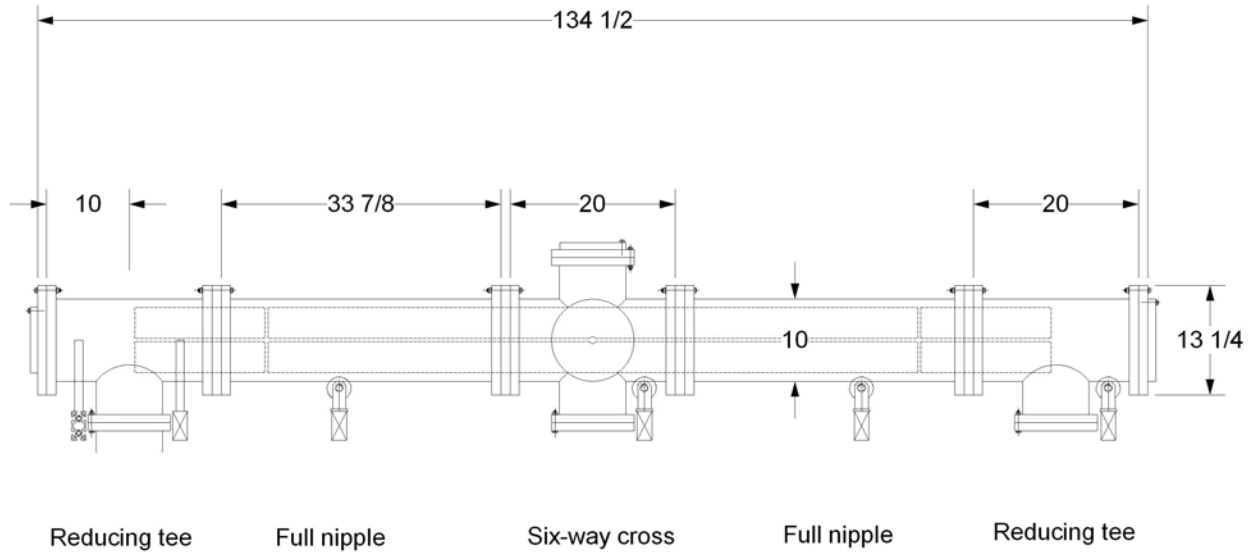

Figure 3.4: Schematic drawing of the PTSX vacuum flanges. Electrodes inside the flanges are indicated by the dashed lines. All dimensions are in inches [88].

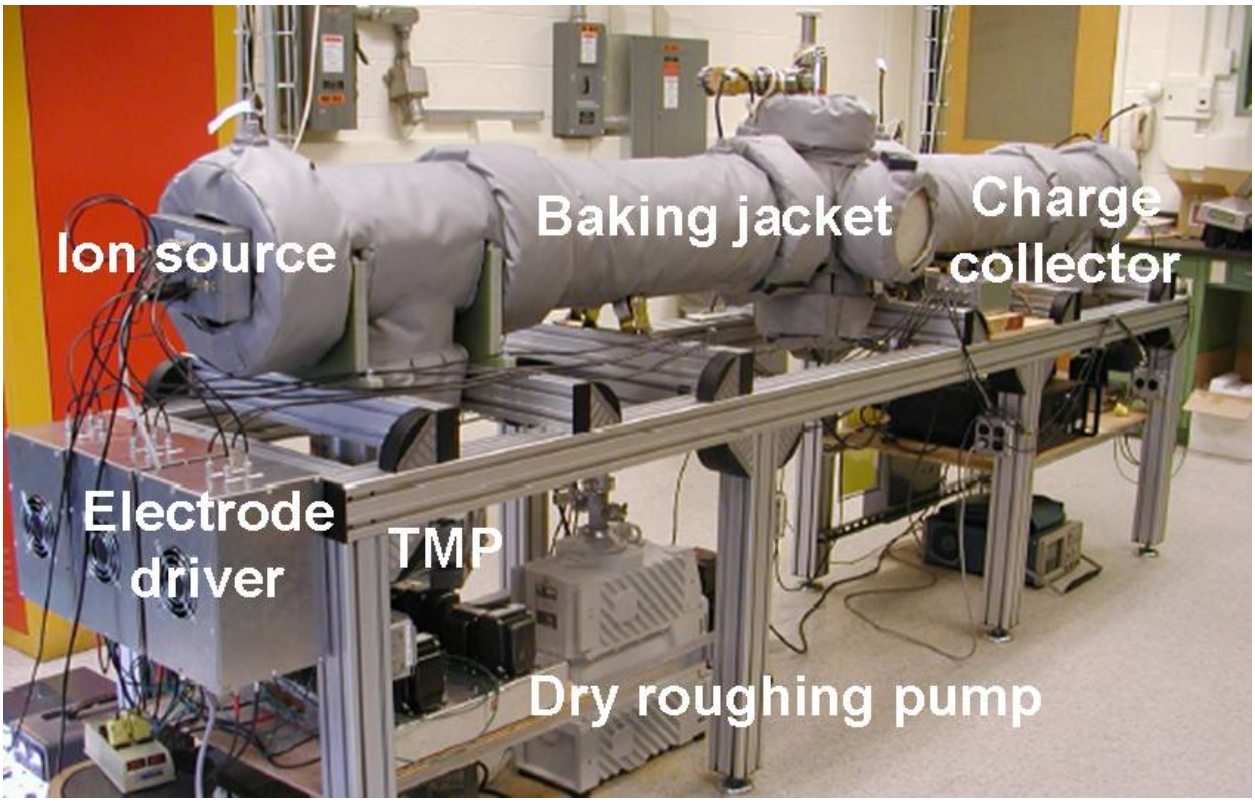

Figure 3.5: Photograph of the PTSX device.

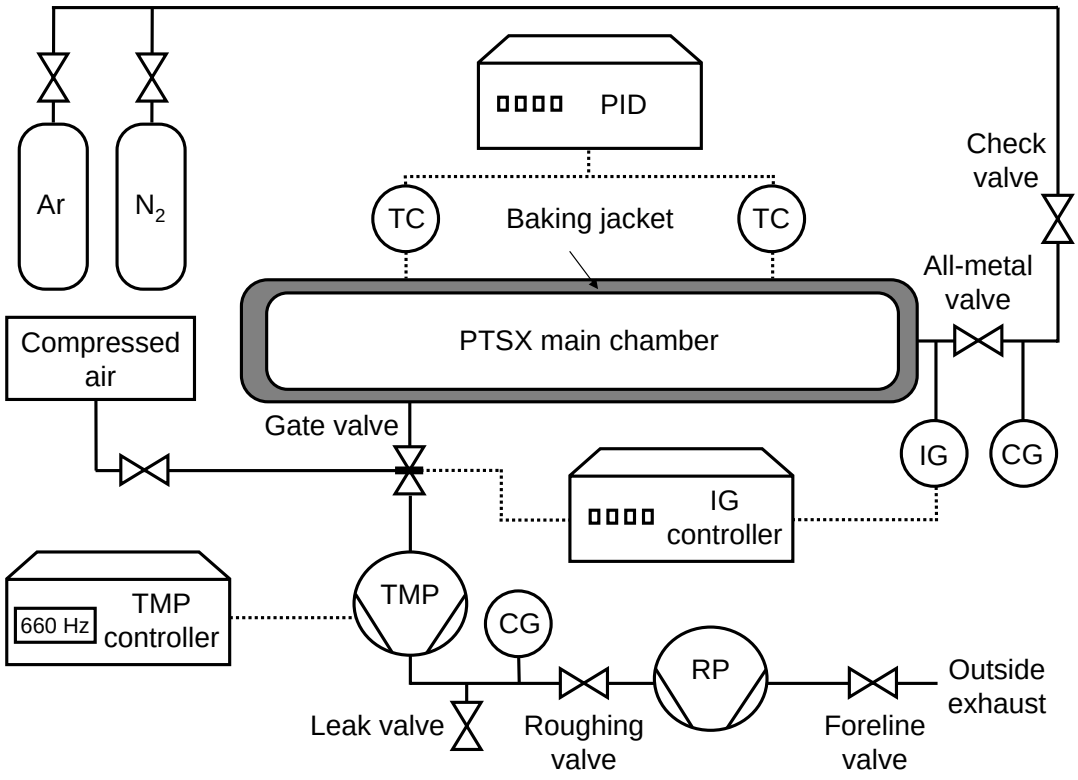

Figure 3.6: Schematic diagram of the PTSX vacuum system. Solid lines represent the flow of gas, while dotted lines represent the electrical signals [88].

3.2.3 Electrode Control System

To apply the oscillatory voltage $\pm V_0(t)$, a National Instruments 5411 Arbitrary Function Generator Card (NI PCI-5411) with a 20 MHz clock rate and a 2 M-sample, 16-bit waveform memory is used. This PCI card has a single analog output connector whose voltage levels are ± 5 V with 12-bit resolution for nominal 50 Ω load termination. The memory architecture of the card imposes certain restrictions on the waveform size and resolution. The minimum size of a single waveform is 256 samples and the number of samples must be divisible by 8. For a 20 MHz clock rate, the time resolution becomes $\Delta t = 1/(20\text{ MHz}) = 50$ nsec. These requirements adjust the actual frequency of a single waveform according to

$$\frac{n_1}{f_0 + \Delta f} = \{256 + 8(n_2 - 1)\}\,\Delta t, \tag{3.1}$$

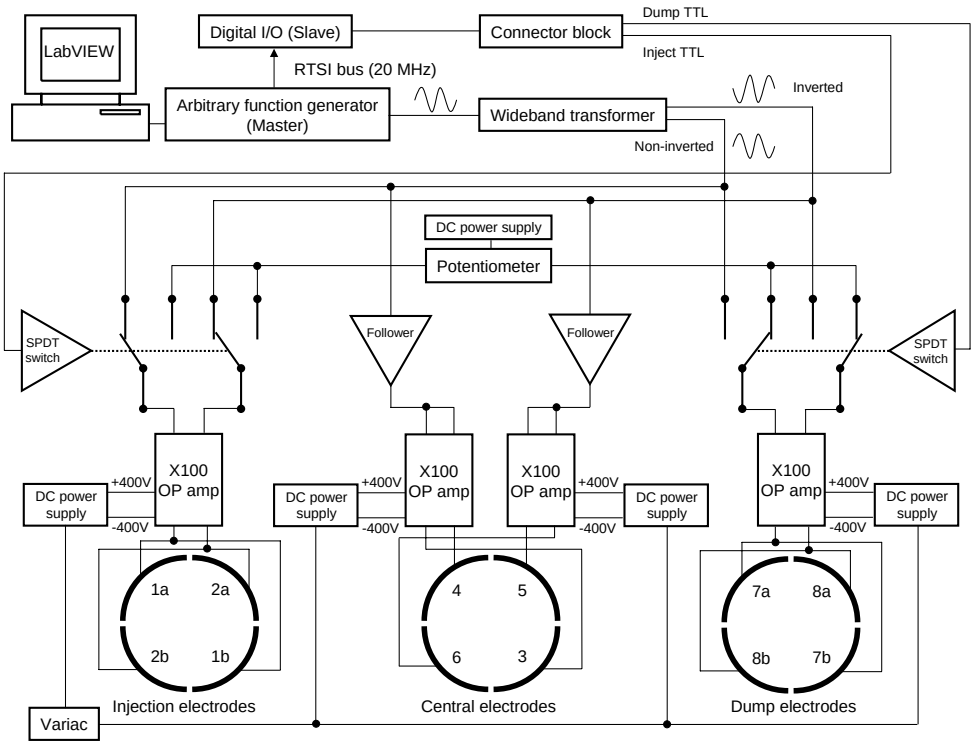

Figure 3.7: Schematic diagram of the PTSX electrode control system. [88]

where f_0 is original desired frequency, $f_0 + \Delta f$ is adjusted frequency, and n_1 and n_2 are positive integers that minimize $|\Delta f|$. For example, if we set $f_0 = 60$ kHz, then from Eq. (3.1), $n_1 = 1$, $n_2 = 11$, and the final frequency is adjusted to $f_0 + \Delta f = 59.5238$ kHz. Such a slight adjustment in frequency is not noticeable for most of the PTSX experiments, except for the aliasing pattern in the on-axis density oscillation presented in **Chapter 4** of this thesis. By looping a single waveform many times and linking different waveforms together, a long arbitrary waveform is generated to simulate a wide variety of periodic-focusing quadrupole lattice patterns.

To create the train of TTL (Transistor-Transistor Logic) pulses that controls the timing of the injecting, trapping, and dumping of the plasma, a National Instruments 6534 Digital I/O Card (NI PCI-6534) is used. We use 3 channels of the PCI card that switch on and off the bias voltages of the injection electrodes, dump electrodes, and emission surface. The output of each channel is either 5 V for "On", or 0 V for "Off". For example, an "On" signal

(5 V) switches the voltages of the short electrodes from $\pm V_0(t)$ to a DC bias $+\hat{V}$, and closes the trap so that no ions can pass through. On the other hand, an "Off" signal (0 V) switches the voltages from $+\hat{V}$ to $\pm V_0(t)$, allowing ions to pass through the short electrodes.

To prevent an unwanted phase slipping between the waveform from the NI PCI-5411 and the TTL pattern from the NI PCI-6534, the two cards are made to share a common 20 MHz clock. Moreover, to ensure synchronization, a marker pulse is added to the very beginning of the first waveform of the NI PCI-5411. This marker pulse is used to initially trigger the NI PCI-6534 via the RTSI (Real-Time System Integration) bus line to start the TTL pattern generation.

As illustrated in Fig 3.7, the waveform signal from the arbitrary function generator is transferred into $+V_0(t)$ and $-V_0(t)$ by unit-gain non-inverting and inverting op amps. These $+V_0(t)$ and $-V_0(t)$ signals are sent to a set of solid-state SPDT (Single Pole Double Throw) switches. Based on the TTL pattern from the digital I/O card, the switches allow the end electrodes to receive either the DC voltage $+\hat{V}$ for trapping, or $\pm V_0(t)$ for injecting and dumping the plasma. The amplitude of the DC voltage $+\hat{V}$ is adjusted by a potentiometer from 36 to 150 V. The central electrodes always have a voltage waveform $\pm V_0(t)$, but can be biased to ground by setting $|V_0(t)|_{\max} \equiv \hat{V}_0 = 0$ V.

The signals are then sent to high-voltage operational amplifiers (Apex Microtechnology PA94) with ± 400 V supply voltages (Fig. 3.8). The system can apply signals up to $\hat{V}_0 = 400$ V and $f_0 = 100$ kHz to the electrodes. These limits are set by the supply voltage limit, the 100 mA continuous output current limit, and the frequency bandwidth of the operational amplifiers. To eliminate high-frequency noise on the voltage input V_{in}, an input bypass capacitor has been added, setting the 3dB point of the low-pass filter at $f_{3\text{dB}} \approx 400$ kHz. The voltage gain of this inverting amplifier is $-V_{\text{out}}/V_{\text{in}} = 100$. To ensure stable operation of the amplifier at such a high gain, a compensation capacitor C_C of 2.2 pF and a current limit resistor R_{LIM} of 7.5 Ω are added. For overvoltage protection, general-purpose 1N914 diodes are used on the input voltages and unidirectional zener diodes are used in the supply voltages.

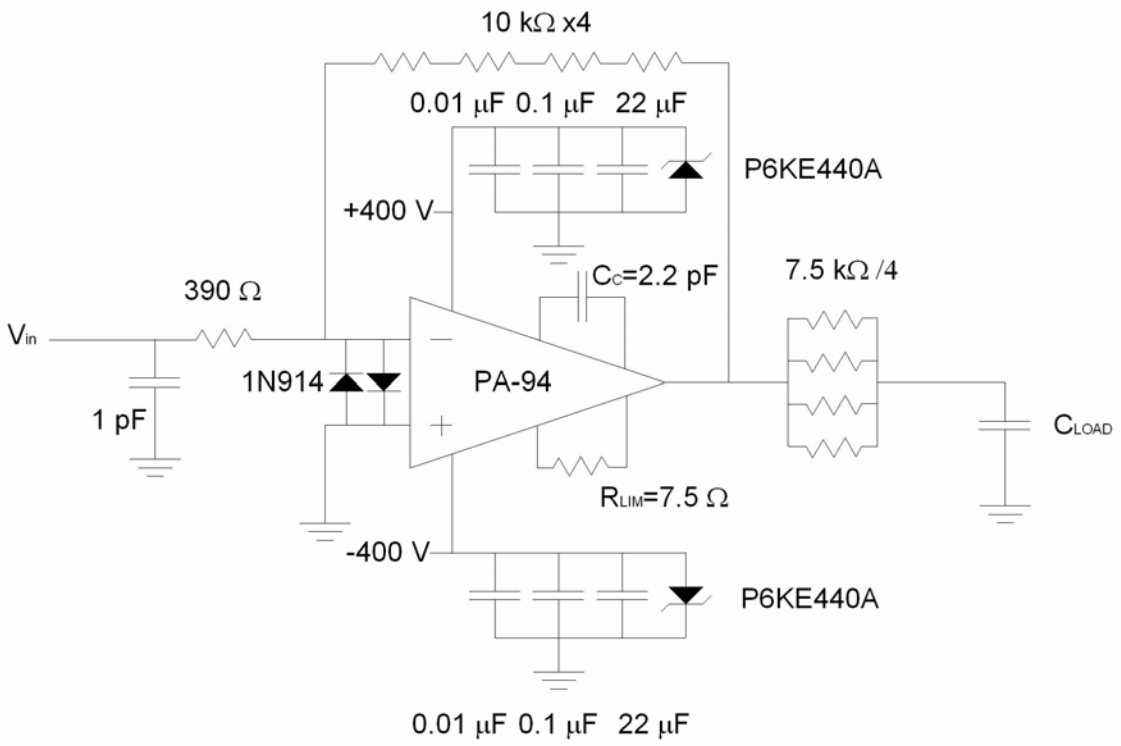

Figure 3.8: Schematic circuit diagram of the PTSX electrode driver.

Each electrode of the PTSX device represents a capacitive load and draws increasing current at higher frequencies. The capacitances of the long and short electrode sectors are measured to be ~ 270 pF and ~ 90 pF, respectively [7]. These capacitances are measured by a simple capacitive voltage divider with respect to ground. To achieve stability in driving purely capacitive loads, a load resistance of 1.875 kΩ is added on the voltage output, making the load not purely capacitive, and all the BNC cables ($\sim$ 30.5 pF/ft) which deliver voltage signals to the electrodes are made to have the same lengths of about 30 cm. A variac sets the power supply voltage. Even though a heatsink, a thermal washer, and a cooling fan maintain the temperature of the system properly, the extra heat produced by high-voltage and high-speed operation occasionally damages the operational amplifier (on the average once a year for 8 copies of the electrode driver).

3.3 Cesium Ion Source

Cesium ions (Cs^+) were used in the initial phase of the PTSX experiment because of cesium's large mass (133 amu) and the commercial availability of sources. The ion source consists of a 0.6 in. diameter aluminosilicate cesium emitter (Heatwave Labs TB-118) surrounded by a Pierce electrode, followed by an acceleration grid and a deceleration grid (Fig. 3.9). This triode grid system has flexibility to change the extraction field strength without changing the beam energy. In practice, we usually ground the bias voltage on the deceleration grid and fix the bias voltage on the Pierce electrode. By varying the bias voltage on the acceleration grid, we can inject a reasonable range of ion currents while keeping the charged particle energy constant. Cesium oxide, Silicon oxide, and Aluminum oxide are melted into the emitter surface, which is an extremely porous tungsten disc welded to the molybdenum heater body. When the emitter surface is heated, cesium oxide decomposes and cesium ion is produced through contact ionization with tungsten which has a high work function ($\sim$ 4.55 eV). The heater is a non-inductively wound coil of molybdenum wire solidly potted into the molybdenum body with high purity alumina (Al_2O_3). A DC power supply is connected to the heater, keeping the source temperature 900 $\sim$ 1200 °C with 7 $\sim$ 13 A of applied current. The thermionic electron emission from the emission surface is negligible. In any event, electrons cannot be confined in PTSX due to their small mass.

The Pierce electrode is made of copper and has a 67.5° opening angle to compensate for possible beam divergence due to space-charge forces [100]. Because the ion beam energy is relatively low in the PTSX experiment, 85% transparent electroformed copper meshes have been used for the fabrication of the acceleration and deceleration grids. To avoid the possible formation of a virtual cathode (i.e., an axial potential structure generated by space charge), we set the distance between the emission surface and acceleration grid (d_1) to be larger than the distance between the acceleration and deceleration grids (d_2), i.e., $d_1 > d_2$ [101]. While the two grids and the Pierce electrode are electrically insulated using machinable ceramic spacers, the emission surface is biased with the voltage of the Pierce electrode. The amount

(a) Aluminosilicate cesium ion source.

(b) Pierce electrode.

(c) Acceleration (or deceleration) grid.

(d) Ion source assembly.

Figure 3.9: Photographs of the cesium ion source.

of charge injected can be controlled easily by adjusting the voltages on the emitter surface (V_s), acceleration grid (V_a), and deceleration grid (V_d) of the ion source. Normally, we set $V_s > V_a > V_d \geq 0$ V to minimize the effects of virtual cathode. The voltage difference between the emitter surface and the acceleration grid determines the extraction voltage $V_e = V_s - V_a$, and the voltage difference between the emitter surface and the deceleration grid adjusts the axial beam velocity $v_b = \sqrt{2q(V_s - V_d)/m}$.

In Fig. 3.10, we present the axial beam current $I_b = qNv_b$ measured by allowing the ions to stream directly from the source to the large copper plate at the diagnostic end electrodes

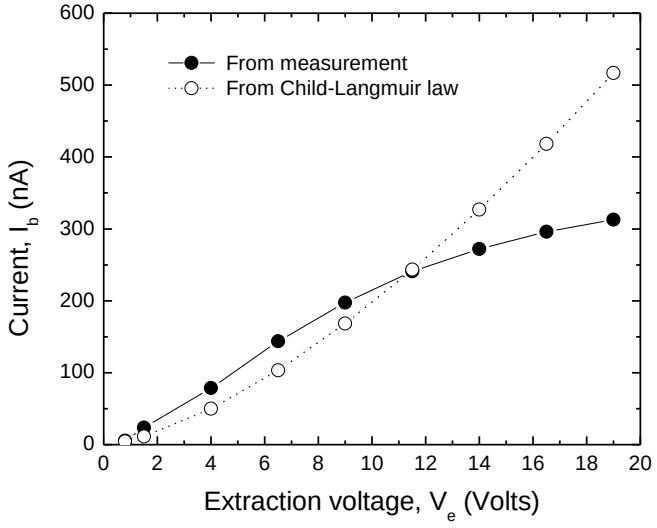

Figure 3.10: The current extracted from the source actually collected on the large copper plate at the diagnostic end electrodes (solid circles) and estimated from the Child-Langmuir law (open circles).

for different values of extraction voltage V_e. For the case of space-charge-limited flow [16,21], it is expected that $I_b \approx I_{\rm CL}$ from current density conservation. Here, the Child-Langmuir current $I_{\rm CL}$ is estimated by $I_{\rm CL} \approx (4\epsilon_0/9d_1^2)(2q/m)^{1/2}V_e^{3/2} \times \pi r_s^2 \times (0.85)^2$, where r_s is the radius of the emission surface, and $(0.85)^2$ term represents transparency of the grids. Figure 3.10 shows, however, that I_b depends linearly on V_e rather than the $V_e^{3/2}$ scaling of the Child-Langmuir law for $V_e \lesssim 10$ V. On the other hand when $V_e \gtrsim 10$ V, I_b is saturated and becomes much smaller than $I_{\rm CL}$. Despite the departure from the Child-Langmuir law, this control allows us to fill the trap with a wide range of ion densities.

3.4 Radially Scanning Charge Collector

3.4.1 Mechanical Description

The primary diagnostic on PTSX is a radially scanning charge collector on the dumping end of the device. The charge collector is mounted on a linear motion feedthrough with a 6-in. stroke that allows the assembly to go from 2 in. beyond the device center to being completely

withdrawn from the trap. The original charge collector was based on a commercially-available Faraday cup that consists of a stack of three 0.75-in. by 1.5-in. plates that support the cup and has small apertures. In order to reduce the effect of stray charge striking the edges of these plates and confounding the measurements, the assembly was enclosed in a copper box that measured 1 in. across by 3 in. tall, and was not symmetrically placed about the collection aperture. This resulted in a boundary condition for the electric potential that varied as the Faraday cup was moved, and this was evidenced in the data as an offset in the position of the peak charge density. To assure a boundary condition that is independent of the position of the Faraday cup, a slotted 8-in. diameter copper disk was placed in front of the Faraday cup. Although this eliminated the dependence of the measurement on the position of the Faraday cup, the dumped plasma now broadened significantly as it approached the diagnostic. The time-dependent oscillating voltage that normally confines the plasma radially, gradually became a constant axial field in the vicinity of the copper disk, and there is no longer a transverse confining field.

The original Faraday cup has been replaced by a charge collector with a simpler design on PTSX [102]. Figure 3.11(a) shows a schematic of the final charge collector, and Figs. 3.11(b) and (c) show photographs of the final collector in place in PTSX. The 5 mm diameter head of a copper nail now serves as the collection surface. A coaxial wire is connected to the body of the nail, and the wire and nail are inserted into a thin, alumina rod that insulates the collector from the conductive support rod. The ceramic rod, in turn, is inserted into a 3/16 in. diameter, stainless steel support rod. The base of this rod is clamped into a block that sits atop the arm of the linear motion feedthrough. Thus, the collection surface sits approximately halfway into the dumping electrodes, thereby avoiding fringe fields. Since this thin support rod is grounded and moves in a null of the fully time-dependent voltage, the charge collector has a minimum impact on the potential structure within the dumping electrodes. Measurements show that the radial charge profile no longer exhibits the broadening associated with the equipotential copper disk used previously, and the profile is

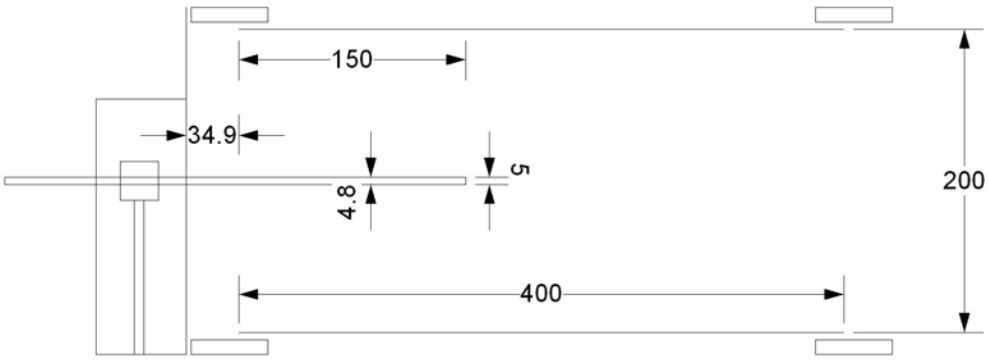

(a) The charge collector plate is placed transversely at a null of the applied quadrupole potential and axially away from the the fringe fields. All dimensions are in mm.

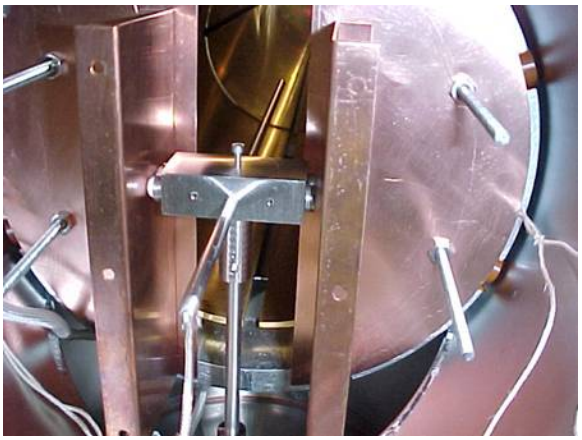

(b) The charge collector is guided in the horizontal direction by a pair of copper plates attached to a slotted copper disk at the end of the PTSX device.

(c) The 5 mm diameter head of a copper nail serves as the collection plate.

Figure 3.11: Schematic drawing and photographs of the charge collector.

well-centered. Moreover, because of the low axial kinetic energy of the ions, there is no need for an additional structure to suppress secondary electron emission.

3.4.2 Model 6514 Electrometer

The Model 6514 electrometer [103] makes charge measurements with 10 fC resolution. In the electrometer, an accurately known capacitor is placed in the feedback loop of the amplifier so that the voltage developed is proportional to the charge, which is the integral of the input

current. The voltage is then scaled and displayed digitally as charge. The integration time of the A/D converter affects the amount of reading noise, as well as the ultimate reading rate of the charge measurement [104]. The integration time is specified in terms of the number of power line cycles (PLC), where 1 PLC for 60 Hz is 16.67 ms. If the A/D converter integrates for an amount of time equal to an integer number of 1 PLC, then the signal components from the power line noise, which tend to be periodic, can be cancelled. In the PTSX device, charge measurement is optimized for a 6 PLC reading rate which corresponds to a 100 ms integration time. In addition, to reduce the periodic noise from the AC/DC switching of the end electrodes, the cycle time t_{cycle} is set to be a divisor of the integration time. Figure 3.12 indicates that setting t_{cycle} to be a divisor of the integration time averages out coupling from the electrodes and makes background signal less noisy.

In the charge measurement using the electrometer, the input offset current is usually very low. However, for low level charge measurements, as in the PTSX device, even this small offset current can generate a significant error factor after long-time integration. The typical input offset current in the Model 6514 electrometer is about 4 fA, which will cause the offset in the charge measurement Q_{offset} to be about 0.4 fC for $t_{\text{cycle}} = 100$ ms. Due to the temperature dependence of the input offset current and a number of other external current sources in the system, it is very difficult to determine the exact offset current of the entire system and subtract it from the actual reading. A general rule of thumb is to set $Q_{\text{offset}} \sim 1$ fC and cut off the charge measurement when $Q(r) < Q_{\text{offset}}$, allowing an additional uncertainty associated with subtracting the offset. Other unwanted currents can result from triboelectric effects, electrostatic interference, and magnetic fields. Triboelectric currents are generated by charges created between a conductor and an insulator due to friction [104]. In the PTSX device, insulated cable delivering collected charges inside the vacuum chamber creates some noise when subjected to expansion and contraction. One easy solution is to wait several seconds after moving the position of the charge collector. Electrostatic interference is recognizable when hand or body movements near the experiment cause erroneous or unstable

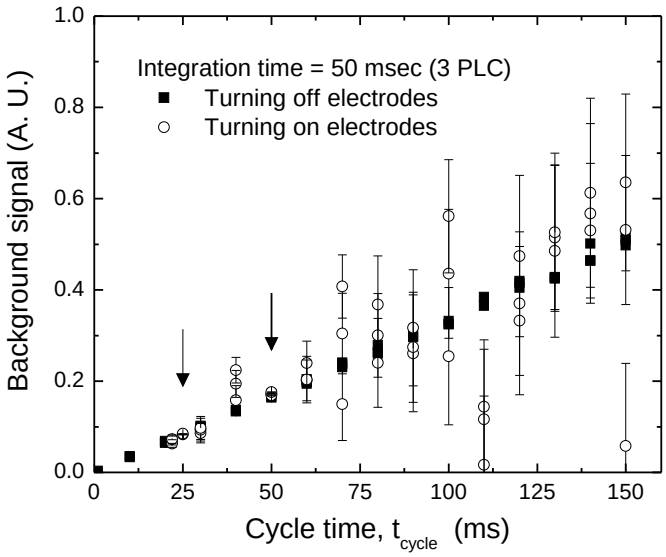

(a) Integration time = 50 msec (3 PLC).

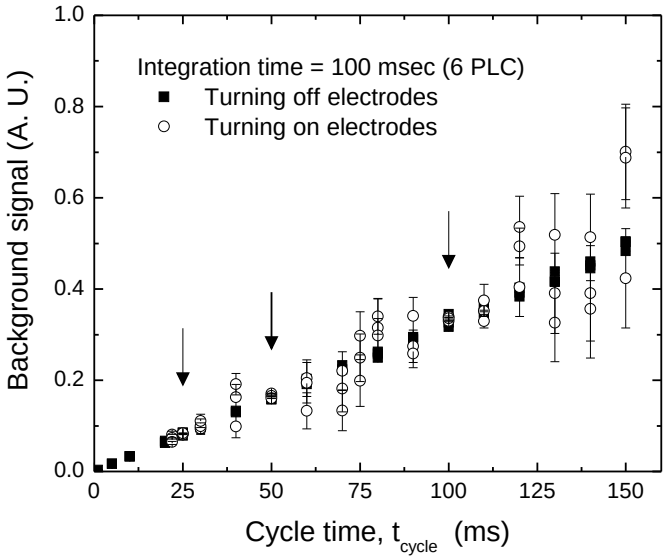

(b) Integration time = 100 msec (6 PLC).

Figure 3.12: The background signal measured without trapped ions is linearly proportional to the cycle time of PTSX operation. When the electrodes are turned on, the background signal becomes noisy (open circles). Setting the cycle time to be a divisor of the integration time averages out coupling from the electrodes (indicated by arrows). Considering that the dumping time is $t_d \geq 15$ ms, the cycle time is usually set to be $t_{\text{cycle}} \geq 25$ ms.

readings. Magnetic fields from neighboring experiments can also introduce fluctuations in the readings.

In calibrating the internal voltage offset of the electrometer, which drifts with time and temperature, we perform zero check and zero correction for every charge measurement. The zero check feature provides a mean for internal zero verification, and the zero correction feature corrects the internal offset so that the display reads zero with no input signal. When turning on the zero check feature, the accumulated charges in the charge collector and the BNC cable dissipate through the 10 MΩ resistor. After turning off the zero check feature, a new measurement cycle begins. However, the residual charges remaining in the system often cause sudden changes in the charge reading (known as zero check hop). This effect gives rise to a nonlinear increase in charge in the initial phase of the measurement (see Fig. 3.13), which becomes significant particularly for low charge level. A convenient way to deal with this effect is to avoid the nonlinear regime by starting the charge measurement several seconds after the zero check. The measured charge signal is transferred to a LabVIEW program of PC in the ASCII data format through a GPIB interface. The Model 6514 electrometer can be used within one minute after it is turned on. However, it should be allowed to warm up for at least one hour to achieve optimum performance.

3.4.3 Radial Profile and Inferred Quantities

If the true density profile $n(r')$ is uniform in the z direction and axisymmetric in the smooth-focusing approximation, the total charge collected per cycle $Q(r)$ by the collector plate centered at radius r can be related to $n(r')$ as

$$Q(r) = qL_p \int_0^{r_c} \rho d\rho \int_0^{2\pi} d\theta n(r'), \tag{3.2}$$

where $r' = (r^2 + \rho^2 - 2r\rho\cos\theta)^{1/2}$ is the local radius, r_c is the size of the circular collecting plate, and L_p is the plasma length, which can be estimated either from numerical simulations or the analytical formula for the axial potential distribution (see **Appendix A of [88]**). To increase the collected charge signal out of a low beam current density, the size of the charge

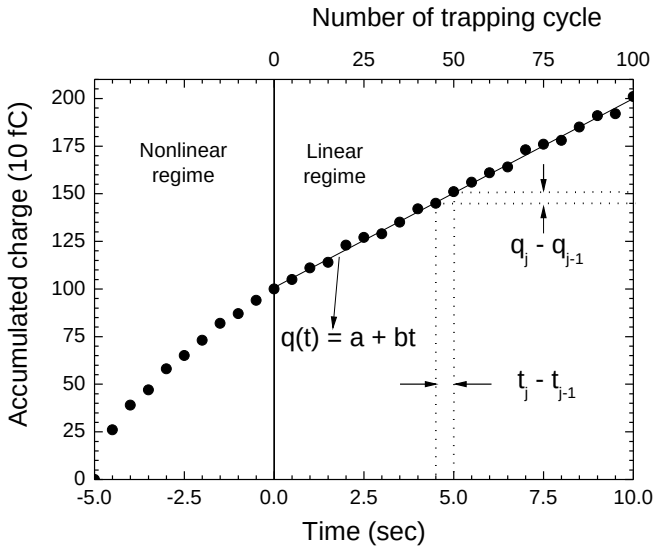

Figure 3.13: Illustrative example of repeated charge measurement. The resolution of the accumulated charge measurement is 10 fC, which is set by the electrometer. We wait for 5 sec (or more, if necessary) and collect data only in the linear regime for 10 sec, which corresponds to 100 trapping cycles for $t_{\rm cycle} = 100$ ms. Due to the finite speed of the GPIB communication between the electrometer and the LabVIEW interface, the total number of data readout N_t is about 20 out of 100 cycles.

collector has been chosen to be $r_c = 2.5$ mm, which is much larger than the opening of the commercial Faraday cup ($r_c \lesssim 0.5$ mm). By noting that the typical density profile in the PTSX device is close to Gaussian, we obtain

$$n(\bar{r}) \approx \frac{Q(r)/q}{\pi r_c^2 L_p}, \tag{3.3}$$

where for $r \lesssim r_c$, $\bar{r} \approx [r^2 + r_c^2/2]^{1/2}$, and for $r > r_c$, $\bar{r} \approx r\,[1 + O(r_c^2/r^2)]$. The exact on-axis density $\hat{n} = n(r = 0)$ can be approximately determined by extrapolation from the two nearest data points to $r = 0$.

The mean-square radius of the trapped plasma column can be calculated from either $n(r)$ or $Q(r)$ according to

$$R_b^2 = \left\langle r^2 \right\rangle = \frac{1}{N} \int_0^{r_w} dr 2\pi r r^2 n(r) \approx \frac{1}{Q_b} \int_0^{r_w} dr 2\pi r r^2 Q(r), \tag{3.4}$$

where $N = 2\pi \int_0^{r_w} drrn(r)$ is the line density, and $Q_b = 2\pi \int_0^{r_w} drrQ(r)$ is the total charge in the trap for one cycle. The integrals are evaluated numerically using the Simpson rule with relative errors of order $(\delta r_i/R_b)^5$, where δr_i is the radial spacing between measurements, which is typically 2.54 mm. Since the collected charge is necessarily averaged over many focusing periods, the values of R_b calculated from Eq. (3.4) can be interpreted as the rms radius of the beam in the smooth-focusing approximation. The effective transverse temperature $\bar{T}_\perp$ of the ions is inferred from global force balance equation as [1]

$$\bar{T}_\perp = \frac{1}{2}\left[m\omega_q^2 R_b^2 - \frac{Nq^2}{4\pi\epsilon_0}\right]. \tag{3.5}$$

This temperature is a measure of the average (random) kinetic energy of the beam particles in the smooth-focusing equilibrium. For a matched beam in thermal equilibrium, $\bar{T}_\perp$ is approximately equal to the thermal temperature of the ion source, i.e., $\bar{T}_\perp \approx T_s$. Furthermore, the average transverse emittance in the beam frame can be estimated as

$$\epsilon \approx 2R_b\left(\frac{2\bar{T}_\perp}{m}\right)^{1/2}. \tag{3.6}$$

3.5 Summary and Discussion

In this chapter, the Paul Trap Simulator Experiment (PTSX) apparatus has been described in detail. For the PTSX device to confine and detect the pure ion plasma with parameters relevant for the simulation of the intense beam in the alternating-gradient (AG) focusing system, the device configuration, electrode control system, vacuum system, ion source, and charge collector have been carefully designed and installed. Initial experiments with a cesium ion source and a radially scanning charge collector diagnostic, which will be presented in **Chapters 4** of this thesis, demonstrate the wide operating range and the large degree of flexibility of the PTSX device.

Chapter 4

Collective Mode Excitation and Machine Imperfection Effects

4.1 Introduction

In this chapter, we present a brief review of the theoretical models for collective modes of charged particle beams and discuss the excitation of those collective modes and their effects on beam parameters. Effects of machine imperfections on beam qualities will be also be discussed. In Sec. 4.2, we discuss the theoretical models for collective modes. In Sec. 4.3, excitation of quadrupole modes and the characteristics of the quadrupole modes are presented. In Sec. 4.4, excitation of dipole modes and the characteristics of the dipole modes are discussed. In Sec. 4.5, effects of machine imperfections will be presented.

4.2 Quadrupole and Dipole Modes

The long thin charge bunch in PTSX and the charged particle beams in periodic transport systems support a wide range of collective modes, and these modes can be studied in the context of different models. A Kapchinskij-Vladimirskij (KV) distributed beam or charge bunch has uniform number density and Gaussian distributed velocities, with charged

particles entailed by beam envelopes defined by $x^2/a^2(t) + y^2/b^2(t) \leq 1$, where $a(t)$ and $b(t)$ are the x-direction and y-direction envelopes of the beam. Using the assumption of a KV distribution, a great deal of analytic progress has been made in collective mode studies [1, 51, 56, 105–109]. The frequencies of the surface modes with azimuthal mode number l can be found using the KV Vlasov-Poisson smooth-focusing model in which the KV distribution is used and the time- dependent periodic quadrupole lattice is replaced by a continuous focusing force [1]. Alternatively, a KV smooth-focusing envelope model can be used to derive the expressions of the frequencies of $l = 0$ body mode and $l = 2$ quadrupole mode [38]. We can also numerically study the dependence of mode frequencies of $l = 0$ body mode and $l = 2$ surface mode on space charge using the KV smooth-focusing envelope model with fully time dependent quadrupole lattice. Finally, particle-in-cell (PIC) codes can be employed to create steady state, matched beam distributions that can be perturbed to study the collective modes numerically [57]. For the $l = 0$ body mode, $l = 1$ dipole mode and $l = 2$ quadrupole mode, the analytical expressions for their frequencies can be written as [1, 38]

$$f_{dipole} = f_q = \frac{\omega_q}{2\pi} \tag{4.1}$$

$$f_{quadrupole} = 2f_q \left(1 - \frac{3}{4}\hat{s}\right)^{\frac{1}{2}} \tag{4.2}$$

$$f_{body} = 2f_q \left(1 - \frac{1}{2}\hat{s}\right)^{\frac{1}{2}} \tag{4.3}$$

where ω_q is the average smooth transverse focusing frequency and $\hat{s} = \omega_p^2/2\omega_q^2$ is the normalized intensity which measures the strength of the space charge effect. The dipole mode corresponds to the bulk transverse displacement of the plasma column, and the body mode corresponds to the axisymmetric perturbation of the envelope of the charge bunch, while the quadrupole mode corresponds to the elliptical perturbation of the surface of the charge bunch. In order for the external perturbation to interact with the collective modes, both the spatial structure and the frequency of the external perturbation must be the same as those of the collective modes. In the following sections, we will discuss the excitation of collective

modes and study the interaction between the external perturbation and the collective modes under a wide range of perturbation schemes.

4.3 Excitation of Quadrupole Modes

4.3.1 Beat Drive Scheme

Experimental Results

Quadrupole modes exist naturally in intense charged particle beams. Usually, the amplitudes are very small and they don't cause degradation of charged particle beams. Therefore, to see the effects of quadrupole modes at large amplitude, we need to excite those quadrupole modes externally. Here, two ways to excite the quadrupole modes are considered. One is the beat drive scheme which is discussed in this section. The other scheme is the linear drive scheme which is discussed in Sec. 4.3.2. In our experiments, a combination of sine waves is applied to the four PTSX electrodes:

$$V(t) = V_0 \sin(2\pi f_0 t) + V_1 \sin(2\pi f_1 t) \tag{4.4}$$

where V_0 is the normal unperturbed voltage amplitude applied to the PTSX electrodes, f_0 is the corresponding frequency, V_1 is the perturbed voltage amplitude, usually expressed as a fraction of V_0, and f_1 is the summation of f_0 and the desired mode frequency f_{mode}, i.e. $f_1 = f_0 + f_{mode}$. In PTSX, the typical values for V_0 and f_0 are 140 V and 60 kHz, respectively. The beating between the $V_0 \sin(2\pi f_0 t)$ and the $V_1 \sin(2\pi f_1 t)$ term will create another slow-motion beating term with frequency $f_{beat} = f_1 - f_0$. In other words, we introduced an external perturbation of frequency $f_{beat} = f_1 - f_0$. The typical value of V_1 is about $0.5\% - 1.5\%$ of V_0.

When the external perturbation frequency equals $f_0 + f_{mode}$, the f_{mode} component external perturbation due to the beating between $f_0 + f_{mode}$ and f_0 resonates strongly with the

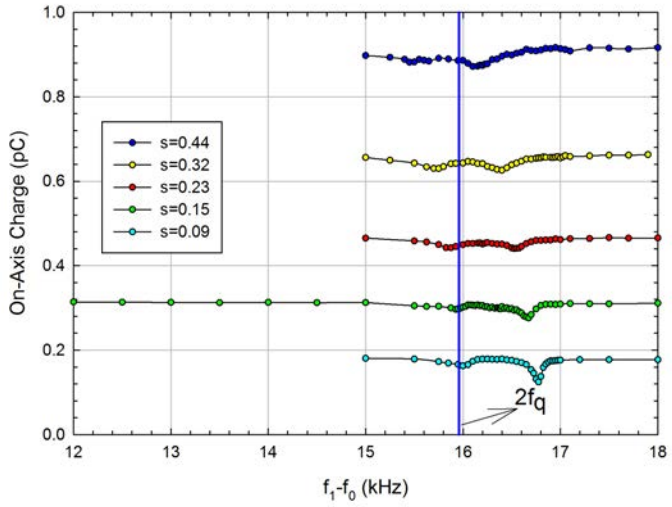

Figure 4.1: On-axis Charge density as a function of $f_1 - f_0$. The results show strong response of the plasma near $2f_q$, while little response was observed when $f_1 - f_0$ was far away from $2f_q$.

collective modes of the charge bunch. The strong resonation acts as an extra energy source which causes the heating of the charge bunch. The on-axis charge density is reduced due to the expansion of the plasma which can be observed in experiments. The experimental results of beat drive scheme are shown in Fig. 4.1. Since the spatial structure of the external perturbation is more likely to excite quadrupole mode, the plasma responds strongly near $2f_q$, the expected quadrupole mode frequency, while there is little response near f_q, the expected dipole mode frequency. There are two noticeable peaks near the quadrupole mode frequency and this is likely due to coupling to other modes that have frequency near $2f_q$. For example, quadrupole mode and the breathing mode have frequencies near $2f_q$. The normalized intensity dependence of the quadrupole mode frequency shown in Fig. 4.1 was measured and the quadrupole mode frequency was plotted as a function of the normalized intensity $\hat{s}$ as shown in Fig. 4.2. The experimental data and the polynomial regression agree well with each other. We also plotted theoretical quadrupole mode frequency together with the experimental data for further comparison. The first term of the regression expression is extremely close to $2f_q$ which agrees with the simple KV smooth-focusing model at small

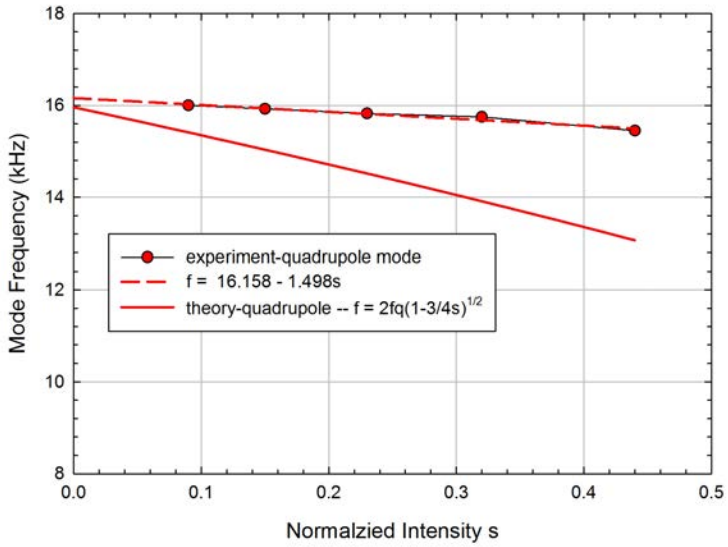

Figure 4.2: Comparison among experimental data, polynomial regression, and the theoretical model for quadrupole mode.

normalized intensity $\hat{s}$. Experimental data shows weaker dependence of mode frequencies on $\hat{s}$ than the theoretical mode. There exists systematic difference between the experimental data and the theoretical model which is demonstrated by consistently higher experimental mode frequencies. See Sec. 4.3.2 for detailed explanation of this discrepancy. The experimental results shown in Fig. 4.1 and 4.2 were obtained by applying 0.5% perturbation on the PTSX electrodes. We saw a strong response of the plasma near the frequency $2f_q$, and didn't see rich mode frequencies at other frequencies. The primary modes (e.g. quadruple mode and breathing mode) are still relatively easy to identify. As we increased the amplitude of the perturbation, the mode excitation and mode coupling became much more complicated when the collective mode was driven to the nonlinear regime. Fig. 4.3 shows on-axis charge density as a function of the beating frequency. Compared to a small perturbation (i.e. 0.5%), the mode structure at a large perturbation(i.e. 1.5%) is more complex and it is difficult to identify which modes have been excited. It is still hard to explain to the mechanism of this behavior at large external perturbations and a much more suitable theoretical model other than simple KV smooth-focusing model is needed to explain the experimental results. In

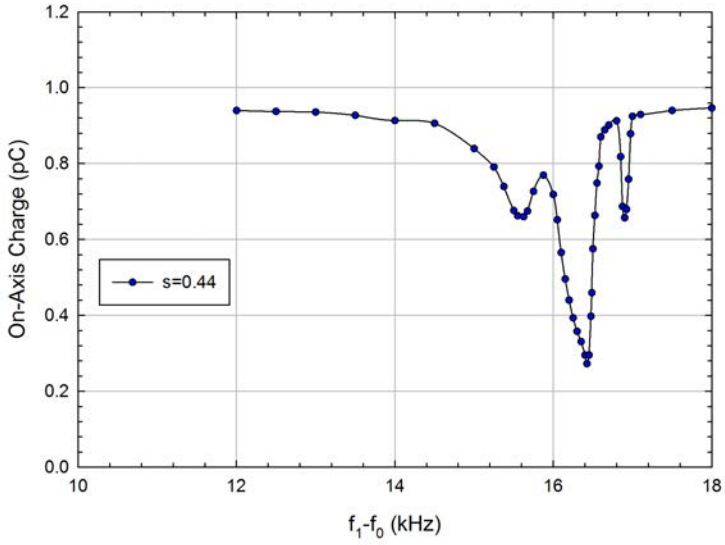

Figure 4.3: On-axis charge density shows much more complicated behavior at 1.5% perturbation than 0.5% perturbation at $\hat{s} = 0.44$.

order to gain some insights, we turn to the Warp 3D simulation which is discussed in the following section.

Warp Simulation Results

In Sec. 4.3.1, we presented the experimental studies of the quadrupole mode excitation using a beat drive scheme. Fig. 4.1 shows the plasma has a strong response near $2f_q$, the expected quadrupole mode frequency, while there is little response at other perturbation frequencies. Fig. 4.2 compares the dependence of the quadruple mode frequency on normalized intensity $\hat{s}$ from experiments with the simple KV smooth-focusing model predicts. The KV model agrees with the experimental results qualitatively, while there exists quantitative discrepancies between the experimental results and the theoretical results. Since the assumptions of the KV model are very strong and don't apply to our circumstances, we turn to Warp 3D simulations to support the experimental results and better under the excitation of the quadrupole mode. In the Warp 3D simulations, we used 0.5% perturbation amplitude all throughout and scanned the perturbation frequency using different initial normalized inten-

sities $\hat{s}$. The charge bunch was injected to the PTSX main chamber and trapped for 100 ms in total. In the first 5 ms, normal oscillating voltage was applied to the PTSX electrodes and the charge bunch gradually relaxed to a steady state. 30 ms external perturbation was applied afterwards, which was followed by 15 ms relaxation time where normal oscillating voltage was applied. We measured the final radial charge density profile, from which we computed other important quantities such as rms radius, transverse temperature, and emittance. The rms radius is computed first from the complete radial density profile. Using the global force balance equation, the transverse temperature kT is calculated. Emittance is computed using rms radius and kT.

Figure 4.4 shows the on-axis number density as a function of $f_1 - f_0$ for several different values of initial $\hat{s}$. Similar to what is shown in the experimental data, the simulation data show strong response near $2f_q$ and the mode structures shown in the simulation are similar to what we saw in the experiment. But unlike the experimental data, there is only one primary peak for most of the simulation data, and this is hard to explain. Since the spatial structure of the perturbation is more favorable to the excitation of the quadrupole mode, we treat only the conspicuous mode as the quadrupole mode. Not only did the simulation confirm the existence of the quadrupole mode, it also provided a tool to study the dependence of the quadrupole mode frequency on $\hat{s}$. Figure 4.5 shows the comparison of dependence of quadrupole mode on $\hat{s}$ between experiment, simulation and KV smooth-focusing model. The simulation and the experiment agreed well with each other, while both of them differed from the KV model significantly.

In addition to studying the dependence of mode frequencies on $\hat{s}$, we also use Warp 3D simulations to study the properties of the charge bunches such as rms radius, transverse temperature, emittance under external perturbation. Fig. 4.6 shows the changes of rms radius, transverse temperature and emittance as perturbation frequency changed. When the perturbation frequency equals to $f_0 + f_{mode}$, strong resonance occurred and the charge bunch was heated by the extra energy which caused the expansion of the charge bunch.

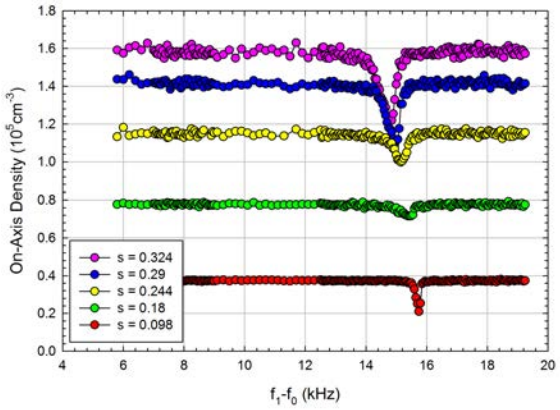

(a) On-axis number density vs $f_1 - f_0$ in the whole frequency range

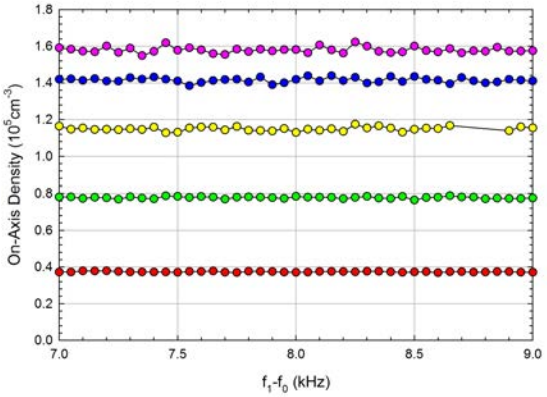

(b) On-axis number density vs $f_1 - f_0$ between 7 kHz and 9 kHz

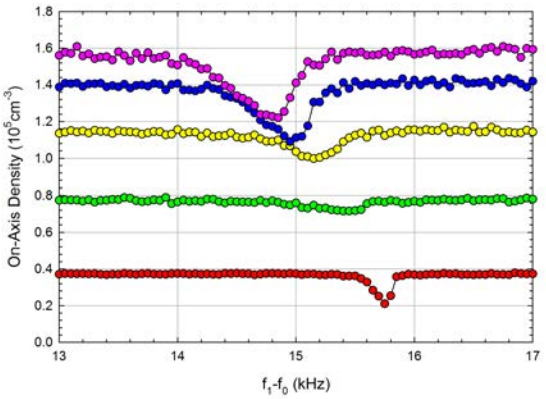

(c) On-axis number density vs $f_1 - f_0$ between 13 kHz and 17 kHz

Figure 4.4: On-axis number density as a function of $f_1 - f_0$ under different $\hat{s}$. Different initial $\hat{s}$ are chosen to study the mode frequency dependence on $\hat{s}$. The charge bunch shows strong response to the perturbation near $2f_q$, while having little response at other frequencies.

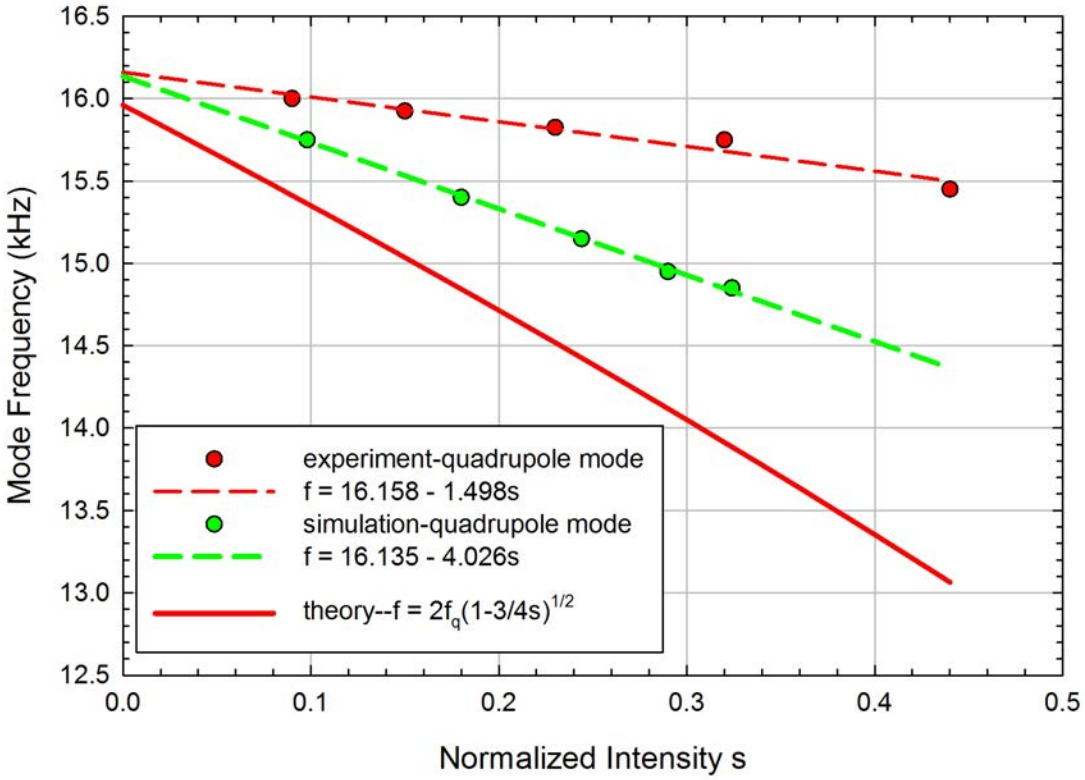

Figure 4.5: Comparison of dependence of quadrupole mode frequency on $\hat{s}$ between experiment, simulation and KV smooth-focusing model. The experiment and simulation results agree well with each other, while both of them differs from the KV smooth-focusing model significantly.

Both the rms radius and the transverse temperature increased accordingly. Some particles are eventually lost when they drift too far away from the center. So usually particle loss is accompanying the resonance. The resonance intensity decreased as $f_1 - f_0$ moved away from the mode frequency which resulted in the quasi-bell shape of the plots. The final radial density profiles with initial $\hat{s} = 0.18$ at different perturbation frequencies were plotted and compared to one another to show the effects of charge bunch expansion. Fig. 4.7 shows the radial density profiles at different perturbation frequencies with initial $\hat{s} = 0.18$. As the resonance occurred, the charge bunch expanded and the on-axis charge density dropped accordingly. Since the resonance between the external perturbation and the collective modes of the charge bunch causes beam degradation, resonance should be avoided. It is still unclear how exactly the external perturbations interacts with the collective modes of the charge bunch. This will be further investigated in future research.

4.3.2 Linear Drive Scheme

Experimental Results

We have discussed above the excitation of collective modes and the interaction between the external perturbation and the collective modes using the beat drive scheme. In this section, a linear drive scheme is used to excite the collective modes. The oscillating voltage applied to the PTSX electrodes is also a summation of sine waves expressed as:

$$V(t) = V_0 \sin(2\pi f_0 t) + V_1 \sin(2\pi f_1 t) \tag{4.5}$$

where V_0 is the normal unperturbed voltage amplitude applied to the PTSX electrodes, f_0 is the corresponding frequency, V_1 is the perturbed voltage amplitude, usually expressed as a fraction of V_0, and f_1 is the frequency of the perturbation. In PTSX, the typical values for V_0 and f_0 are 140 V and 60 kHz, respectively. Typically, V_1 is $0.1\% - 1\%$ of V_0. As opposed to the beat drive scheme, the linear drive scheme uses the perturbation voltage to directly

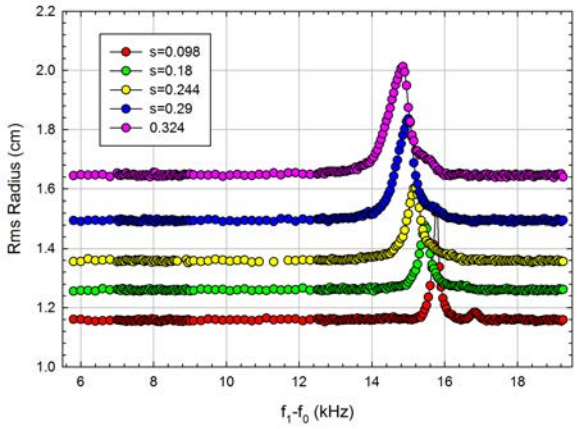

(a) Rms radius vs $f_1 - f_0$

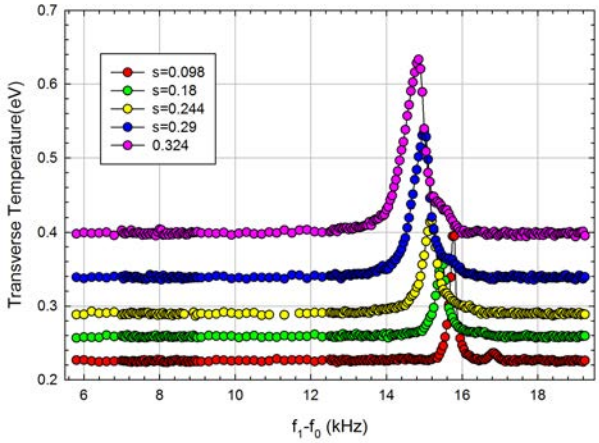

(b) Transverse temperature vs $f_1 - f_0$

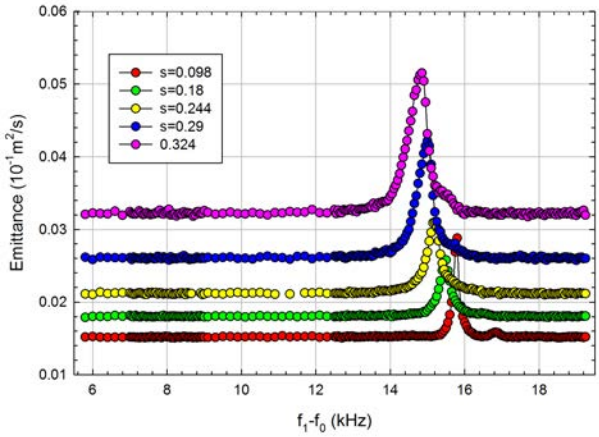

(c) Emittance vs $f_1 - f_0$

Figure 4.6: The properties of charge bunches changed significantly when strong resonance between collective modes and perturbation occurred.

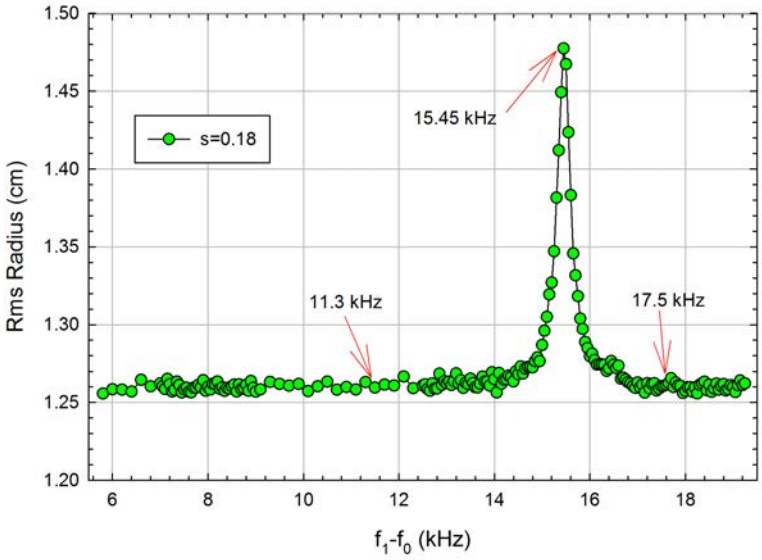

(a) Rms radius vs perturbation frequency at $\hat{s} = 0.18$

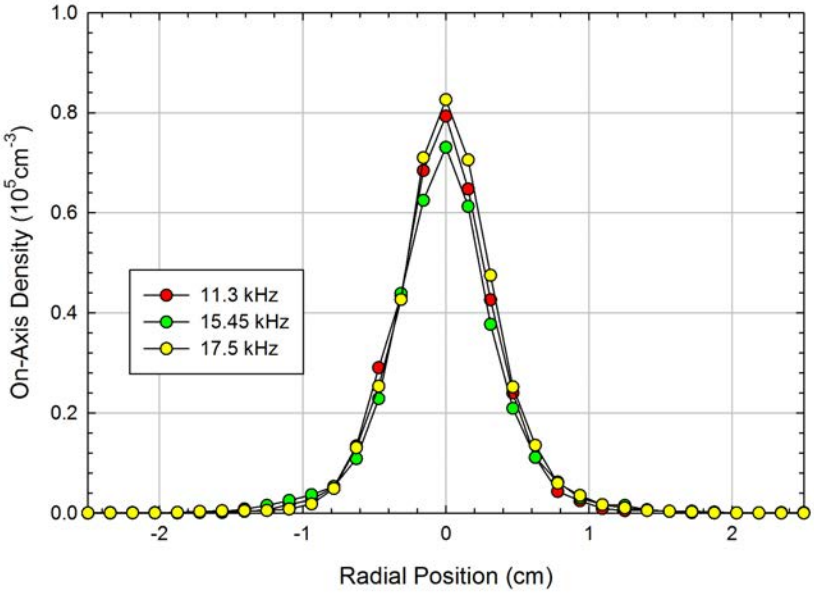

(b) Radial density profiles at selected perturbation frequencies

Figure 4.7: The radial density profiles at different perturbation frequencies under initial $\hat{s}$ = 0.18. At resonance frequency, the radial density profile is lower than normal case and the charge bunch is broader.

excite the collective modes, leading us to choose f_1 to match the collective mode frequencies, i.e. $f_1 = f_{mode}$. Further, the amplitude of the perturbed voltage for the linear drive scheme is also smaller compared to that of the beat drive scheme. In our case, the typical perturbed

voltage amplitude is 0.12% of V_0. When the external perturbation frequency is the same as the collective mode frequency, strong resonance may occur between the external perturbation and the collective modes. The resonance serves an extra energy source and heats the plasma. As the plasma is expanding radially due to the heating, the on-axis charge density will decrease which can be easily observed in experiments. For a strong resonance to occur, not only does the perturbation frequency have to match a collective mode frequency, but also the spatial structure of the perturbation has to match that of a collective mode. The theoretical model of collective modes described in Sec. 4.2 predicts that the collective mode frequency is a decreasing function of normalized intensity $\hat{s}$. The experimental results are shown in Fig. 4.8 for the case of a quadrupole perturbation. As expected, since the spatial structure of the perturbation matched the quadrupole mode, the charge bunch responds strongly near $2f_q$, the expected quadrupole mode frequency, while there is little response near f_q, the expected dipole mode frequency. This feature is clearly demonstrated by Fig. 4.8(b) and Fig. 4.8(c). Note that there are two conspicuous peaks near the quadrupole mode frequency and this is likely due to coupling to other modes that have frequencies near $2f_q$. For example, the quadrupole mode and the breathing mode both have frequencies near $2f_q$.

The normalized intensity dependence of the quadrupole mode frequency shown in Fig. 4.8 was measured by repeating the experiment for various amounts of injected charge. There are two primary peaks which shift as the $\hat{s}$ varies. The frequencies of the primary peaks in data such as those in Fig. 4.8 are plotted as a function of normalized intensity $\hat{s}$ in Fig. 4.9. Both the linear regression and the quadratic regression of the breathing mode data agree well with the experimental data but exhibit noticeable discrepancy at small normalized intensity $\hat{s}$. There are a couple of possible reasons to explain that discrepancy. First of all, only four data points were used in the regression, which made the regression inevitably subject to relatively large regression error due to small sample size. Another possible reason relates to the difficulty of properly identifying the breathing mode. Since the spatial structure of the external perturbation is more favorable to exciting the quadrupole

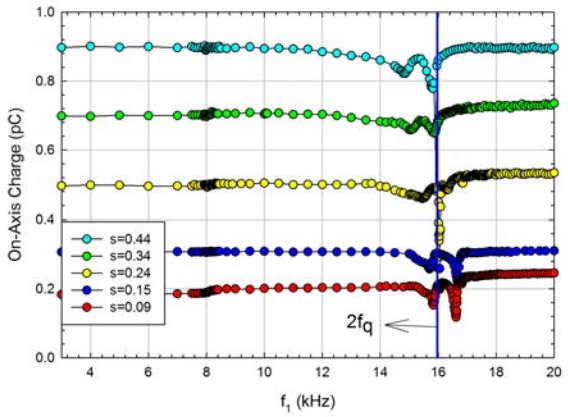

(a) On-axis charge density vs perturbation frequency in the whole frequency range

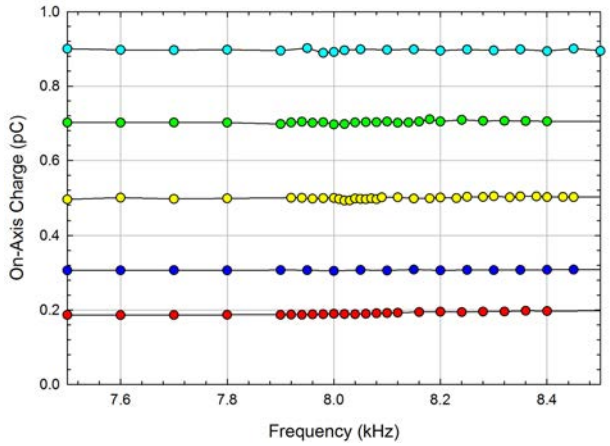

(b) On-axis charge density vs perturbation frequency between 7.5 kHz and 8.5 kHz

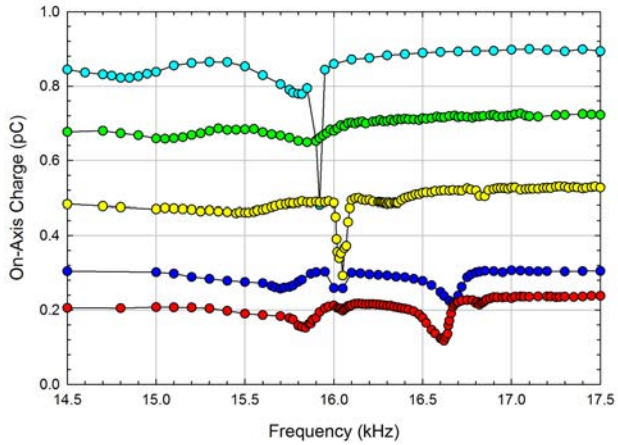

(c) On-axis charge density vs perturbation frequency between 14.5 kHz and 17.5 kHz

Figure 4.8: On-axis charge density as a function of perturbation frequency at different normalized intensity $\hat{s}$.

mode, it is difficult to determine if the breathing mode has been excited. Taking into account the possibility of mode coupling near $2f_q$, it is even harder to identify the breathing mode. Both the linear regression and the quadratic regressions of the quadrupole mode data agree well with the experimental data and the polynomial regressions also agree well at small $\hat{s}$. To further compare the experimental data with the simple KV theoretical model, we plot the experimental data with the theoretical model together in Fig. 4.10. We choose the linear regression plots for both quadrupole and breathing modes for comparison purpose. The first terms of both regressions are extremely close to $2f_q$, which agrees with the simple KV smooth-focusing model at small normalized intensity $\hat{s}$. Experimental data shows weaker dependence of mode frequencies on $\hat{s}$ than the theoretical model and the dependence of the breathing mode is on $\hat{s}$ is much weaker than that of the quadrupole mode. Although the experimental data agree with the theoretical model qualitatively, the mode frequencies from the experiments are consistently higher than the theoretical values and it shows systematic difference between them. This difference may be explained both by the measurement errors of operating parameters and oversimplicity of the theoretical model. For example, for the linear regression of the quadrupole mode frequencies at various $\hat{s}$, the interception coefficient is about 16.125 kHz, which corresponds to the quadrupole mode frequency at zero $\hat{s}$ (i.e. $2w_q$). The corresponding $2w_q$ used in the theoretical model is about 15.9 kHz, which is about 1.5% smaller than 16.125 kHz. The w_q used in the theoretical mode is computed using the measured values oscillating voltage amplitude V_0, the oscillating voltage frequency f_0, the radius of the PTSX electrodes R. Take the measurement of the voltage amplitude for example, the fluctuation of the measurement is about 1.4%. All being said, the measurement error could be partially responsible for the discrepancy between the experiment and the theory. With regard to the concerned KV smooth-focusing model, the charge bunch number density $n(x, y, s)$ is uniform within the elliptical cross-section $x^2/a^2(s) + y^2/b^2(s) = 1$, while $n(x, y, s)$ is zero outside the elliptical cross-section [1]. In our case, the radial density profile in equilibrium is approximately Gaussian which is far cry from uniform. This oversimplicity

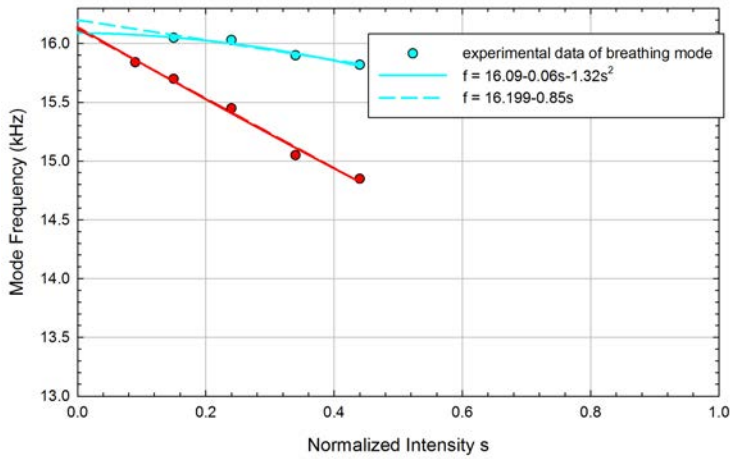

Figure 4.9: Comparison between experimental data and polynomial regressions for both quadrupole mode and breathing mode.

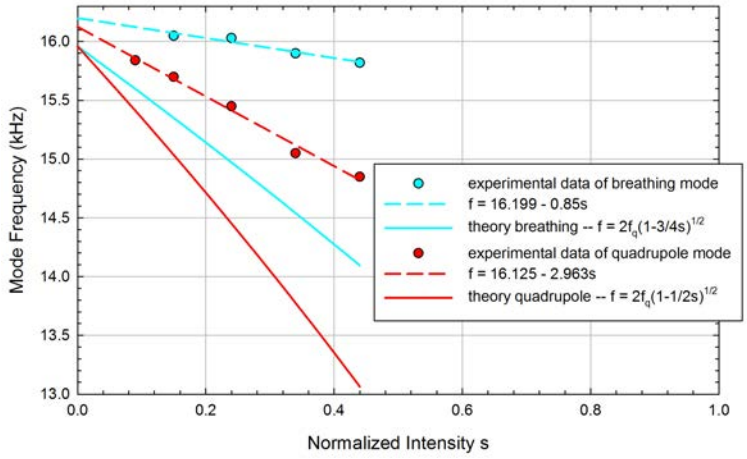

Figure 4.10: A simple KV smooth-focusing model predicts a decrease of quadrupole mode frequencies as a function of the normalized intensity $\hat{s}$. The experimental data exhibits weak dependence on $\hat{s}$

of the theoretical model is probably a major reason why the theoretical model doesn't fully explain the experimental results quantitatively.

The experimental results shown in Fig. 4.8, 4.9 and 4.10 were obtained by applying 0.12% perturbation on the PTSX electrodes. We saw strong response of the plasma near the $2f_q$ frequency, and didn't see rich mode structures at other frequencies. In that case, the primary modes are still relatively easy to identify. As we increased the amplitude of

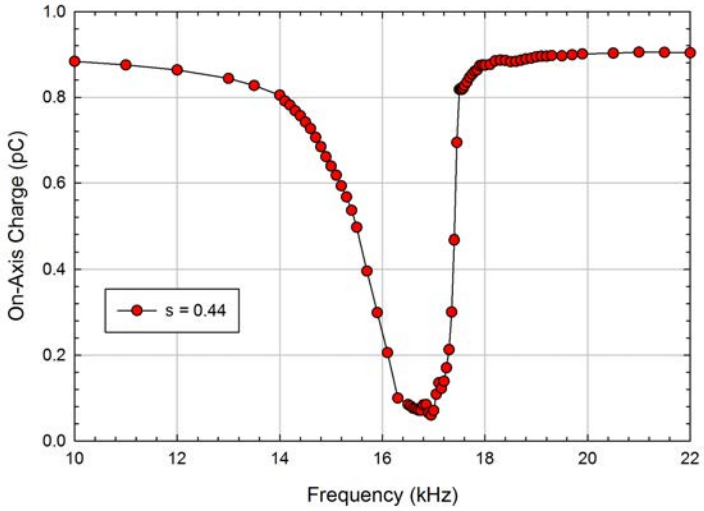

Figure 4.11: On-axis charge density as a function of the perturbation frequency. The perturbation amplitude is 0.5% and the unperturbed normalized intensity $\hat{s}$ is 0.44.

the perturbation, it is highly possible that the collective modes were driven to the nonlinear regime and the mode coupling became more complicated. As we see from Fig. 4.11, at 0.5% perturbation amplitude, the possible nonlinear behavior and the complex coupling of collective modes results in a huge drop of the on-axis density near $2f_q$ and it is difficult to tell which specific modes have been excited. It is still unclear why this behavior occurs and it is hard to draw meaningful conclusions without further investigation of this behavior in the future research.

Warp Simulation Results

In Sec. 4.3.2, we applied a sum of sine waves on PTSX electrodes to study the excitation of quadrupole mode. Figure 4.8 shows the charge bunch has a strong response near $2f_q$, the expected quadrupole mode frequency, while there is little response at other perturbation frequencies. Figure 4.10 compares the dependence of mode frequencies on $\hat{s}$ from experiments with the simple KV smooth-focusing model predicts. Although the KV model qualitatively agrees with the experimental results, some assumptions of the KV model don't apply to our experimental circumstances which probably can explain the quantitative discrepancies

between the KV model and the experimental results. To better understand the excitation of quadrupole modes in PTSX, we employed the 3D Warp simulation tool. In the 3D Warp simulation, we used 0.12% perturbation amplitude all through and scan the perturbation frequency under different initial normalized intensity $\hat{s}$. The charge bunch was injected into the PTSX main chamber and was allowed 5 ms to relaxed to a steady state before the external perturbation kicked in. After 30 ms of perturbation, the charge bunch was given 15 ms to relax to another equilibrium state. We measured complete radial charge density profile, from which we computed other important quantities such as rms radius, transverse temperature, and emittance.

Figure 4.12 shows the on-axis number density as a function of perturbation frequency under different initial $\hat{s}$. As shown in the experimental data, the simulation data also shows strong response near $2f_q$ and the mode structures shown in the simulation are quite similar to what we saw in the experiments. It is unclear why some mode structures have only conspicuous mode instead of two like we saw above in the experiments (Fig. 4.8). Based on the spatial structure of the perturbation, the quadrupole mode the most likely mode to be excited, so we treat only conspicuous mode in some mode structures as the quadrupole mode. Not only did the simulation confirm the existence of the quadrupole mode, it also provided a tool to study the dependence of quadrupole mode frequency on $\hat{s}$. Figure 4.13 shows the comparison of dependence of quadrupole mode on $\hat{s}$ between experiment, simulation and KV smooth-focusing model. The simulation and the experiment agreed pretty well with each other, while both of them differed from the KV model quantitatively.

Besides studying the dependence of mode frequencies on $\hat{s}$, we can also use a 3D Warp simulation to study the properties of charge bunch such as rms radius, transverse temperature, emittance under external perturbation. Fig. 4.14 shows the changes of rms radius, transverse temperature and emittance as perturbation frequency changed. At the mode frequency, strong resonance occurred and the charge bunch was heated by the extra energy which also led to the expansion of the charge bunch. Both the transverse temperature and

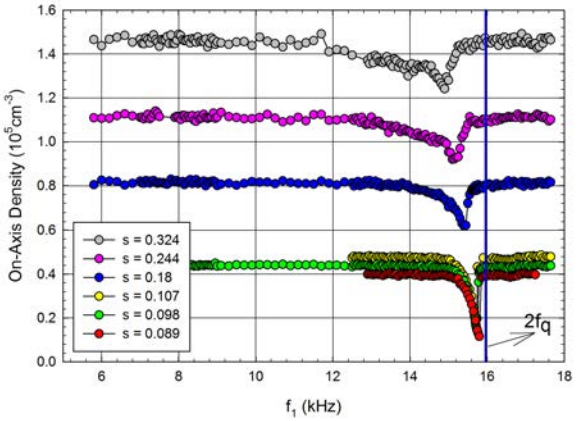

(a) On-axis number density vs perturbation frequency in the whole frequency range

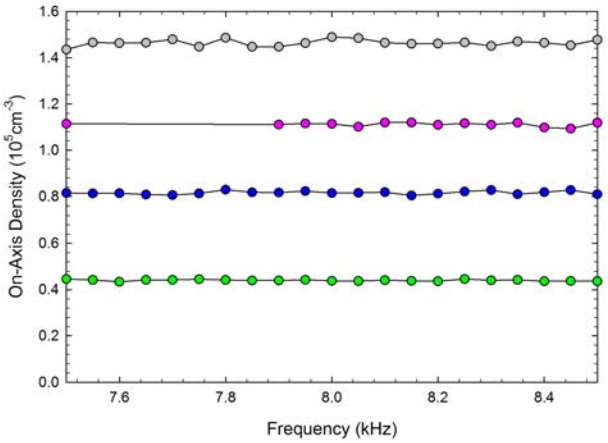

(b) On-axis number density vs perturbation frequency between 7.5 kHz and 8.5 kHz

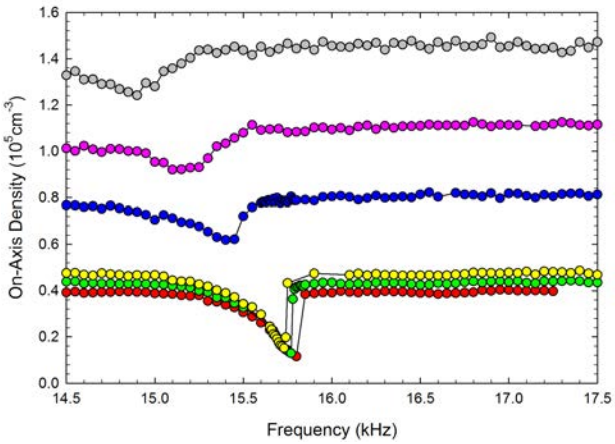

(c) On-axis number density vs perturbation frequency between 14.5 kHz and 17.5 kHz

Figure 4.12: On-axis number density as a function of perturbation frequency under different $\hat{s}$. Different initial $\hat{s}$ are chosen to study the mode frequency dependence on $\hat{s}$. The charge bunch shows strong response to the perturbation near $2f_q$, while having little response at other frequencies.

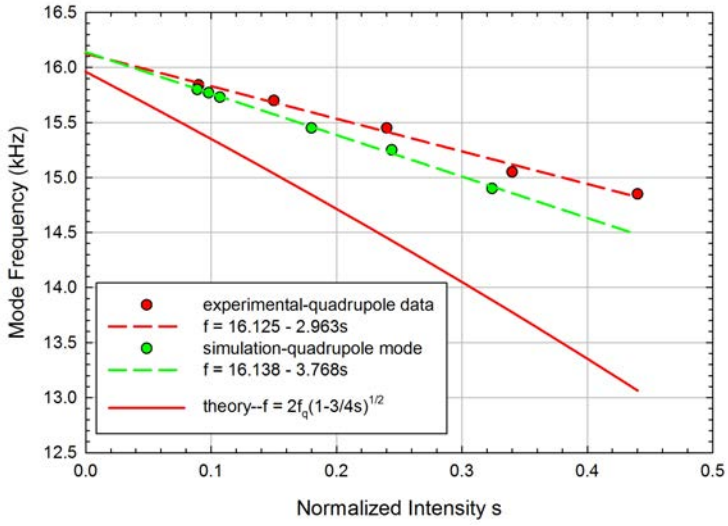

Figure 4.13: Comparison of dependence of quadrupole mode frequency on $\hat{s}$ between experiment, simulation and KV smooth-focusing model. The experiment and simulation results agree pretty well with each other, while both of them differs from the KV smooth-focusing model quantitatively.

the rms radius increased accordingly. If the particles stray too far away from the center, they eventually lose confinement. So usually when the resonance occurs, particles are lost. The resonance intensity decreased as the perturbation frequency moved away from the mode frequency which resulted in the quasi bell shape of the radial density profiles. To further describe the expansion of charge bunch during resonance, we plotted the radial density profiles of the charge bunch at different perturbation frequencies and compared them head-to-head. Fig. 4.15 shows the radial density profiles at different perturbation frequencies with initial $\hat{s} = 0.18$. As the resonance occurred, the charge bunch expanded and the on-axis density dropped according. Since the resonance between the external perturbation and the collective modes of the charge bunch causes the beam degradation, we should try our best to avoid the resonance as best as we can. It is still unclear how exactly the external perturbation interacts with the collective modes of the charge bunch. This will be further studied in the future research.

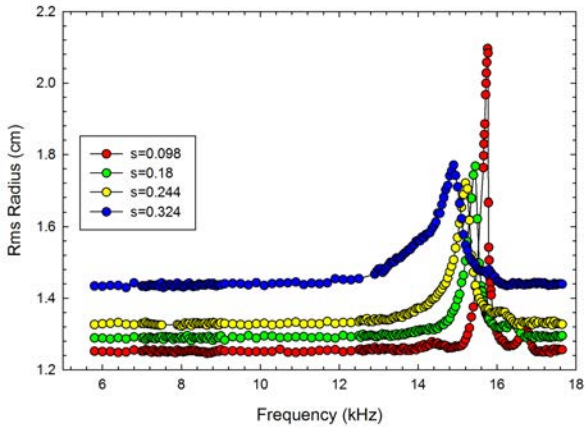

(a) Rms radius vs perturbation frequency

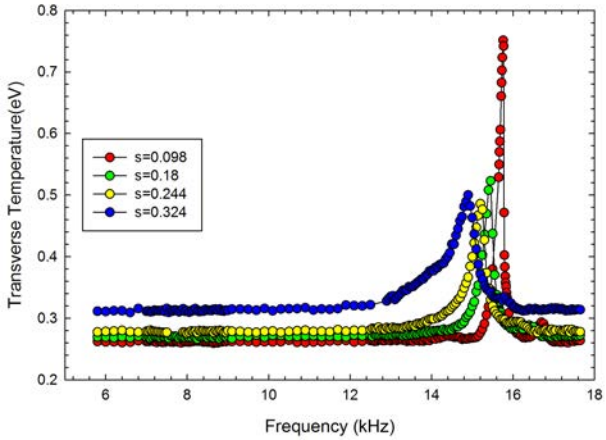

(b) Transverse temperature vs perturbation frequency

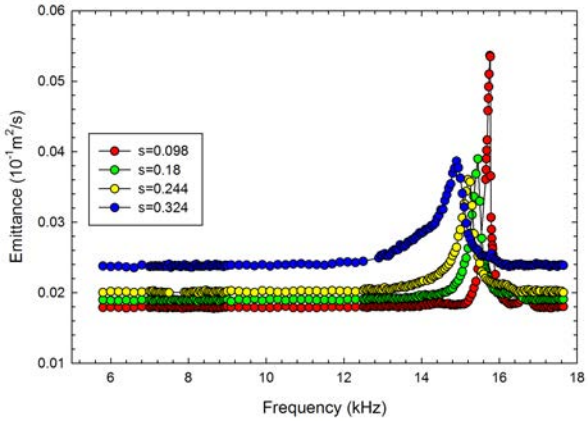

(c) Emittance vs perturbation frequency

Figure 4.14: The properties of charge bunch changed significantly when strong resonance between collective modes and perturbation occurred.

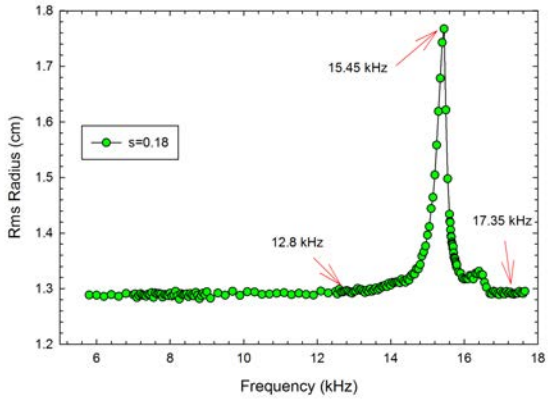

(a) Rms radius vs perturbation frequency at $\hat{s} = 0.18$

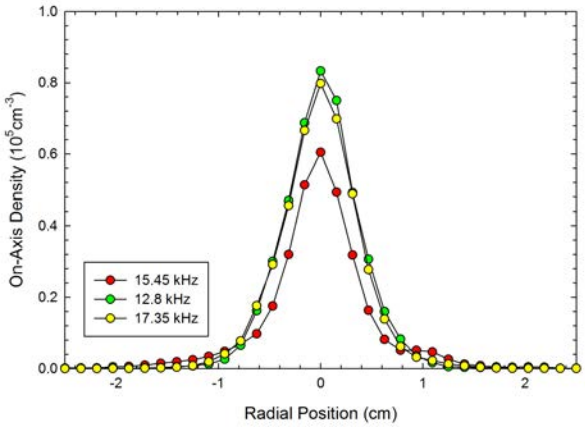

(b) Radial density profiles at selected perturbation frequencies

Figure 4.15: The radial density profiles at different perturbation frequencies under initial $\hat{s}$ = 0.18. At resonance frequency, the radial density profile is lower than normal case and the charge bunch is broader.

4.4 Excitation of Dipole Modes

4.4.1 Experimental Results

In Sec. 4.3, we discussed the excitation of the quadrupole mode using a beat drive and a linear drive scheme. We also presented the effects of external perturbations on beam characteristics. In this section, we will focus on another important collective mode: the dipole mode. In order to excite the dipole mode, the spatial structure and the frequency of the the perturbation should be the same of those of the dipole mode. While the frequency

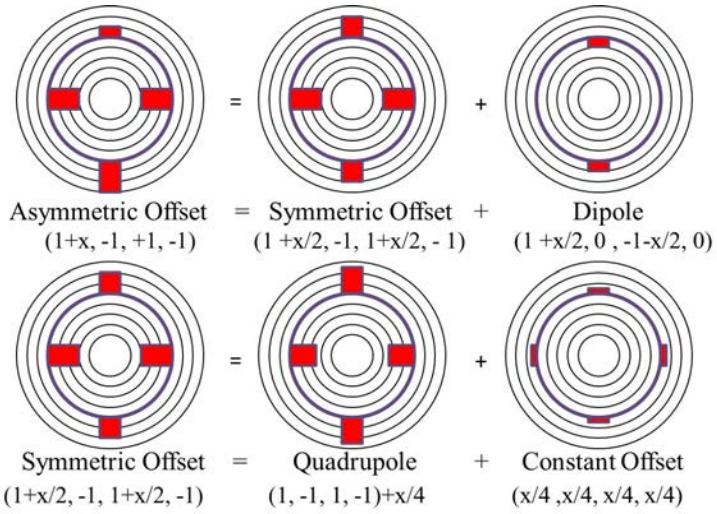

Figure 4.16: Decomposition of the set of voltages { +(1+x), -1, +1, -1}as a combination of perturbed quadrupole field, a dipole field, and a uniform perturbation.

can be easily controlled by the arbitrary function generators, the spatial structure of the perturbation is controlled by applying a slightly different waveform on one of the PTSX electrodes. As described in Sec. 3.2, the oscillating quadrupole field is produced by the four PTSX electrodes when the four electrodes have voltages $\{+V_0, -V_0, +V_0, -V_0\}$ $\sin(2\pi ft)$ applied to them, and the potential inside the PTSX chamber can be written as [15]

$$V(r,\theta,t) = \frac{4V_0(t)}{\pi}\sum_{l=1}^{\infty}\frac{\sin(l\pi/2)}{l}\left(\frac{r}{r_w}\right)^{2l}\cos(2l\theta) \tag{4.6}$$

For the general case, where the four PTSX electrodes have voltages $\{V_1, V_2, V_3, V_4\}$ applied to them, and the potential inside the cylinder has the form $V(r,\theta) = \sum_{l=0}^{\infty} C_l (r/r_w)^l \cos(l\theta)$, the normalized amplitude of each multipole component can be written as $A_l = \frac{1}{4}\int_0^{2\pi} V(r_w,\theta)\cos(l\theta)$. We choose the normalization so that a set of voltages {+1, -1, +1, -1} produces a quadrupole term with strength $A_2 = 1$. Accordingly, this set of voltages {+1, -1, +1, -1} generates a quadrupole term $A_2 = 1$, a 12-pole term $A_6 = 1/3$, and higher-order terms.

A simple way to create a dipole perturbation while still well preserving the normal quadrupole field is to apply a set of voltages $\{+(1+\delta), -1, +1, -1\}$ to the four PTSX electrodes [12]. Since the potential is additive, the above set of voltages can be de-

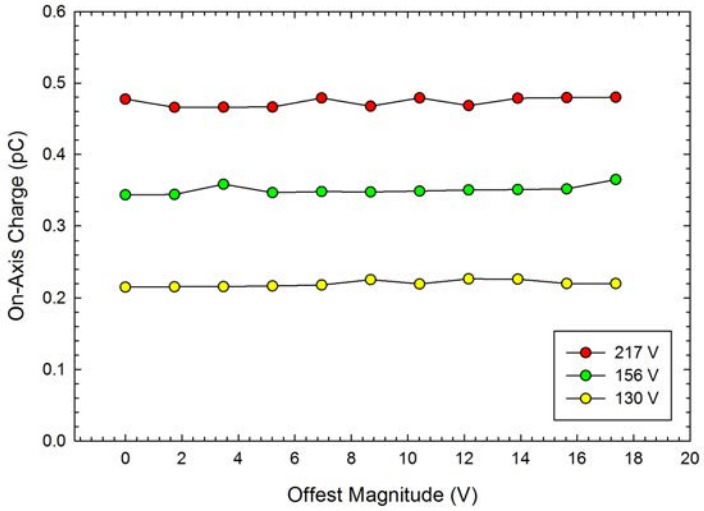

Figure 4.17: Uniform perturbations are applied to the plasma under different oscillating voltage amplitudes ranging from 130 V to 217 V. The on-axis charge density is almost constant and doesn't independent on the uniform perturbation amplitude. It suggests the uniform perturbation doesn't have any effect on the plasma.

composed as $\{+(1+\delta), -1, +1, -1\} = (1+\delta/4)\{+1, -1, +1, -1\} + \delta/2\{+1, 0, -1, 0\} + \delta/4\{+1, +1, +1, +1\}$, that is, as the sum of a perturbed quadrupole perturbation plus a dipole perturbation, and a uniform perturbation as shown in Fig. 4.16. In this case, $A_0 = \delta\pi/8, A_1 = \delta/4, A_2 = 1+\delta/4, A_3 = \delta/12, A_5 = \delta/20, A_6 = 1/3+\delta/12$, etc. The effects of hexapole and higher order terms can be safely neglected since the trapped charge bunch is confined near the center of the cylinder where $r/r_w < 0.25$. The $\delta/4$ increase in the quadrupole field can be compensated for by lowering the voltage amplitude on all four electrodes by $\delta/4$ if desired. Note that the A_0 term, corresponding to a uniform potential perturbation applied to the PTSX electrodes, does not contribute to the electric field force felt by the trapped charge bunch. Experiments were carried out in which uniform potential perturbations were applied to the PTSX electrodes, and no effect on the plasma was observed as seen in Fig. 4.17 [12]. Uniform perturbation with various amplitudes were applied to the PTSX electrodes. No matter what the main quadrupole voltage magnitude was, the uniform perturbation didn't have any effect on the plasma.

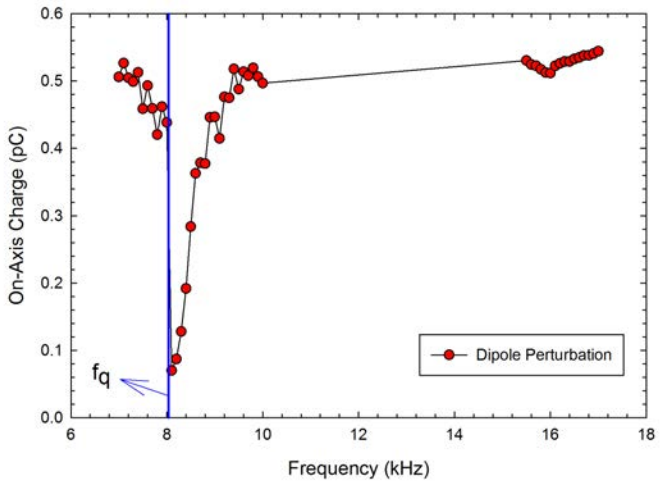

Figure 4.18: The plasma has a strong response to the external perturbation at dipole mode frequency f_q, while there is little response at other perturbation frequencies. The small response near $2f_q$ is probably due to the excitation of quadrupole mode.

In order to see the response of plasma to dipole perturbations with different frequencies, we scanned the perturbation frequency. Since the collective modes of interest are near either f_q or $2f_q$, where the f_q is the smooth-focusing frequency, the perturbation frequency was scanned within vicinity of those frequencies. The dipole perturbation amplitude is 0.5% of the main quadrupole voltage amplitude. The on-axis charge was measured after the perturbation was turned off and plotted as a function of perturbation frequency. As shown in Fig. 4.18, the dipole perturbation had a strong resonance with the dipole mode of the charge bunch, while having little effect on the charge bunch at other frequencies. It is noted that there is a local minimum on Fig. 4.18 near $2f_q$. It is likely to be the quadrupole mode. The mode amplitude is very small mainly because the spatial structure of the perturbation is not favorable to the excitation of the quadrupole mode.

In order to study the beam qualities under different perturbation amplitudes, we fixed the perturbation frequency at the dipole mode frequency to make sure that the dipole mode would be excited. Then various perturbation amplitudes were applied to one PTSX electrode. The radial density profiles were measured at each perturbation amplitude. The rms radius

R_b and line charge density N were computed from the complete radial density profile. Using the following global force balance equation [1],

$$m\omega_q^2 R_b^2 = 2kT + \frac{Nq^2}{4\pi\epsilon_0}, \tag{4.7}$$

the transverse temperature kT was computed. The emittance was calculated as $2\sqrt{2}R_b\sqrt{kT}$. As expected, when the resonance between the external perturbation and the dipole mode occurred, the plasma was heated by the extra energy, causing the beam's temperature to rise and the beam to expand, eventually causing the emittance growth. As the perturbation amplitude increased, the damaging effect was more conspicuous as shown in Fig. 4.19. It is demonstrated that even a small amplitude dipole perturbation can cause a strong response from the plasma. In Fig. 4.19 (d), we can see that even a 10 ms dipole perturbation of 0.7% amplitude can cause a more than 20% increase of the emittance. Since the plasma is quite sensitive to the dipole perturbation, we should try our best to avoid the dipole perturbation.

To study the dependence of the dipole mode on the space charge, we varied the bias voltage on the emitting surface of the cesium ion source to obtain a range of charge densities. Since the dipole mode corresponds to the movement of the whole plasma column, its frequency should be independent of the space charge. As demonstrated in Fig. 4.20, the dipole mode frequency remained the same for various charge densities.

Finally, as discussed before, the way we applied the dipole perturbation introduced an extra minor quadrupole perturbation. To verify that the damaging effect at dipole mode frequency was caused by the perturbation of dipole spatial structure instead of the perturbation of quadrupole spatial structure. We separated the two perturbations and studied their effects separately. This will be discussed in Sec. 4.5.

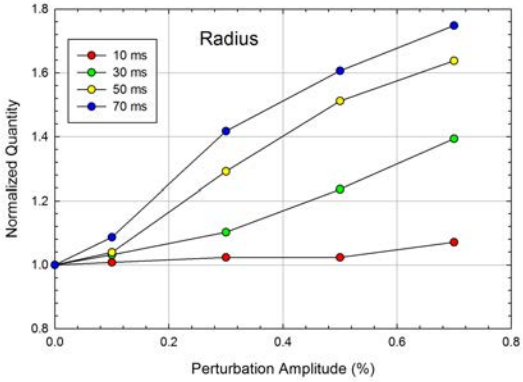

(a) The rms radius vs perturbation amplitude

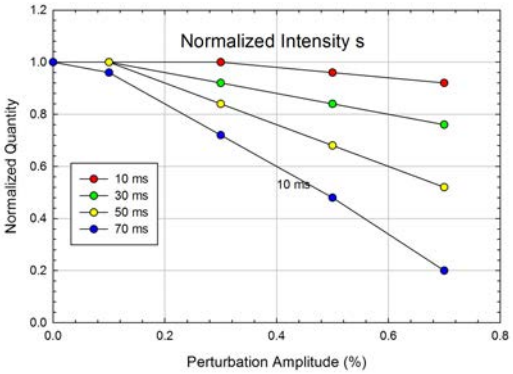

(b) Normalized intensity vs perturbation amplitude

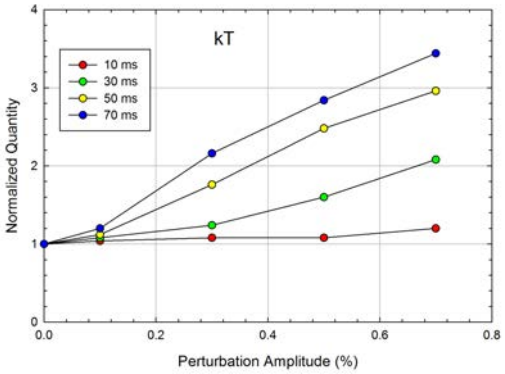

(c) Transverse temperature vs perturbation amplitude

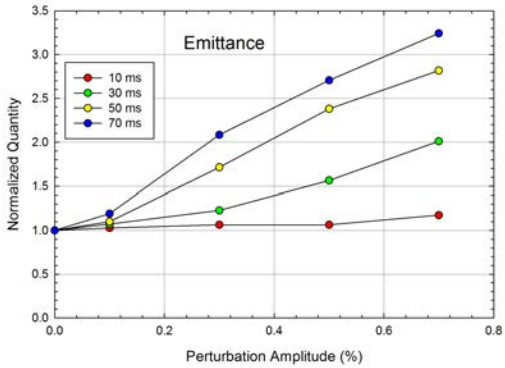

(d) Emittance vs perturbation amplitude

Figure 4.19: As the perturbation time and the perturbation amplitude increase, the dipole perturbation has increasingly damaging effect on the charge bunch.

4.4.2 Warp Simulation Results

In the previous section, we have shown the experimental results using an external dipole perturbation. As expected, the plasma had a strong response at the dipole mode frequency and the plasma expanded due to the extra heating from the resonance, causing the decrease of on-axis density and the broadening of the radial density profile. As the perturbation duration and amplitude increased, the damaging effects became more conspicuous. We also showed that the dipole mode frequency is independent on the space charge, which agrees with the

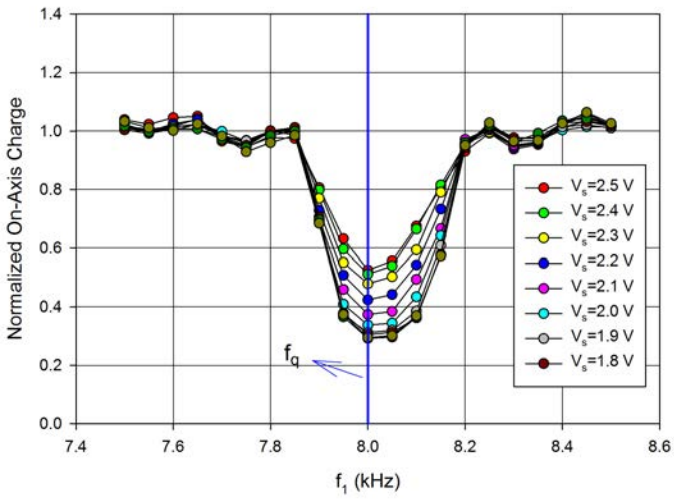

Figure 4.20: The dipole perturbation is applied to the plasma under different bias voltage V_s on the cesium ion source ranging from 1.6 V to 2.5 V. V_s determines the injected charge density which determines the space charge field strength. The measured on-axis density is normalized with respect to the unperturbed value for each V_s. The plots clearly show that the dipole mode is independent on the space charge.

theory. To further interpret the experimental results, we used the 3D Warp simulation results for the comparison with the experimental data. In the experiments, the dipole perturbation was applied by adding perturbation on one PTSX electrode, which also introduced smaller amplitude quadrupole perturbation and a uniform perturbation. In the 3D Warp simulation, we use the same technique to simulate what happens in the experiments. The 3D Warp is a particle-in-cell (PIC) simulation code. The simulation is set up in the following manner: The number of the macro particles as 80,000, the transverse grid size as 10/32 cm. The time step is 1/20 of the lattice period, where the lattice period in our case is 16.67 μ s. The dipole perturbation duration is chosen to be 30 ms which is the same as in the experiments. The perturbation amplitudes and the initial normalized intensity $\hat{s}$ are varied to simulate various scenarios in the experiments. The total simulation duration is 50 ms. In the first 5 ms, the plasma is allowed to relax to an equilibrium state. Afterwards, the 30 ms perturbation kicks in. Then the plasma is given another 15 ms to relax to a new equilibrium. The radial density profiles are measured in the end of the simulations. The corresponding quantities

including the rms radius, the transverse temperature, the emittance, the line-charge density are computed from the radial density profiles using the global force balance equation [1].

Figure 4.21 shows the changes of the beam density, rms radius and temperature as a function of the perturbation frequency at 0.1% perturbation amplitude. As expected, the plasma shows a strong response to the external perturbation at the dipole mode frequency. The plasma was heated by the extra energy from the resonance which caused the expansion of the plasma and the decrease of on-axis density. To further investigate the transverse particle distribution of the plasma at different perturbation frequencies, we plotted the radial density profiles of the plasma perturbed at the dipole mode frequency and at frequencies far away from the dipole mode frequency. Figure 4.22 (a) shows the radial density profiles of the plasma after being perturbed at the dipole mode frequency and at other frequencies. It shows when the plasma is perturbed at frequencies far from the dipole mode frequency, the plasma is barely affected and the shape of the profile is quite Gaussian. However, while the plasma is perturbed at dipole frequency, the strong resonance between the plasma and the external perturbation causes the plasma to expand significantly, rendering a broad, non-Gaussian density profile. The rms radius of the perturbed plasma at the dipole mode frequency is almost twice that of the perturbed plasma at other frequencies. To further investigate the two-dimensional distribution of the particles during the external perturbation, we plotted the transverse particle distributions before and after the dipole perturbations. Figure 4.22 (b) is the transverse particle distribution some time before the perturbation. If we look at the particle distribution for a few lattice periods, we will see the particle bunch is oscillating at lattice frequency in both transverse directions and the average shape looks like an eclipse. If there is no external perturbation, the particle bunch will remain in equilibrium and the line-charge density will be conserved. Figure 4.22 (c) shows the particle distribution after 5 ms perturbation. The shape of the distribution is really strange and the origin of the shape is unclear. To further investigate the incremental changes of the particle distribution, we plotted the incremental changes of the particle distribution after 5 ms perturbation with

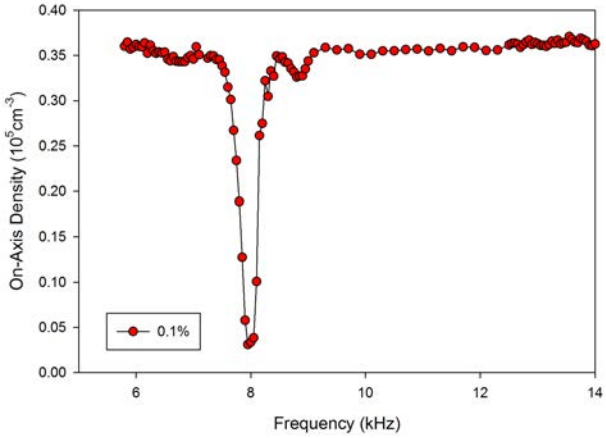

(a) On-axis density vs perturbation frequency

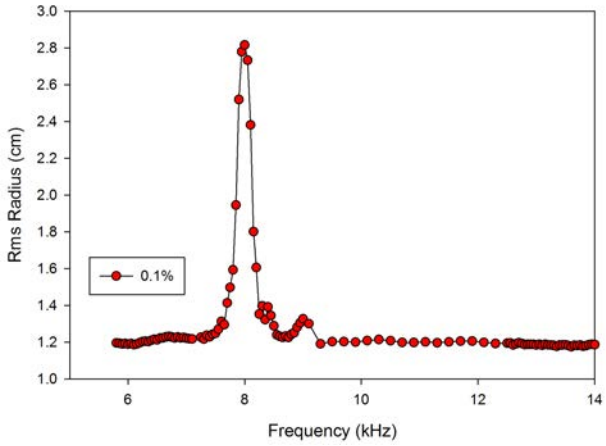

(b) Rms radius vs perturbation frequency

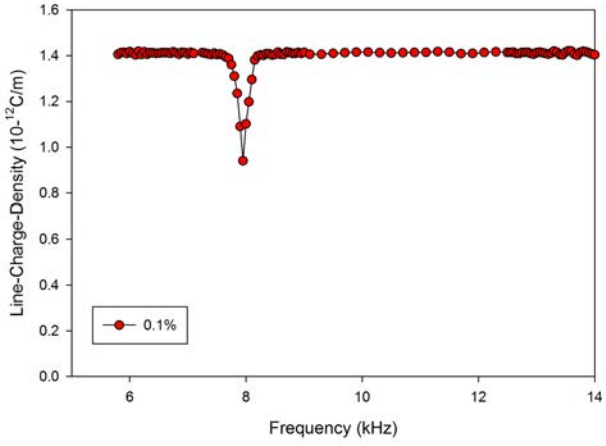

(c) Line-charge density vs perturbation frequency

Figure 4.21: There is a strong response at the dipole mode frequency when 0.1% external perturbation with dipole structure is applied. For other frequencies, there is little response from the plasma.

an interval of 15 time steps. Figure 4.23 and Fig. 4.24 show the continuous change of the particle distribution. Although it is still unclear why those specific shape of distribution came up, it is clear that the whole charge bunch is oscillating in the X direction with a period of approximately 150 time steps. In our experiments, the lattice frequency is 60 kHz and the time step is 1/20 of the lattice period. So the oscillating frequency of the charge bunch in the X direction is approximately 60*20/150 = 8 kHz. This is exactly dipole mode frequency as calculated from the operating parameters. It is evident the the dipole mode has been excited and as time goes by, the strong resonance between the plasma and the external perturbation will cause the plasma to expand significantly.

So far, we have shown from the simulations that the perturbation at dipole mode frequency caused an expansion of the plasma and a decrease of the on-axis density. To further study to what extent the perturbation affects the plasma, we perturbed the plasma in the simulations at different amplitudes ranging from 0.05% to 0.35% and examine the changes of the on-axis density and line-charge density at different perturbation amplitudes. Figure 4.25 (a) shows the on-axis density as a function of the perturbation amplitude. It is expected that as the perturbation amplitude increases, the stronger resonance causes the plasma to expand to a larger extent and results in a bigger drop of the on-axis density. Figure 4.25 (b) and (c) combined illustrate that when the perturbation amplitude is small, the expansion of the plasma is small enough to conserve most of the charged particles. As the perturbation amplitude grows, some particles are driven too far away from the axis and eventually lose confinement. In terms of applying our findings in the dipole mode excitation to the design of the next-generation high-intensity accelerators, we should strive to avoid this kind of large amplitude perturbation at dipole mode frequency.

Finally, we used the 3D Warp simulation to study the dependence of the dipole mode frequency on the space charge effect by varying the normalized intensity parameter $\hat{s}$. Figure 4.26 shows that the dipole mode frequency is completely independent on the normalized

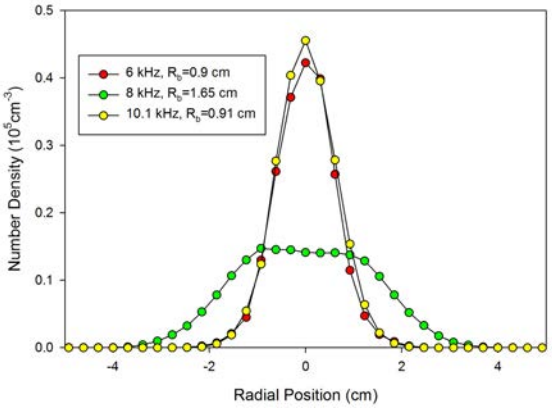

(a) Radial density profiles at various perturbation frequencies

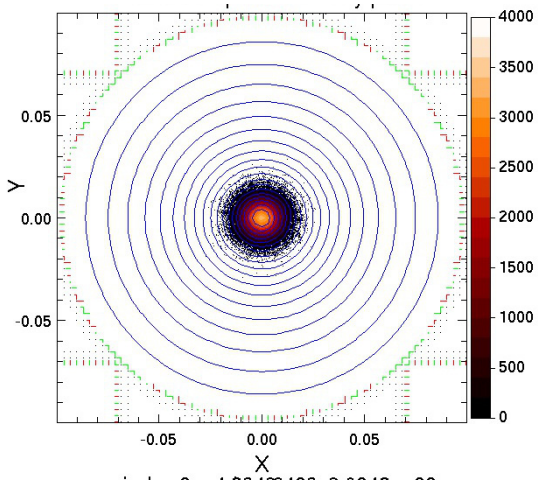

(b) Particle distribution of the plasma before external perturbation at dipole mode frequency

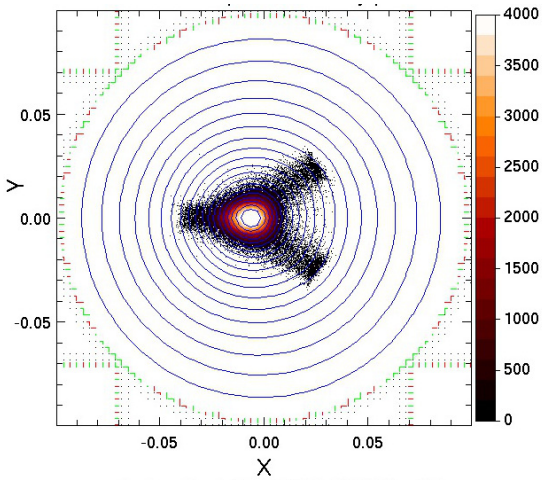

(c) Particle distribution of the plasma after 5 ms external perturbation at dipole mode frequency

Figure 4.22: The radial density profile after perturbation at the dipole mode frequency is much broader than those perturbed at other frequencies.

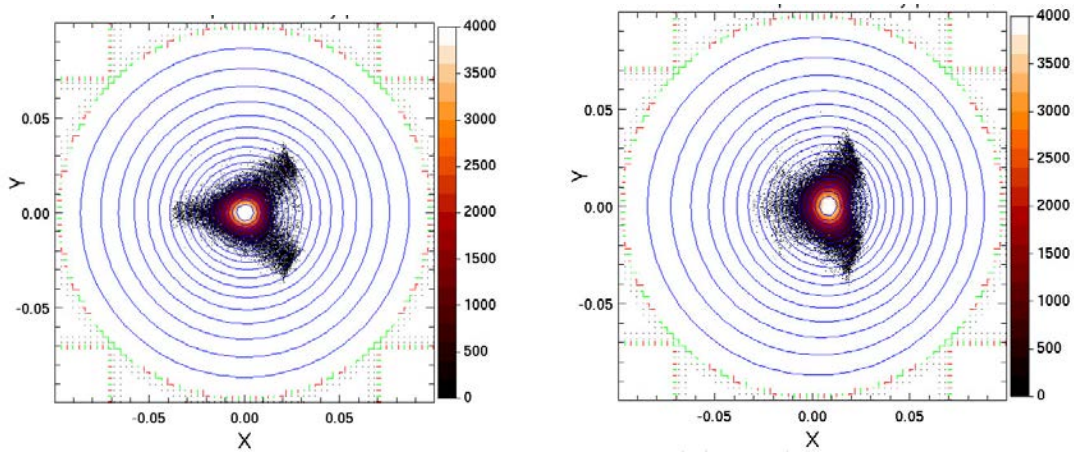

(a) Initial particle distribution

(b) Particle distribution after 15 steps

(c) Particle distribution after 30 steps

(d) Particle distribution after 45 steps

(e) Particle distribution after 60 steps

(f) Particle distribution after 75 steps

Figure 4.23: Particle distributions after 5 ms dipole perturbation. The consecutive particle distributions with incremental 15 time steps are shown above.

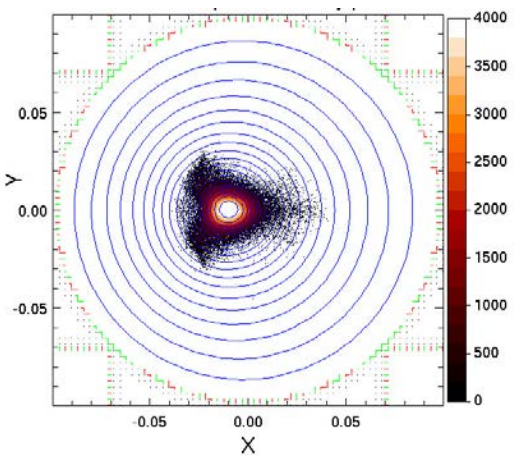

(a) Particle distribution after 90 steps

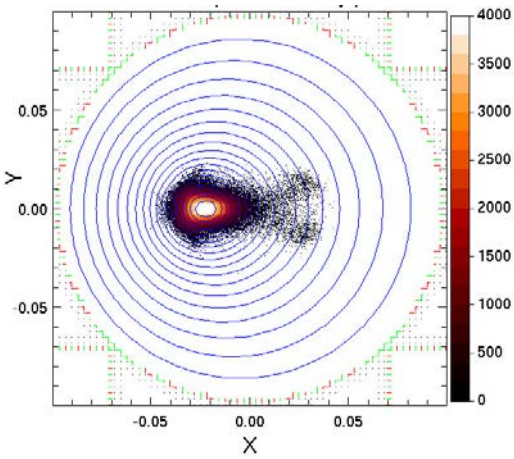

(b) Particle distribution after 105 steps

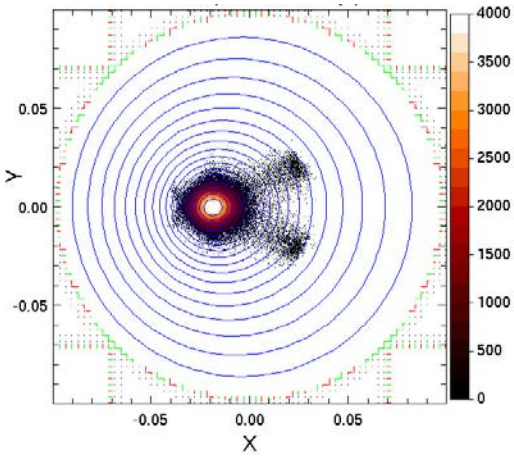

(c) Particle distribution after 120 steps

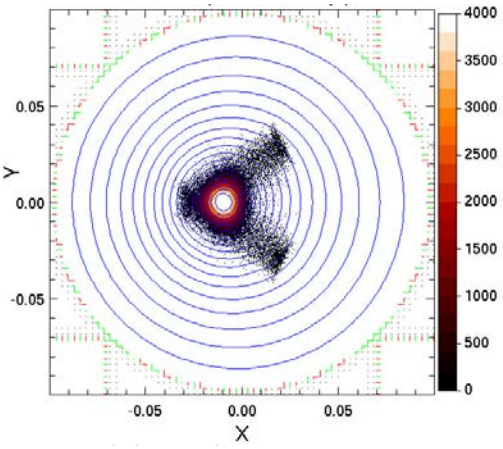

(d) Particle distribution after 135 steps

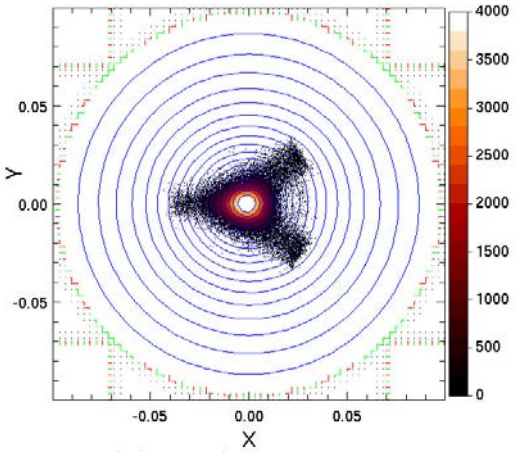

(e) Particle distribution after 150 steps

Figure 4.24: Particle distributions after 5 ms dipole perturbation. This continues the Fig. 4.23. The particle distribution is oscillating in the X direction with a period of about 150 time steps.

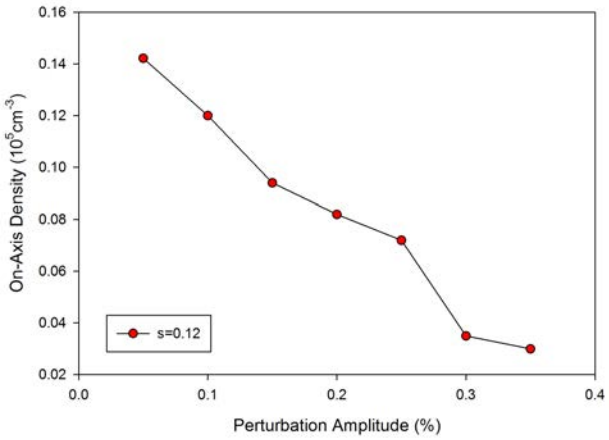

(a) On-axis density driven at dipole mode frequency using various perturbation amplitudes

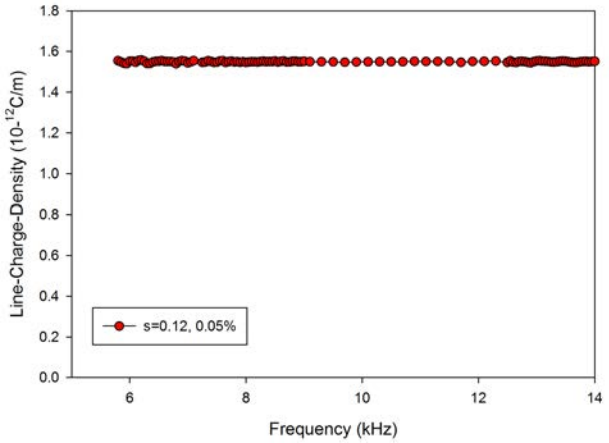

(b) Line-charge density for $\hat{s} = 0.12$ at different frequencies is conserved at small perturbation amplitudes

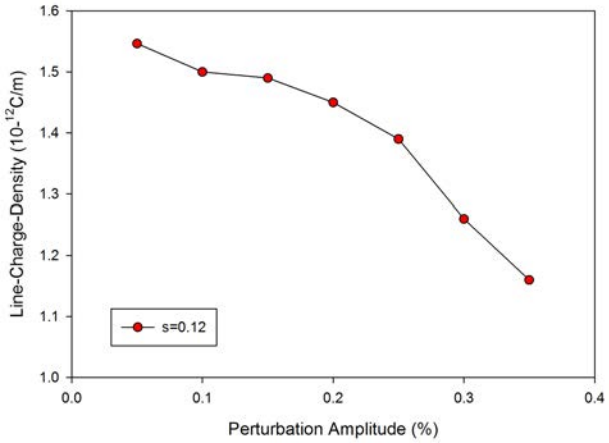

(c) Line-charge density driven at dipole mode frequency using various perturbation amplitudes

Figure 4.25: 3D Warp simulation shows that the effects of dipole perturbation increases as the amplitude grows. Large amplitude perturbation can cause particle loss.

intensity parameter $\hat{s}$. It is consistent with the theory prediction and the experimental results.

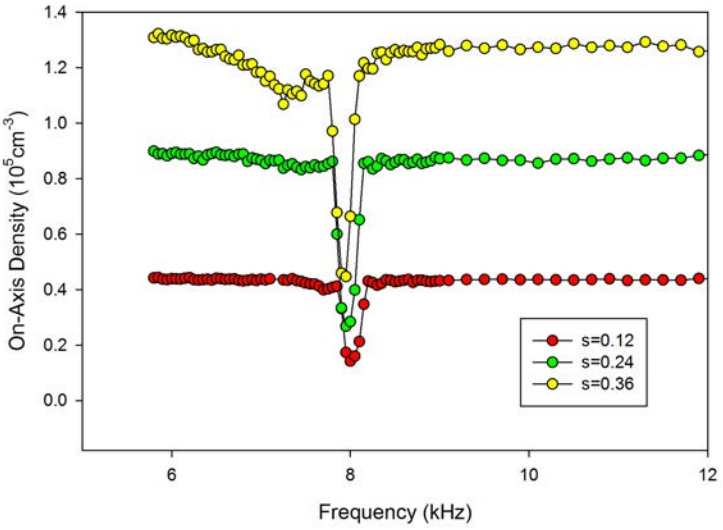

Figure 4.26: The dipole mode frequency is independent on the self field.

4.5 Machine Imperfection Effects

4.5.1 Coherent Periodic Resonances

Charged particles can circulate in a ring machine many times and, if there is a lattice perturbation inside a ring, the particles will experience that perturbation in a coherent periodic way. Assuming the frequency of this perturbation is f_{ring} and there exists a characteristic mode frequency f_q for the charge bunch traveling around the ring, when the condition $f_q = \nu f_{ring}$ is satisfied, where ν is an integer, there would be adverse effects for the charge bunch due to the interaction of perturbation and the inherent collective modes of the charge bunch. The integer ν is a called the tune of the transport system. For dipole mode with frequency f_q, avoiding integer ν prevents the adverse effects of dipole mode interacting with the coherent lattice errors. For quadrupole mode with frequency $2f_q$, avoiding both half-

integer and whole-integer avoids the adverse effects of quadrupole mode interacting with the coherent lattice errors.

In the experiments conducted on PTSX, coherent periodic perturbation is applied by changing the waveform amplitude every N^{th} period by a fixed amount, corresponding to a N-lattice-period ring machine. The size of the perturbation every N^{th} period is usually expressed as a percentage of the regular waveform amplitude V_0. To study the interaction of the dipole mode with the perturbation, the perturbation is applied to a single PTSX electrode, while for the quadruple mode case, the perturbation is applied to all four PTSX electrodes. The tune ν can be changed either by varying the ring lattice period N or changing the waveform voltage amplitude, corresponding to changing f_{ring} and f_q, respectively. For both dipole and quadruple mode cases, we start the experiments by tuning the PTSX device to $\nu = 2$ for $N = 12$ given a lattice frequency of 60 kHz. This adjustment is made by varying the waveform voltage amplitude V_0 in the neighborhood of values corresponding to approximately $\nu = 2$. The desired tune is found by choosing the V_0 such that the measured on-axis charge of the trapped charge bunch decreases significantly. For dipole mode, the frequency is 10kHz, while for the quadrupole mode, the frequency is approximately 20 kHz when the normalized intensity $\hat{s}$ is small. The data in Fig. 4.27 shows that the adverse effects of the quadrupole perturbation are strong when the tune ν is an half-integer or whole integer value. Similar data have shown that the adverse effect is strong when the tune ν is a whole-integer value.

In the above experiments, the tune is changed by varying the ring period. Alternatively, the tune can be changed by changing the mode frequency. Experiments were conducted for both quadrupole and dipole perturbations where the periodicity of the ring is fixed at $N = 12$, while varying the waveform voltage amplitude from 0 V to 350 V. Without resonant effects between collective modes and external perturbation, the on-axis charge is expected to increase with V_0 when the transverse confining force is small. When V_0 becomes so large such that the vacuum phase advance σ_v exceeds 180 degrees, the transverse particle confinement

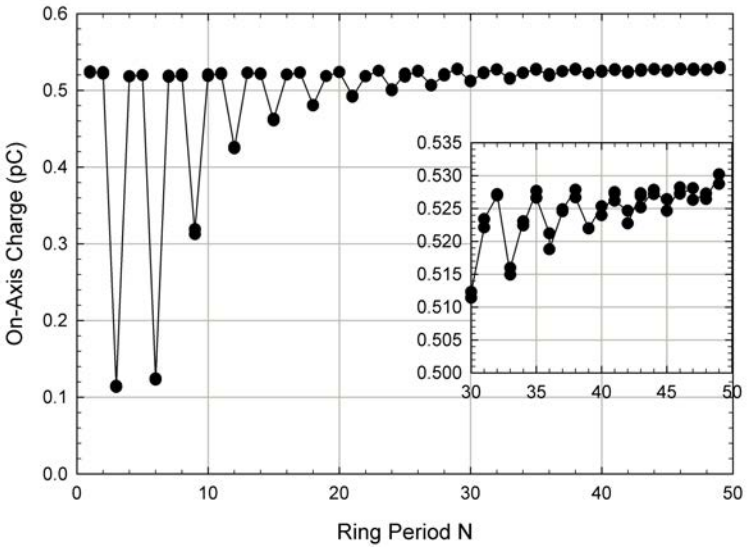

Figure 4.27: The quadrupole mode period is three lattice periods for a vacuum phase advance $\sigma_v = 60$. Whenever the ring period is a multiple of three, the quadrupole mode is strongly excited [12].

is lost and the on-axis charge drops significantly. Figure. 4.28 shows that this is the case, with added structure due to mode excitations.

4.5.2 Random Noise

Random noise, and its effects on intense charged particle beams, are almost unavoidable in high-intensity accelerators. Random noise includes machine imperfections, such as variations in the strength of the quadruupole magnets, misalignment of quadrupole magnets, jitter of power supplies, hardware irregularities that establish fluctuating image-charge forces, etc [110]. In general, random noise serves as a continuous supply of free energy to the beam particles, which results in degradation of an intense beam's quality including emittance growth, larger rms radius, higher transverse temperature, enhanced halo formation especially over long propagation distances [88, 110, 111]. Various multiparticles Particle-In-Cell (PIC) simulations have been made to improve the understanding of the random-noise-induced beam degradation [110–113]. Strenuous experimental efforts have been made to verify the effects of random noise on intense beams using random quadrupole noise [5, 6]. In this chapter, we will focus on the effects of random dipole noise. In the alternating-gradient focusing

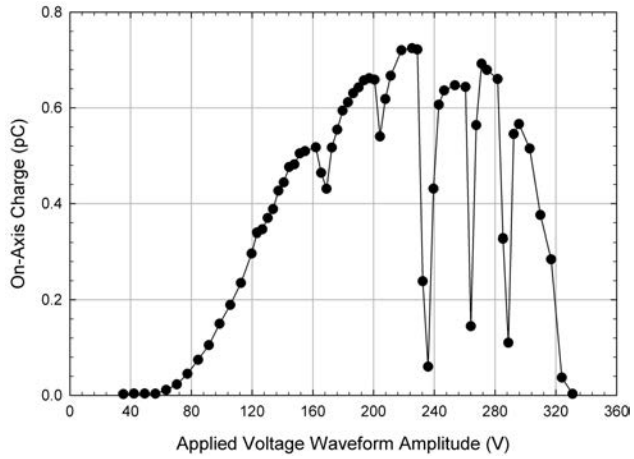

(a) half and whole-integer tune for quadrupole mode.

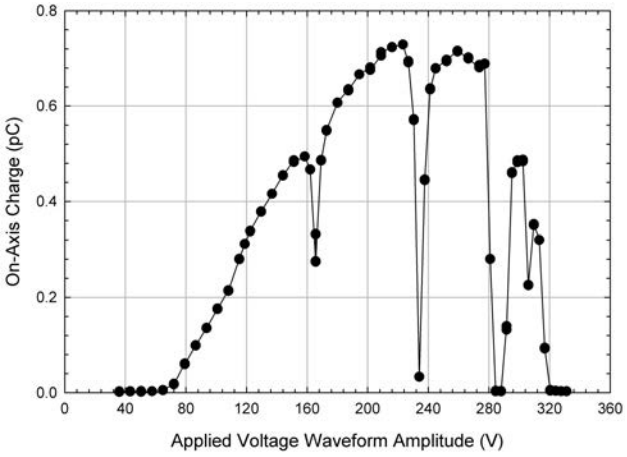

(b) whole-integer tune for dipole mode.

Figure 4.28: Half and whole-integger turn for quadrupole mode. (a) 2% coherent quadrupole perturbation is applied with V_0 scanned from 40 V to 350 V. Quadrupole mode excitations were observed at half-integer and whole-integer tunes. When V_0 is larger than 350 V, the single particle orbit stability is lost [12]. (b)2% coherent dipole perturbation is applied with V_0 scanned from 40 V to 350 V. Dipole mode excitations were observed at whole-integer tunes. When V_0 is larger than 350 V, the single particle orbit stability is lost [12].

system, the quadrupole magnets may each have a random transverse misalignment, and this will lead to a dipole magnetic field error in the misalignment direction. In this case, the error can be characterized by a random number Δ_n for each of n sets of magnets in the transport system. For the experiments presented here, the numbers Δ_n are Gaussian distributed with unit variance and a given amplitude. In PTSX, where a sinusoidal waveform is used, the amplitude of the nth half-period waveform is $V_0(1 + \Delta_n)$, with V_0 being the unperturbed waveform voltage amplitude. The amplitude of the Gaussian distribution from which the Δ_n are generated is called the noise amplitude denoted as a percentage of V_0. In our experiments, the ions are allowed 1200 lattice periods to relax to equilibrium state, then 1800 periods of noisy perturbation are applied, followed by 4000 lattice periods for the ions to relax to another equilibrium state. At the end of the trap, the ions are dumped onto a charge collector which measures the on-axis charge which is used to infer the on-axis number density of the previously trapped ions. Previous experiments investigated the effects of random quadrupole noise on the trapped charge bunch with moderate normalized intensity $\hat{s} \sim 0.2$. In those experiments, the effects of the random noise increased as the noise amplitude increases from 0.5%, 1.0% to 1.5%, while for each amplitude the effects increased as the noise duration increased. It was demonstrated that the random noise caused the rms radius growth, transverse temperature rise, on-axis charge density decrease, emittance growth and finally loss of particles. It should be noted that the data presented in the Refs. [6] and [5] were obtained by generating a list of Δ_n repeatedly to measure the range of possible outcomes. Once the range of the possible outcomes was established, 20 Δ_n series were selected to give the average outcome. Thus, the data in Refs. [6] and [5] demonstrated the average effects of certain noise amplitude and duration.

In our experiments, the external perturbation was applied to one of the long PTSX electrodes. In this case, the perturbation field is predominantly dipole, with small quadrupole field. The data in Fig. 4.29 show that a doubling of transverse temperature and the transverse emittance occurs for only 0.5% amplitude dipole noise. It is not surprising that a smaller

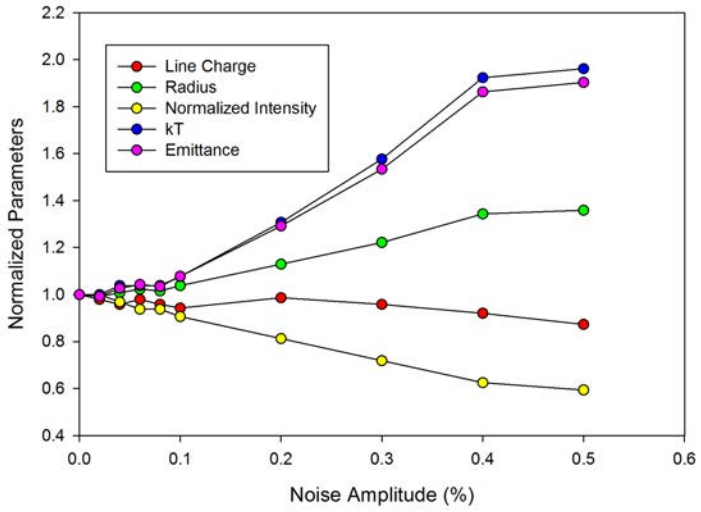

Figure 4.29: 30 ms random noise perturbation applied to a single electrode causes the rms radius, effective transverse temperature, and emittance to increase, while the normalized intensity decreases [12].

amplitude of dipole noise is needed because the dipole field is non-zero near the axis while the quadrupole noise has zero field near the axis. To verify that the results of experiments with external perturbation applied to one single electrode were due to the dipole field effect, we can either eliminate the quadrupole field component of the random noise or conduct the experiments with only the quadrupole part and no dipole contribution. The data in Fig. 4.30 demonstrate that the effect of random noise applied to a single PTSX electrode is due to the dipole component because removing the quadrupole part of the noise doesn't change the experimental results, while applying only the quadrupole part of the noise has no effect on the trapped charge bunch. It should be noted that this is due to the small effect of quadrupole noise while the noise amplitude is small as compared to Moses' data [88]. When the quadrupole noise amplitude is big enough, it can have significant effect on the trapped ion plasma which has already been demonstrated in Sec. 4.3.

When applying a dipole perturbation of 0.5% amplitude and 1800 lattice periods to one single PTSX electrode, a set of random numbers Δ_n was chosen which made the on-axis charge decrease significantly from 0.4 pC to 0.1 pC. The 1800 lattice periods corresponds to

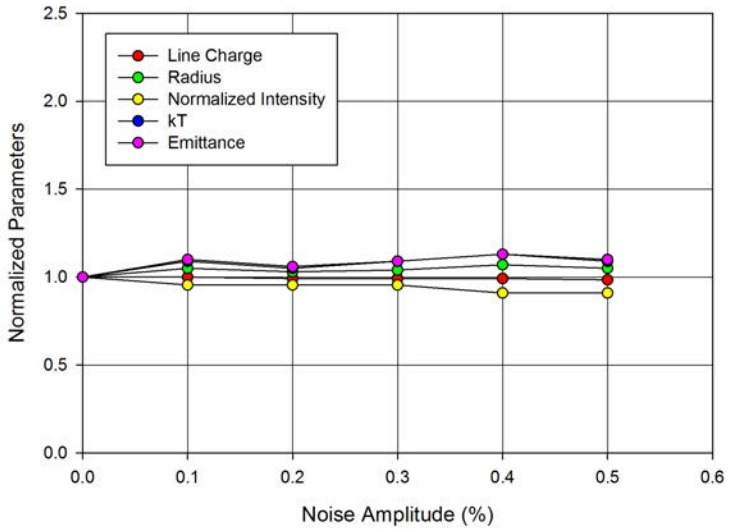

Figure 4.30: The quadrupole part of perturbation applied to a single PTSX electrode can be applied separately and has no effect on the trapped charge bunch with with with the chosen noise amplitude. This verifies that the effect of random noise applied to a single PTSX electrode is due to the dipole component [12].

30 ms perturbation so that the frequency resolution of the Fourier transform of the waveform is $\delta f = 33$ Hz. Due to the 50 ns clock time of the internal function generator, the maximum frequency in the Fourier spectrum is 10 MHz. The spectrum of the waveform was modified by removing all the frequency components from zero up to frequency f which is demonstrated in Fig. 4.31. Figure. 4.32 (a) shows that the damaging effect of dipole noise is eliminated and the on-axis charge is restored to the unperturbed value of 0.4 pC, when the filter removes the frequency component at 8.0667 kHz, which corresponds the dipole mode frequency. The normalized intensity is $\hat{s} \sim 0.19$ in this case. Note that there is no further increase in the on-axis charge when the filter also removes the frequency components near the quadrupole mode frequency $2f_q$. To further investigate if the damaging effect of the dipole noise if due to the resonance between the plasma bunch and the dipole noise at the dipole frequency 8.0667 kHz, we filter only one 33.3 Hz-wide frequency component of waveform spectrum each time. In Fig. 4.33 (a), where the normalized intensity $\hat{s} \sim 0.19$, it is demonstrated that only when

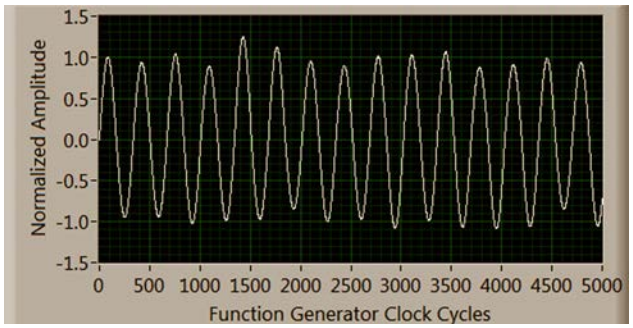

(a) First 15 periods of waveform before passing the filter.

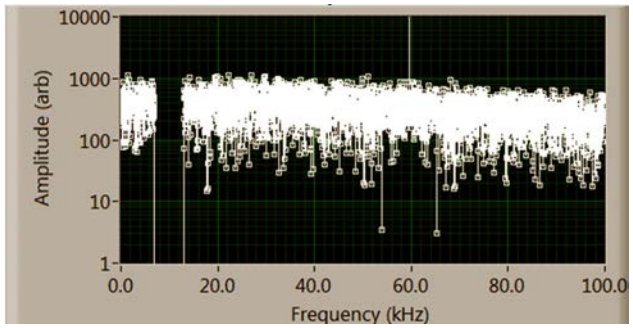

(b) First 100 kHz of the FFT of the waveform. Frequency components between 6 kHz and 12 kHz are removed.

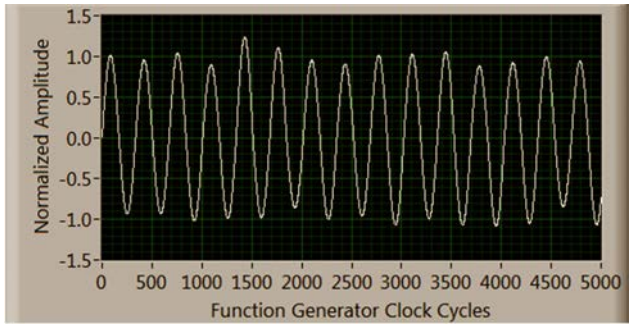

(c) First 15 periods of the waveform after passing the filter.

Figure 4.31: Demonstration of frequency components removal in Labview. An example of 10% perturbation is used to make it easy to see.

the frequency component of the spectrum at dipole mode frequency 8.0667 kHz was removed did the on-axis charge return to the unperturbed level.

Filtering the waveform applied to the PTSX electrodes is quite simple, while filtering spectrum of errors of a set of quadrupole magnets would be rather difficult. Instead of filtering the spectrum errors, it is possible to change the spectrum by manipulating the waveform in the time domain by shuffling the random numbers in a given list of Δ_n. For example, in a 30 ms dipole perturbation, there are 3600 random numbers. By shuffling the

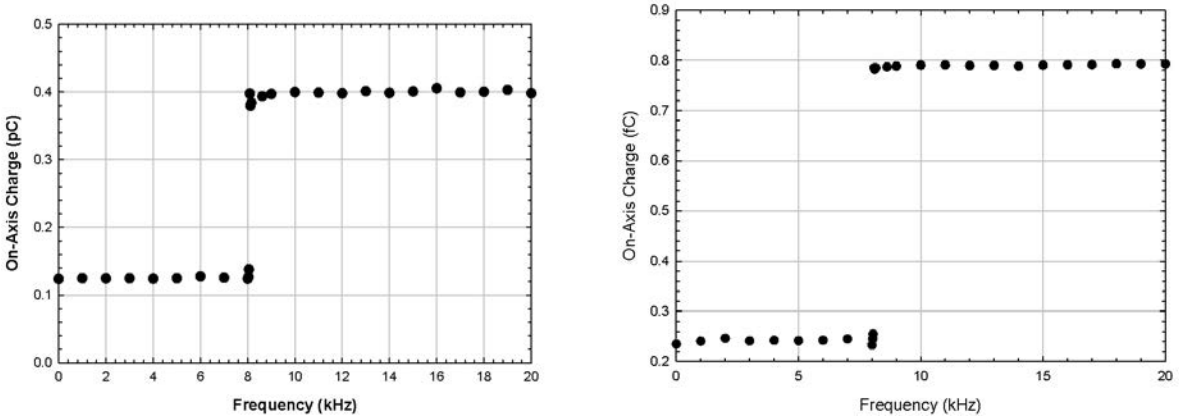

(a) s = 0.19. (b) s = 0.39

Figure 4.32: All frequency components from zero up to frequency f were removed by a low-pass filter. When the dipole mode frequency component at 8.0667 kHz was removed, the dipole perturbation effect was eliminated and the on-axis charge was back to unperturbed level.

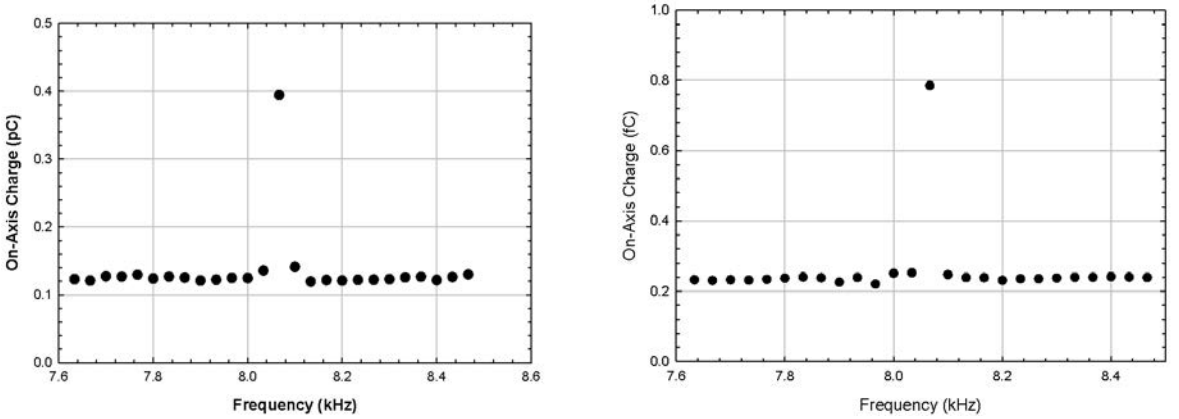

(a) s = 0.19 (b) s = 0.39

Figure 4.33: Only one 33.3 Hz-wide frequency component of the waveform spectrum was removed each time by a low-pass filter. When the dipole mode frequency component at 8.0667 kHz was removed, the dipole perturbation effect was eliminated and the on-axis charge was back to unperturbed level.

random numbers, we can find proper orders of the random numbers which yield a spectrum with near-zero amplitude at the dipole mode frequency 8.0667 kHz. In Fig. 4.34, it is shown that the on-axis charge is almost a monotonic function of the amplitude of dipole mode

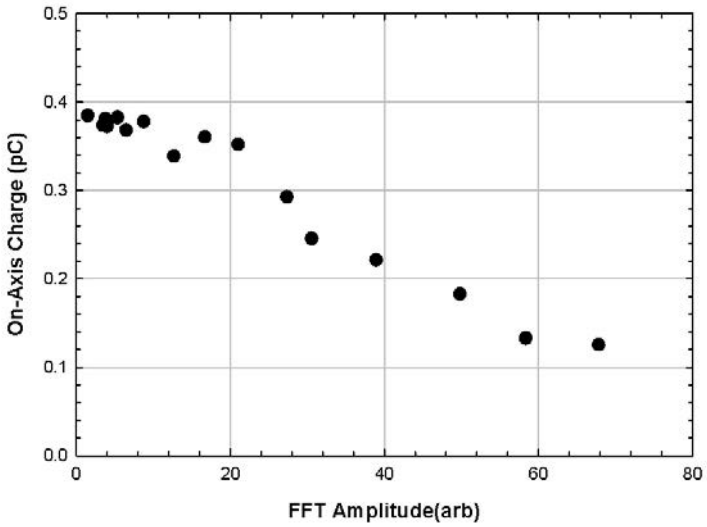

Figure 4.34: While the amplitude of the frequency component at the dipole frequency 8.0667 kHz increases, the on-axis charge decreases. We can shuffle the random numbers of a given list Δ_n to make the amplitude of the dipole mode frequency component near zero.

frequency component. By re-ordering the random numbers which yields a spectrum with near-zero amplitude at the dipole mode frequency 8.0667 kHz, we can effectively eliminate the damaging effects of the dipole noise. Simply sorting the list of random numbers Δ_n also suffices to remove the frequency component of at the dipole mode frequency, but it could bring some undesirable changes such as the gradual changes in the transverse focusing frequency.

Similar experiments for a quadrupole perturbation with 1% amplitude and a duration of 1800 lattice periods were conducted and the results were shown in Fig. 4.35. The changes of the on-axis charge are more gradual as the width of the filter window is increased than the dipole mode case and also exhibits a plateau above 17.5 kHz. The results show that there are two broad peaks at 16.4 kHz and 16.9 kHz near the quadrupole mode frequency $2f_q$. Due to their breadths, removing a single 33 Hz-wide frequency component is not sufficient to eliminate the adverse effect of the quadrupole noise. However, a filter window with 1 kHz width centered at 16.5 kHz is sufficient to restore the on-axis charge to its unperturbed value.

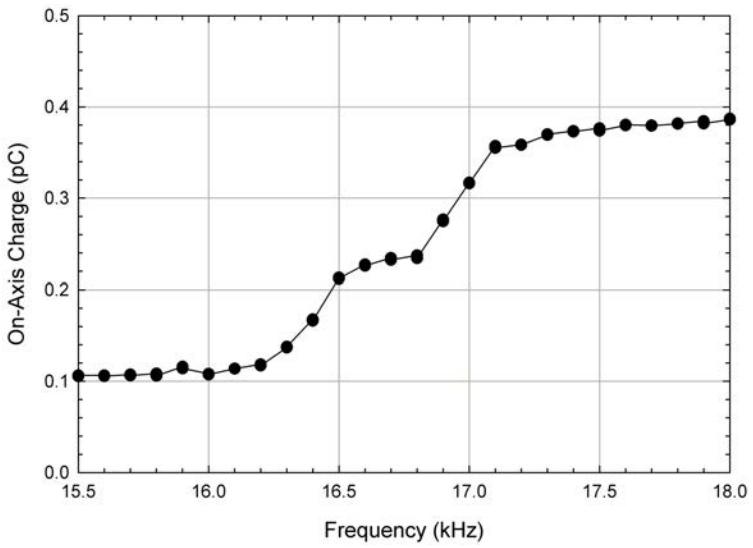

Figure 4.35: All the frequency components from zero up to frequency f were removed by a low-pass filter. When all components below 17.5 kHz were removed, the damaging effects of the quadrupole noise were eliminated.

In this section, we have shown that both dipole mode and quadrupole modes can be excited using either dipole noise or quadrupole noise. The dipole mode is quite narrow and by eliminating an individual 33 Hz-wide frequency component at the dipole mode frequency is sufficient to eliminate the adverse effect of the dipole noise. By re-ordering the random numbers of a given list Δ_n, we are able to choose the proper order of the random numbers which yields a spectrum with near-zero amplitude at the dipole mode frequency and restore the on-axis charge to its unperturbed value. The quadrupole data shows there are two broad peaks near the quadrupole mode frequency $2f_q$. Due to their finite breadths, a wider filter window is needed to completely eliminate the damaging effect of quadrupole noise.

4.6 Summary and Discussion

The high intensity charged particle beams propagating in the magnetic alternating-ingredient focusing system support a wide range of collective modes. These collective modes play an important role in furthering our understanding of the beam dynamics of the charged particle beams. Among those collective modes, we focus on the quadrupole and dipole modes which

have definite structures and easily excited by external perturbation. In Sec. 4.2, we briefly described the motivation for collective mode studies and the classic KV smooth-focusing model for quadrupole and dipole modes. Analytic expressions of the quadrupole and dipole modes were obtained using the KV model. In Sec. 4.3, we discussed the excitation of the quadrupole mode using a beat drive and a linear drive scheme, respectively. The quadrupole mode was successfully driven in both cases and effects of external perturbation on beam characteristics were investigated. We found the plasma bunch had a strong response to the external perturbation when the quadrupole mode of the charge bunch resonated with the external perturbation. The charge bunch was heated and expanded due to the resonance and usually particle loss was accompanied. 3D Warp simulation was conducted to facilitate our understanding of the experimental results. As expected, the simulation results agreed well with the experimental results and they both show weak dependence of the mode frequency on the normalized intensity $\hat{s}$, while the theoretical model shows strong dependence of the mode frequency on the $\hat{s}$. The theoretical KV models assumes uniform number density in space and Gaussian distribution in transverse velocity. While in our case, the radial number density profile is more like a Gaussian distribution. Although the KV model is not tailored to our beam profile, it is so far the closest theory we can refer to. In Sec. 4.5, we discussed the application of quadrupole and dipole modes in studying the effects of coherent periodic resonances and random noise. When the coherent periodic perturbations resonate with the collective modes particularly dipole or quadruole modes, the beam was degraded and the degradation extent depends on the perturbation duration time and the perturbation amplitudes. The random noise applied can be decomposed a finite summation of sin waves of a wide range of frequencies. It is demonstrated that not all random noise is damaging to the charge bunch and it is damaging while it has the sin wave components of the collective mode frequencies. We also show that some random noise is introduced by the faulty magnets and we can eliminate certain sin wave components by rearranging the magnets. This finding has practical benefits in designing and manufacturing the next-generation accelerator

magnets because the inaccuracy tolerance of the magnet field strength is increased and the manufacturing cost is lowered accordingly. Despite significant progress made on the study of collective modes, there are still a multitude of questions unanswered such as the mechanism of the resonance between the collective mode and the external perturbation and the cause of the rich mode structures near $2f_q$ for some quadrupole excitation data. These will be interesting topics for future research.

Chapter 5

Laser-Induced-Fluorescence (LIF) Diagnostic

5.1 Introduction

Previous experiments using a cesium ion source and a radially scanning charge collector in PTSX have been very successful in studying beam compression, injection mismatch, machine imperfection effects [88] and collective modes **(Chapter 4)**. However, the scanning charge collector is a destructive diagnostic method. The presence of the collector disk affects the nearby electric field distribution which reduces the measurement accuracy of the ion density profile. In addition, the measured density profile is a time-averaged density profile of the plasma bunch, meaning that it is impossible to infer the instantaneous density profile at a specific position. For *in-situ* and non-destructive measurements of the transverse density profile and the velocity distribution of the plasma in the PTSX device [114], which are essential for the detailed study of beam mismatch and collective oscillation of beam envelope, a laser-induced-fluorescence (LIF) diagnostic system has been developed. LIF has a wide range of applications in many areas such as the study of molecular structures, detection of selective species, flow visualization, beam density and velocity distribution measurements,

and so on. The optical transitions of barium ions are more suitable for LIF than those of cesium ions, and so barium ions have been chosen as the preferred ion species [2, 115].

In Sec. 5.2, the development of the new barium ion source and the initial test results of the source are presented. We discuss the test results of the new barium ion source under two circumstances. In one instance, the barium ion source was tested in an independent chamber, while in another case, the barium ion source was tested in the PTSX chamber. We found out in both circumstances, the barium ion source remained stable for a sufficiently long period of time to carry out experiments. In Sec. 5.4, we compare the LIF data with the experimental data obtained by the charge collector and show the reconstructed radial density profile.

5.2 Development of New Barium Ion Source

5.2.1 Theoretical Consideration

Barium ions are produced at a hot metal surface by contact ionization. Traditionally, rhenium and tungsten have been used for the hot metal plate to produce both ions by contact ionization, and also electrons by thermionic emission. Iridium is chosen for its higher work function than rhenium and tungsten and high melting point. Iridium's work function is 5.40 eV, and its melting point is 2466 °C.

Fig. 5.1 shows the available optical transition lines of singly ionized barium ions. The transition from the excited state $6^2P_{1/2}$ to $5^2D_{3/2}$ metastable state or that from the excited state $6^2P_{3/2}$ to $5^2D_{5/2}$ metastable state is considered because there is only one available laser source and most of the barium ions are created in the ground state, which will be shown later in the section. About 24.5% of the ions excited from the ground state $6^2S_{1/2}$ to the excited state $6^2P_{1/2}$ decay to the $5^2D_{3/2}$ metastable state almost immediately (8 ns), emitting red light (649.69 nm), while about 27% of the ions excited from the ground state $6^2S_{1/2}$ to the excited state $6^2P_{3/2}$ decay to the $5^2D_{5/2}$ metastable state, emitting orange light (614.17 nm).

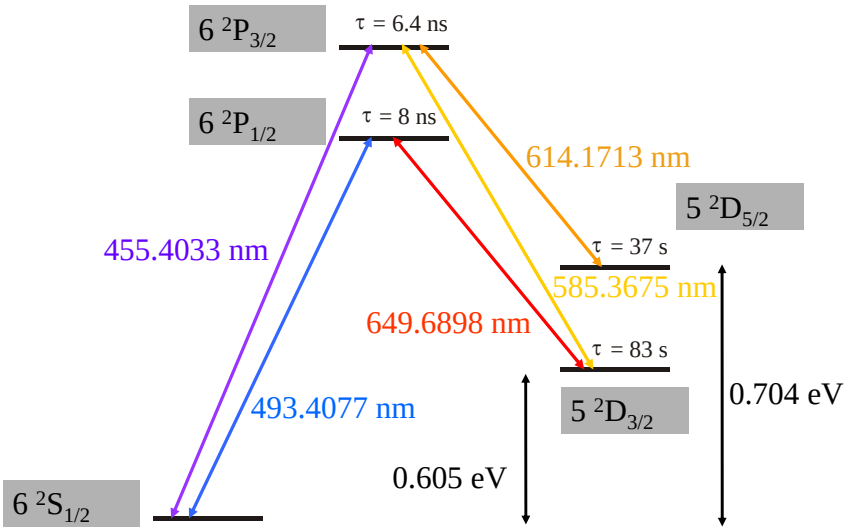

Figure 5.1: Energy level diagram for Ba^+ with transition wavelengths in air, natural lifetimes τ, and energy level differences between the ground state and metastable states [116].

The ionization probability for contact ionization can be calculated using the Saha-Langmuir equation for thermal equilibrium conditions [117]. Since the two metastable states of barium ions lie within about 0.7 eV of the ground state (see Fig. 5.1), the possibility of the ion being excited into metastable states must be considered as well. Therefore, the ionization probabilities for the ground state ions (P_i) and the metastable ions (P_i^*) are estimated by

$$P_i = \frac{g_i}{g_a \exp\left(\left(E_i - W\right)/T\right) + g_i + \sum_* g_i^* \exp\left(-\Delta E^*/T\right)}, \tag{5.1}$$

$$P_i^* = \frac{g_i^* \exp\left(-\Delta E^*/T\right)}{g_a \exp\left(\left(E_i - W\right)/T\right) + g_i + \sum_* g_i^* \exp\left(-\Delta E^*/T\right)}. \tag{5.2}$$

where W and T are the work function and temperature of the hot metal plate (iridium in this case), E_i is the ionization potential of the atom, and ΔE^* is the energy difference between the ground and metastable states. The quantities g_a, g_i, and g_i^* are statistical weights of the atoms, ground state ions, and metastable ions, respectively. The statistical weight g can be calculated from the total angular momentum quantum number J using the relationship,

$g = 2J + 1$. The work function of several typical metals is presented in Table. 5.1. Since the ionization energy of barium is very high (E_i=5.21eV), iridium, with a higher work function (W=5.4eV), is chosen as the hot plate metal to increase the ionization probability.

It is interesting to note that for the case of contact ionization of barium vapor on iridium, E_i(= 5.21 eV) < W(= 5.40 eV) and P_i^* is decreases monotonically with T. This might suggest that iridium ionizer could be operated at a very low temperature. However, Eq. (5.2) is only valid when the metal surface temperature is above the critical temperature (or threshold temperature) T_c [118, 119]. When $T < T_c$, the evaporation rate of atoms decreases and the surface coverage of adsorbed atoms increases, which in turn, causes the effective work function of the composite surface to decrease and finally results in a sharp drop in net ion current [118, 119]. Therefore, it is essential to maintain the surface of the ionizer above the critical temperature. The critical temperature for contact ionization on iridium differs for different ion species. For most cases, $T_c \gtrsim 1200$ ° C [119]. Empirically, the ionizer temperature of the newly developed barium ion source is set to 1200 °C. The ionizer temperature can go higher than 1200 °C if necessary and it will still be well below the melting point for iridium. For an ionizer temperature of 1200 °C, it is estimated from Eqs. (5.1) and (5.2) that the fraction of barium ions produced by the hot platinum surface will be 97.2% in the ground state ($6^2S_{1/2}$), 1.66% in the $5^2D_{3/2}$ metastable state, and 1.14% in the $5^2D_{5/2}$ metastable state. In general, there are two schemes of using the optical transition lines for the LIF diagnostic purpose. The first scheme is to pump the ions from the ground state ($6^2S_{1/2}$) to the exited state ($6^2P_{1/2}$ or $6^2P_{3/2}$), then observe the emission light when the ions decay from the excited state to the metastable state. The second scheme is to pump the ions from the ground state ($6^2S_{1/2}$) to the exited state ($6^2P_{1/2}$ or $6^2P_{3/2}$), then observe the emission light when the ions decay from the excited state to the ground state. The advantage of the first scheme lies in observing the emission of a different wavelength from the incident light. In that case, the background reflection from the incident light can be suppressed by adding an extra filter with limit bandwidth. But the downside of the first scheme is also

Table 5.1: Work Function for Various Materials

Material	**Symbol**	**Work Function (eV)**
Molybdenum	Mo	4.15
Tungsten	W	4.54
Iridium	Ir	5.40
Platinum	Pt	5.32
Rhenium	Re	4.85
Tantalum	Ta	4.12

significant. Because the typical ion density in PTSX is about 10^5 cm^{-3}, assuming all the ions are pumped from the ground state $6^2S_{1/2}$ to either excited state $6^2P_{1/2}$ or $6^2P_{3/2}$, given the decay ratio of about 25%, the effective ion density for detection for the first scheme will be about $10^3 \sim 10^4$ cm^{-3}, which is slightly above the detection limit for typical LIF diagnostics [120]. The downside of the second scheme results from observing the emission of the same wavelength of the incident light. But by adding a stack of razor blades as a laser dump and an anti-reflection coating, the stray light can be significantly reduced. The advantage of the second scheme is due to the higher effective ion density due to the higher decay ratio ($\sim$ 75%). In our experiment, we chose the second scheme and chose 493.4077 nm as our target wavelength. Even if the effective ion density for the second scheme is much larger than the first scheme, it is not much higher than the typical detection limit. Hence, suppression of background signals and sufficiently long integration times are essential for meaningful LIF data.

5.2.2 New Barium Ion Source Assembly

The new barium ion source increases the barium ion density in the PTSX vacuum chamber as well as decreasing the number of neutral barium atoms that enter the PTSX vacuum chamber as compared to the previous barium source [88]. The main components of the barium ion source include an atomic oven, an iridium hot-plate ionizer, an extraction mesh,

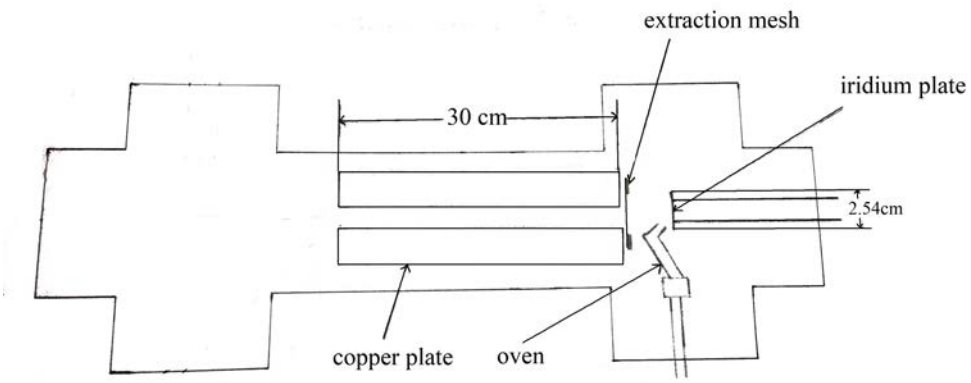

Figure 5.2: Schematic diagram of the new barium ion source assembly.

and copper plates shown in Fig. 5.2. Figure 5.3 shows photographs of the new barium ion source.

The atomic oven is a 0.5″ diameter one-end-open tube with a resistive band heater wrapped around the tube. The barium in the oven can be heated to temperatures up to 800°C. It is common to heat the oven up to high temperatures for a short while to decompose oxides and hydroxides that may come from handling materials. Lower temperatures between 400°C and 500°C are usually sufficient to produce ion densities near 10^6cm^{-3}. The barium vapor coming out of the atomic oven will free-stream to the iridium hot plate which is held at 1200°C. Barium atoms which make contact with the hot plate will become singly-charged ions through contact ionization with approximate 82% probability. The other neutral atoms which fail to be ionized leave the iridium plate isotropically. In contrast, the positve dc bias voltage applied to the iridium plate is able to expel the barium ions produced from contact ionization and send them into the 12″-long, 4″-diameter guiding pipe. Once in the pipe, the

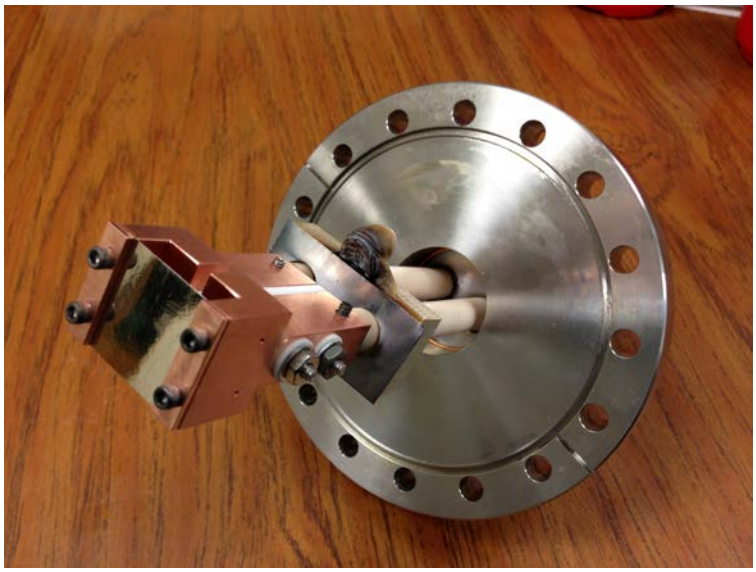

(a) Iridium hot plate. The 1" × 1" iridium plate is mounted on two copper pieces in a way that the movement of copper pieces doesn't distort the iridium plate.

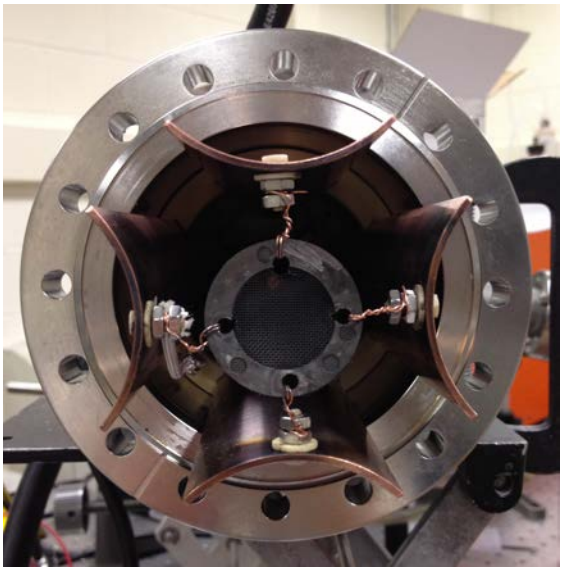

(b) Extraction grid and copper plates. The extraction grid is mounted to the four copper plates using ceramic screws for insulation purpose.

(c) Barium ion source in operation. The assembly includes an iridium plate(right), an oven(center), an extraction grid and four copper plates(left).

Figure 5.3: Photographs of the barium ion source.

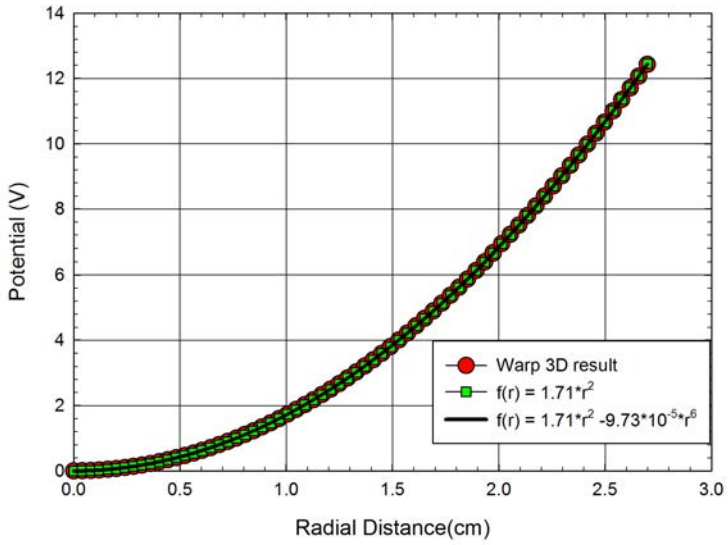

Figure 5.4: Warp 3D simulation shows the electric field near the center is mostly quadrupole with 2.77 cm being the distance between the 2.5″ copper plate and the center of the 4″ pipe.

ions are transversely confined by driving four copper plates inside the pipe with oscillating quadrupole voltages. The four plates are formed from a 2.5" diameter pipe that is quartered and mounted with the quadrants inverted so that they approximate the hyperbolic shape required an ideal quadrupole field. Using Warp 3D simulations for guidance, we chose 2.77 cm as the distance between the edge of the 2.5" copper plate to the center of the 4" pipe in such a manner that the electric field near the center is mostly quadrupole. As shown in Fig. 5.4, the electric potential from Warp 3D simulation agrees well with a polynomial fit in which only the quadrupole term is considered. The Warp 3D results also agree well with a polynomial fit in which both quadrupole and octuple terms are considered. These two polynomial fits share the same coefficient for the quadrupole term and the coefficient for the octuple term is much smaller than that of the quadrupole term. In our case, the ratio of these two coefficients is 5.7×10^{-5}. Adding more terms into the polynomial fit doesn't improve the fit which indicates that the electric potential is mostly quadrupolar.

Adding a 12″-long guiding pipe between the main PTSX vacuum chamber and the barium ion source is a significant improvement compared to the previous barium ion source.

Neutral atoms which enter the pipe adhere to the pipe wall rather than contaminate the main chamber. The driving voltages on the copper plates have the same frequency as, but 10 times smaller amplitude than, the voltages applied to the main PTSX electrodes. The reason why the driving voltages are 10 times smaller than those on the PTSX electrodes is that the relative size of the copper plates is much smaller and it doesn't need large voltage to maintain the same smooth-focusing frequency as we have in PTSX electrodes. Fig. 5.5 shows the use of four cylindrical copper rods to create the quadrupole focusing field in the pipe. In this way, the ions will be well-confined transversely and both the vacuum phase advance and the average focusing frequency within the four copper plates will be the same as in PTSX. The long guiding pipe is extended into the main PTSX vacuum chamber so that the ions are still confined by the quadrupole field generated by the 40-cm injection electrode right after exiting the driven copper plates. The size of the copper plates and the relative position with respect to the guiding pipe are shown in Fig. 5.6

Vacuum conditions of the new ion source are worth considerations since, when the new ion source is ready to use, the six-way cross will be attached to the main PTSX vacuum chamber. This raises a question whether the pressure in the PTSX chamber will still be low enough for meaningful experiments. The general operating pressure in the PTSX chamber is of the order of 10^{-10} – 10^{-9} Torr, while the pressure in the six-way cross is of the order of 10^{-7} – 10^{-6} Torr. When these two chambers are connected by a pipe, there would be gas flowing from the six-way cross to the PTSX chamber due to the pressure gradient. The quantity describing the capability of a pump pulling out gas molecules is the throughput $Q = P_{chamber} \times S_{pump}$, where $P_{chamber}$ is the gas pressure with the units of Torr and S_{pump} is the pumping speed with the units of ℓ/s. The gas flow from the six-way cross to the PTSX chamber is given by $Q_{pipe} = (P_{oven}\text{-}P_{chamber}) \times C$, where P_{oven} is the gas pressure inside the six-way cross, and C is the conductance of the pipe for gas flow. For the low-pressure regime, the conductance C is approximated by $C = \pi v d^3/12l$, where v, d, l are the thermal velocity of gas molecules, the diameter and length of the pipe, respectively. All the other gas sources

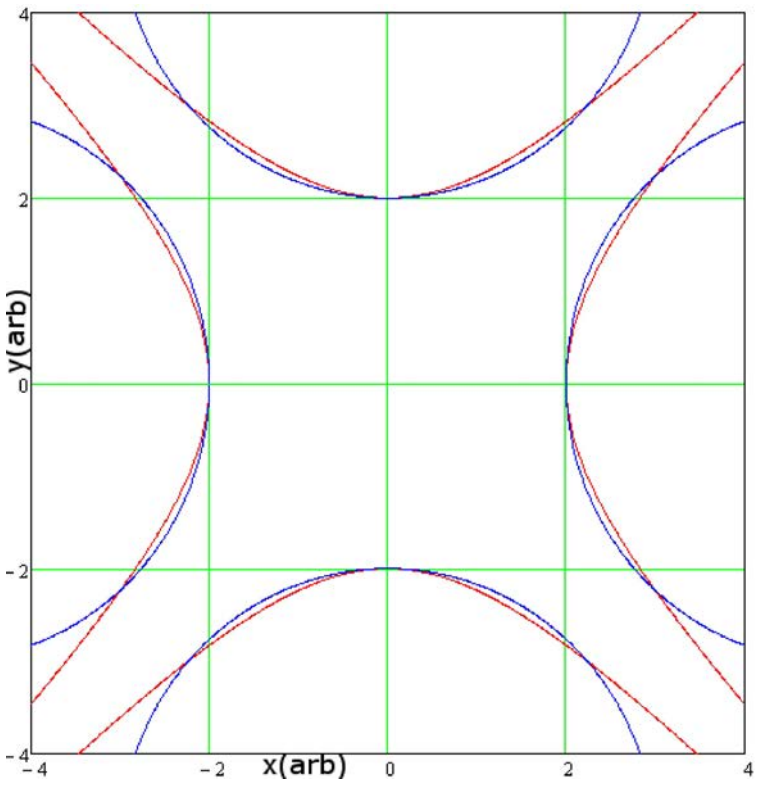

Figure 5.5: Four copper plates are used to approximate the hyperbolic contours of the electric equipotentials in PTSX.

including possible leakage and vapors escaping the chamber walls are included in another term Q_{outgas}, where Q_{outgas} is known from the pumping speed and operating pressure. In equilibrium, we have $P_{chamber} \times S_{pump} = Q_{pipe} + Q_{outgas}$. Assuming P_{oven} is 10^{-6} Torr, $P_{chamber}$ will be of the order of 10^{-8} – 10^{-7} Torr which is adequate for experiments.

5.2.3 Test Results of the New Barium Ion Source

Testing Ion Source Independently

The new barium ion source was initially tested in an independent chamber whose configuration has been shown in Sec. 5.2. The radial number density of barium ions measured on the charge collector is determined by parameters such as bias voltage on the iridium hot plate, the bias voltage on the extraction grid, the hot plate temperature, the oven temperature, the oscillating voltage amplitude and frequency applied to the copper plates. Those parameters

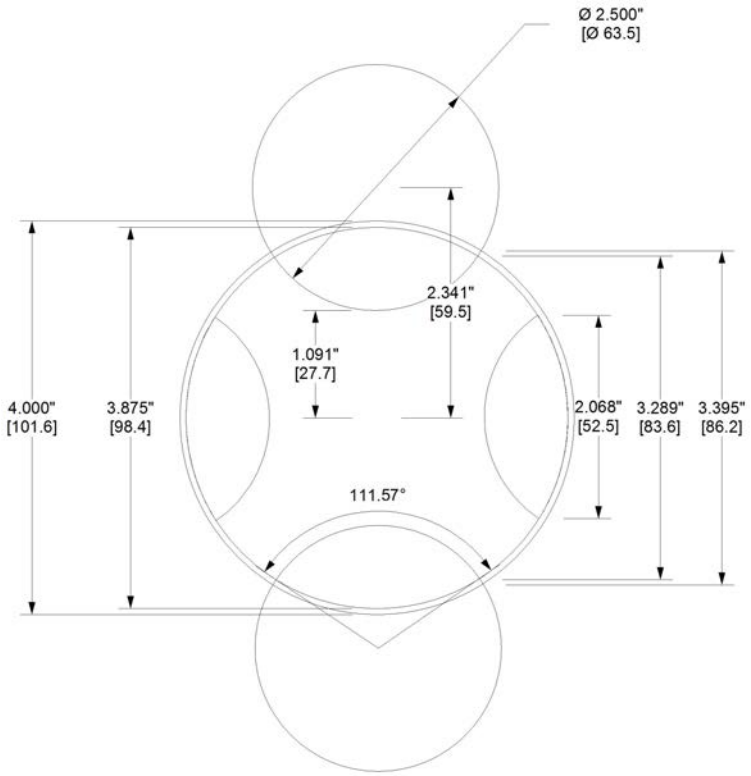

Figure 5.6: Configurations of the copper plates. Each copper plate spans 90 degrees and symmetrically distributed.

need to be selected carefully to optimize the performance of the barium ion source. Not only do we care about the on-axis charge density, we also care about the shape of the radial density profiles. Ideally, we would like to see a Gaussian or quasi-Gaussian distribution of radial charge density. Bearing that goal in mind, typically we vary the values of a particular parameter while keeping others constant, then we measure the radial density profiles, and plot them on the same graph. By comparing the characteristics of those radial density profiles, we choose the operating range of a particular parameter.

The first parameter we aimed to optimize was the bias voltage V_s on the iridium plate. V_s determines the axial velocity of the barium ions, and ideally we desire small axial velocity to allow the ions to go through many lattice periods before being dumped into the end of PTSX chamber. In that case, the ion beam is allowed enough time to reach a quasi-equilibrium state before being measured. For the previous cesium ion source, the typical V_s is 3 V. We

would like to use similar V_s for the barium ion source, so the values of V_s being tested did not exceed 10 V. Figure 5.7 shows the radial number density profiles at different V_s under various oven temperatures. The data for the three graphs shown in Fig. 5.7 used the same hot plate temperature $T_{iridium} = 1100°\text{C}$, the same oscillating voltage amplitude applied to the copper plates $V_0 = 13.5$ V, and the same oscillating voltage frequency $f_0 = 60$ kHz. Note that the radial density profiles of barium ions are not as symmetric as those acquired using the cesium ion source. This is probably due to the fact that the barium ions are not produced symmetrically. The neutral barium vapor coming out of the oven does not make contact with the iridium hot plate uniformly which results in an asymmetric initial radial density distribution. The initial asymmetric ion distribution is expected to relax to a Gaussian or quasi-Gaussian distribution during the propagation in the PTSX chamber. Further, when the on-axis density initially increases as V_s increases, then drops once the V_s passes a turning point. We also noticed that when the bias voltage is small ($V_s < 4$ V), the radial density profiles are more symmetric than those acquired under higher bias voltages. Fig. 5.7 indicates the optimal bias voltage on the iridium plate V_s is between 2 V and 4 V. With regard to the dependence of radial density profiles on oven temperature, we notice that the radial density profiles obtained at $T_{oven} = 420°\text{C}$ are more symmetric than those acquired at $T_{oven} = 320°\text{C}$ and $T_{oven} = 365°\text{C}$.

To further study the characteristics of the barium ion source, we used the same data for Fig. 5.7 and computed important quantities including the normalized intensity $\hat{s}$, the rms radius r_{rms}, the line charge density N, and the transverse temperature T. Figure 5.8 shows the computed quantities. Note that the normalized intensity $\hat{s}$ initially increases as V_s increases, and gradually decreases once it exceeds certain value. Since $\hat{s}$ is an indicator of the relative strength of space charge field to the external focusing field, for the study of high intensity charged particle beams which have strong space charge field, a high $\hat{s}$ is desired in our experiments. The operating range of 2 V to 4 V for V_s is desired to achieve a relatively high $\hat{s}$. From the rms radius point of view, the rms radius generally increases as

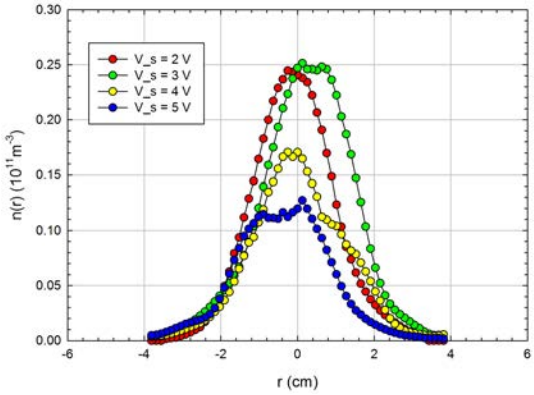

(a) $T_{oven} = 320°\text{C}$.

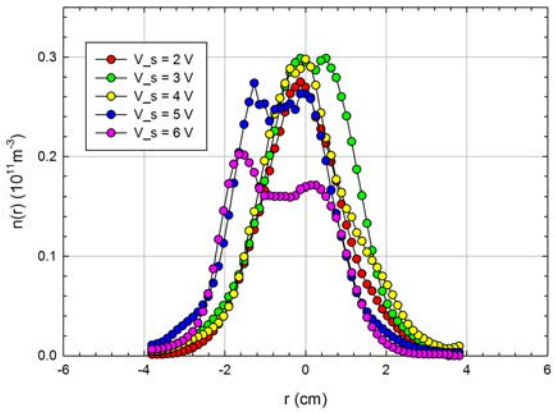

(b) $T_{oven} = 365°\text{C}$.

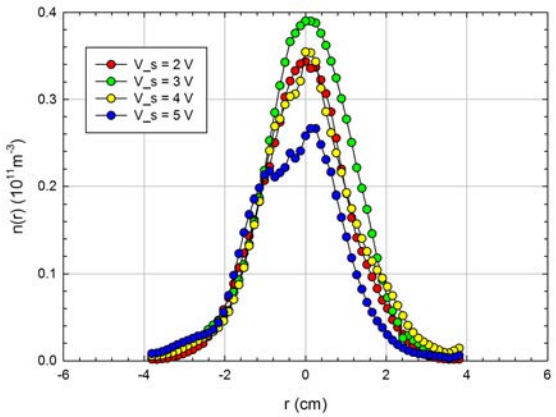

(c) $T_{oven} = 420°\text{C}$.

Figure 5.7: Radial density profiles at different V_s under various oven temperatures. Temperature on the iridium hot plate is $T_{iridium} = 1100°\text{C}$, the oscillating voltage amplitude applied to the copper plates is $V_0 = 13.5$ V, and the oscillating voltage frequency is $f_0 = 60$ kHz.

the bias voltage increases. Since the electric field from the bias voltage is not perfectly axial, barium ions are also accelerated perpendicularly which results in larger radial dispersion at higher bias voltage. The 2 V to 4 V operating range of V_s is acceptable in terms of obtaining moderate rms radius. With regard to the line charge density, it also favors low operating values of bias voltage. For the transverse temperature T, low V_s values are also desired. In summary, low V_s (2 V to 4 V), moderate oven temperature ($T_{oven} = 420°C$) are desired for the operation of the barium ion source.

Another critical parameter for the barium ion source is the oscillating voltage amplitude. It should be large enough to confine the charge particles but small enough to keep the particle orbit stable. Fig. 5.9 shows the dependence the radial density profiles on the oscillating voltage amplitude V_0. The other important parameters in obtaining the data for Fig. 5.9 include oscillating voltage frequency $f_0 = 60$ kHz, the bias voltage on the iridium plate $V_s = 1.123$ V, the oven temperature $T_{oven} = 414°C$, and the iridium plate temperature $T_{iridium} = 1300°C$. The on-axis number density initially increases as the increasing focusing field allows more particles to be confined, then it decreases gradually as large strong focusing field causes the charge particle orbit to be unstable which eventually results in particle loss. The data in Fig. 5.9 suggest that the desired oscillating voltage amplitude at 60 kHz should be around 13 V.

The stability of the barium ion source is of critical importance to us. Typically any experiment conducted on the barium ion source will last from a few minutes to a few hours. To make sure the data acquired are consistent during the experiment, we need to make sure the ion source is stable and the experimental results are reproducible within a certain degree. To test the stability of the ion source, we first choose the typical operating values for the ion source and measure the radial density profiles at different time spanning a few hours. Ideally, the profiles will overlap with each other with minor deviation. Fig. 5.10 shows the radial density profiles measured at different time are almost identical to each other which suggests a stable ion source.

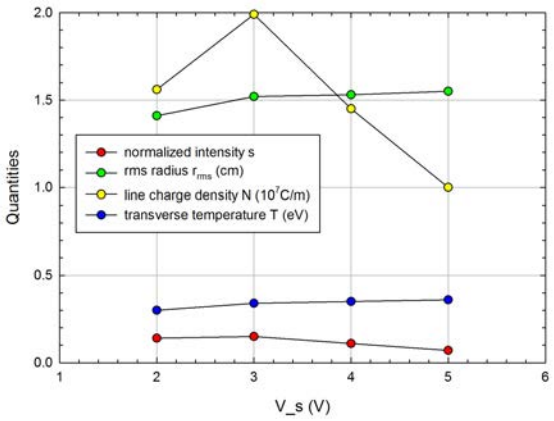

(a) $T_{oven} = 320°\text{C}$.

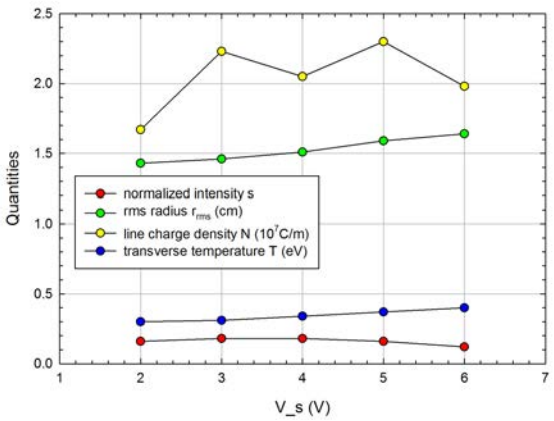

(b) $T_{oven} = 365°\text{C}$.

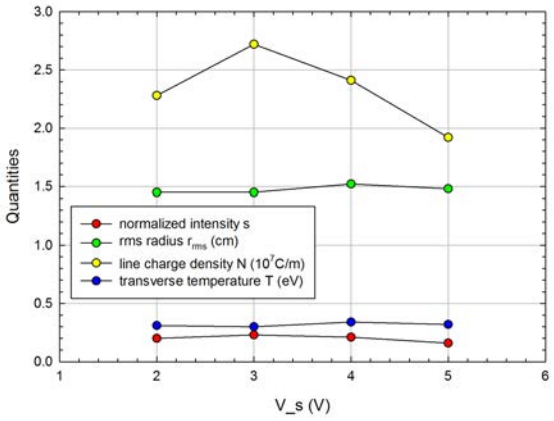

(c) $T_{oven} = 420°\text{C}$.

Figure 5.8: Quantities relevant to the radial density profiles shown in Fig. 5.7. $T_{iridium} = 1100°\text{C}$, $V_0 = 13.5$ V, $f_0 = 60$ kHz.

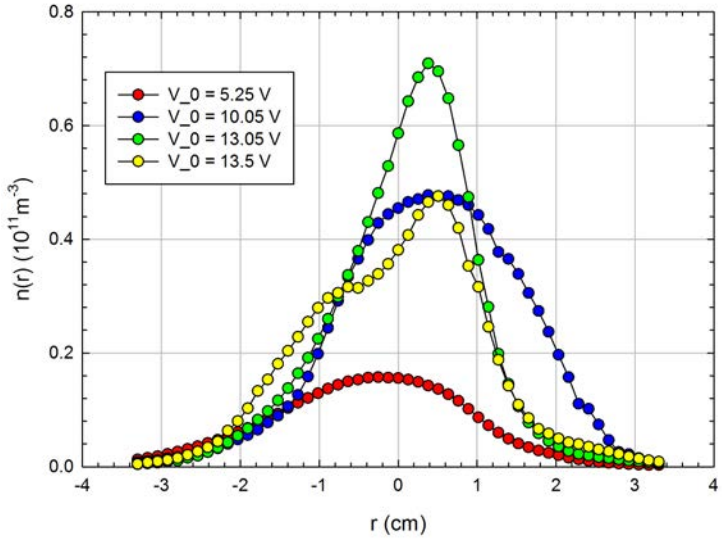

Figure 5.9: Radial density profiles at different oscillating voltage amplitudes V_0.

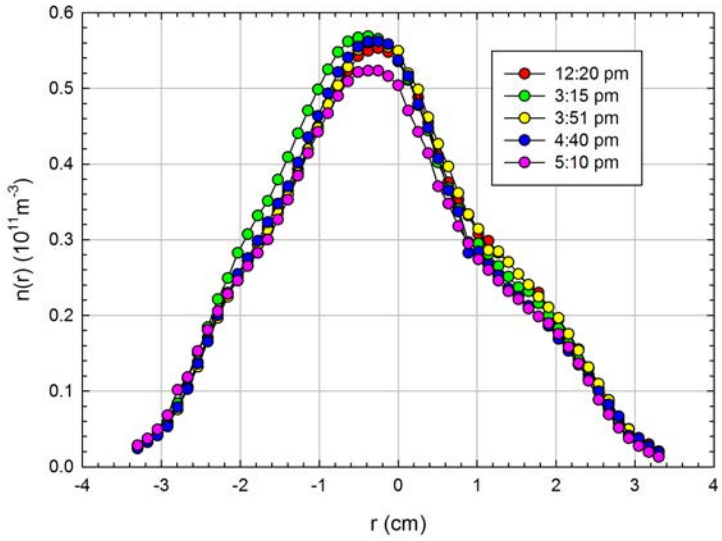

Figure 5.10: Radial density profiles at different time. $T_{oven} = 414°C$, $T_{iridium} = 1300°C$, $V_s = 1.123$ V, $f_0 = 60$ kHz.

Testing Ion Source in the PTSX Chamber

Sec. 5.2.3 discussed the test of the new barium ion source in an independent chamber, and the test results indicate a stable source with high number density of barium ions over a long period of time. In this section, we discuss the test results of the new ion source after it was

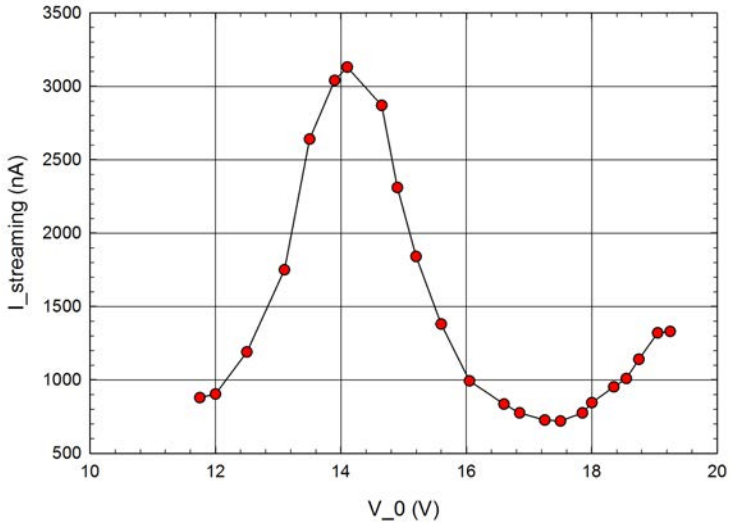

Figure 5.11: Scan of the driving voltage amplitude on the copper plates. The voltage amplitude which gives the maximum streaming current ia about 14 V, which is about 1/10 of the voltage amplitude applied to the PTSX electrodes.

installed onto the PTSX chamber. The maximum oscillating voltage amplitude the previous circuit could provide was 13.5 V which barely meets our needs. A new circuit was designed and the maximum voltage amplitude can go up to 19 V, which provides much more flexibility of optimization of the ion source. The driving voltage is set to have the same frequency as we have in the PTSX chamber which is 60 kHz. Then we scanned the voltage amplitude to find the voltage amplitude which yields the largest streaming current. Figure 5.11 shows the streaming current as a function of the voltage amplitude on the copper plates. We notice that maximum streaming current occurred around 14 V, which is 1/10 of the voltage amplitude on the PTSX electrodes. At 14 V, the smooth-focusing frequency at the copper plates and the PTSX electrodes are matched and the ion transportation is optimized.

After the voltage amplitude is optimized, we would like to optimize the bias voltage on the iridium plate. We fixed the voltage amplitude to be 14 V and frequency to be 60 kHz. The bias voltage V_s on the iridium plate is scanned. Figure 5.12 shows the streaming current as a function of a bias voltage on the iridium plate. The higher the bias voltage is, the higher

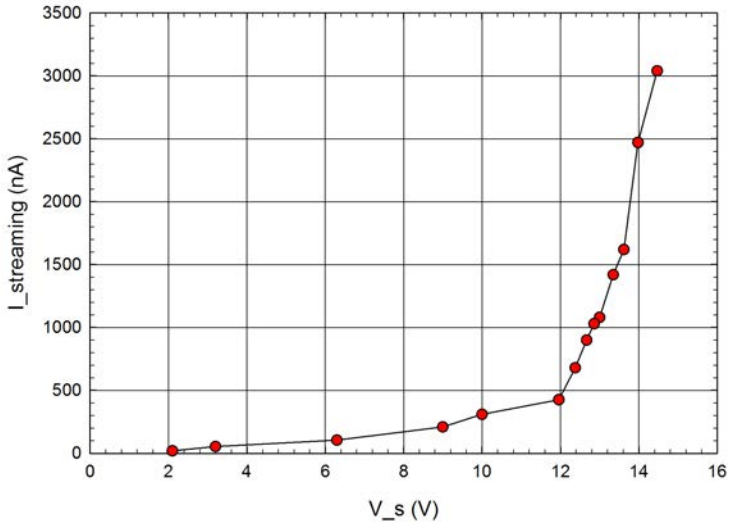

Figure 5.12: Scan of the bias voltage on the iridium plates at a fixed voltage amplitude on the copper plates. The higher the bias voltage is, the higher the streaming current is. But higher bias voltage corresponds to more energetic ion particles which is not desired. The bias voltage is chosen to be around 11 V as a trade off.

the streaming current is. But higher bias voltage means more energetic ion particles which is not desired. As a trade off, a bias voltage around 11 V is chosen.

After the bias voltage V_s and the driving voltage amplitude V_0 were optimized, we measured the radial density profiles in the streaming mode to see if the charge bunch has a nice a shape and the on-axis density is high enough. Figure 5.13 shows the number density profiles and the Gaussian fit of the experimental data. The radial density profile is approximately Gaussian except that the tail is a bit fatter than typical Gaussian shape. That could be due to the higher bias voltage we used to inject the ions. The on-axis number density is approximately 2.8×10^5 cm^{-3}, which is almost three times the typical number density for the cesium ion source. The rms radius is about 1.12 cm and the transverse temperature is about 0.16 eV. The effective normalized intensity $\hat{s}$ is about 0.72 which is much higher than our typical $\hat{s}$ for the cesium ion source (0.2). The radial density profiles suggest that the ion source is working properly together with the PTSX electrodes.

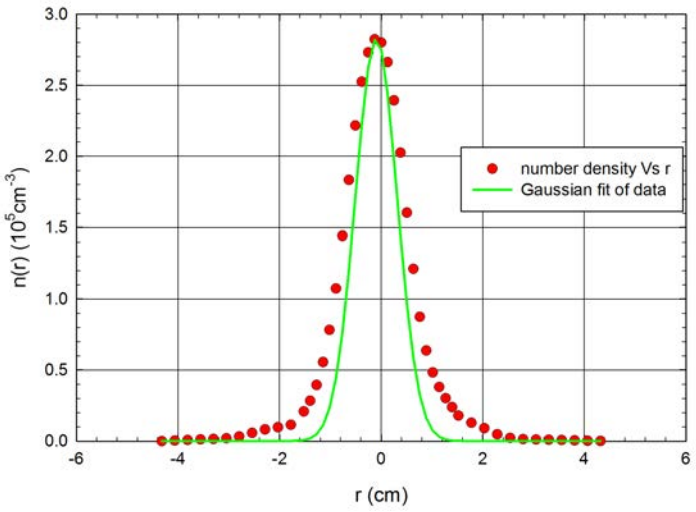

Figure 5.13: The number density profile is approximately Gaussian and the high on-axis density is favorable to the LIF diagnostic. The on-axis density is about 2.8e+5 cm^{-3}, the rms radius is about 1.12 cm, the transverse temperature is 0.16 eV and the effective normalized intensity is about 0.72.

The next step is to verify if the ion source can be operated over a long period while remaining stable. Figure 5.14 shows the radial density profiles measured in the streaming mode at different times. The radial density profiles approximately overlap with each other which suggests the barium ion source is stable over a long period.

So far, we have established a solid baseline for the source operation in the streaming mode. To make the most use of the ion source, we need to operate the ion source in the trapping mode. So the next step we will focus on optimizing the ion source in the trapping mode. Similar to the cesium ion source operation, a complete trap cycle includes the source duration t_{source}, the loading time t_{load}, the trapping time t_{trap}, the dump time t_{dump} and the rest time t_{rest}. The most important parameters are the source duration and the loading time. The source duration is set in the way that the ions fill most of the space between the two sets of the short electrodes, in the mean time reducing the number of fast ions. The loading time is set in the way that any remaining ions inside the short chamber will have enough time to exit the chamber before the positive DC bias voltages are applied to the short electrodes. The trapping time is set to make sure that there are many ions left and the

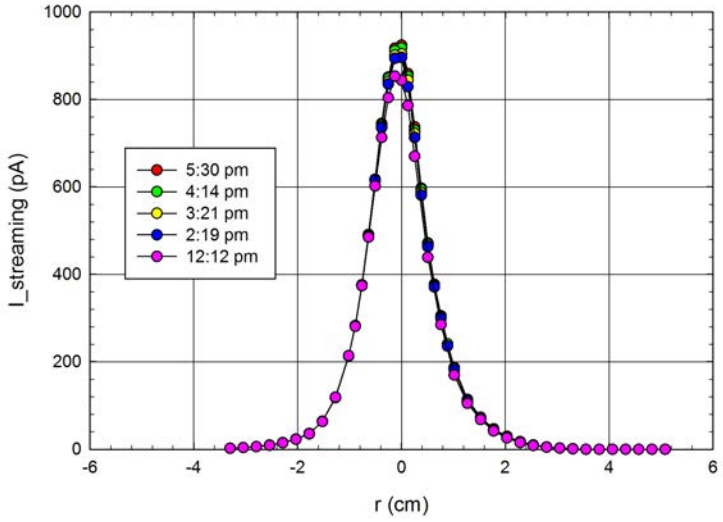

Figure 5.14: Radial density profiles measured at different times demonstrate the stability of the barium ion source.

radial density profile is not too broad. Figure 5.15 shows the radial density profiles under using different t_{source} and t_{load} while keeping the total trapping cycle 100 ms unchanged. It is noted that every single radial density profile measured in the trapping mode is much broader than those measured in the streaming mode. It is probably because the charge bunch is mismatched in the first place and after 100 ms relaxation, the collective instability due to the mismatch causes the charge bunch to expand transversely. Among the available combinations, we chose $t_{source} = 0.7$ ms and $t_{load} = 1.2$ ms to achieve the optimized radial density profiles in the trapping mode.

5.3 Laser and CCD Camera System

5.3.1 Setup of Laser and CCD Camera System

The LIF laser beam is produced by and excimer-pumped dye laser which is shown in Fig. 5.16. The excimer laser uses a mixture of xenon (Xe) and hydrogen chloride (HCl) as the working gas. The dye is a mixture of Coumarin powder and methanol. The XeCl dimer lases

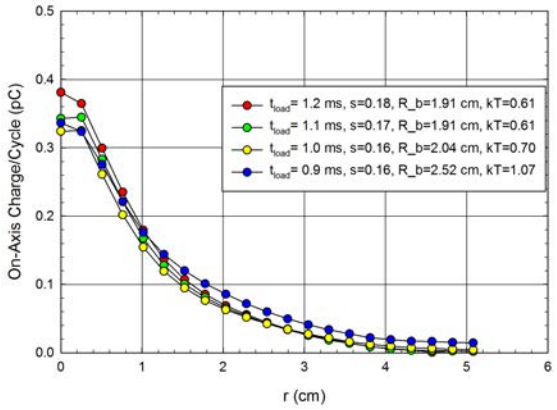

(a) t_{source} = 0.7 ms.

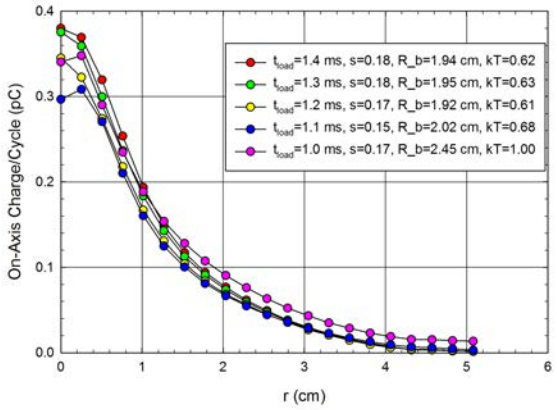

(b) t_{source} = 0.8 ms.

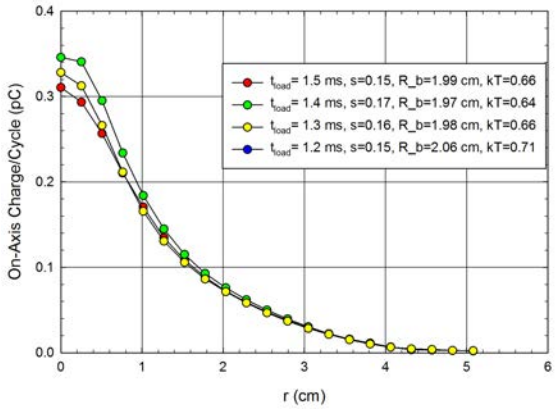

(c) t_{source} = 0.9 ms.

Figure 5.15: The radial density profiles in the trapping mode using t_{source} and t_{load}. We pick t_{source} = 0.7 ms and t_{load} = 1.2 ms as the typical values because this combination give the highest $\hat{s}$, the smallest rms radius and the lowest transverse temperature.

Figure 5.16: Laser system. The small laser on the top a counter is the dye laser. The giant laser on the floor is the excimer laser.

at a wavelength of 308 nm. Then, this laser beam intersects the dye along the propagation path where the laser beam stimulates the dye to emit photons by fluorescence with another wavelength which form the second laser beam in the dye laser. The second laser beam is used in the LIF diagnostic experiments. The repetition rate of the excimer laser is 10 Hz and, the laser beam energy per pulse is about 100 mJ and the pulse duration is about 10 ns.

Figure 5.17 shows the inside of the dye laser and the optical layout. The grating shown in Fig. 5.17 (a) is able to select a specific wavelength and filter the other wavelengths. In our case, our desired wavelength is 493.4077 nm. The bandwidth of the dye laser is 0.15 cm^{-1}, which corresponds to about 0.003 nm linewidth, because bandwidth is defined as $\Delta\lambda/\lambda^2$. The two white ceramic containers shown in Fig. 5.17 (a) are preamplifier dye cell (left) and main amplifier dye cell (right), respectively. The output light from the preamplifier dye cell go through a telescope system lying between those two dye cells before entering the main amplifier dye cell. If there is a coherent laser signal, we will be able to measure it right it goes through the preamplifier dye cell.

The second laser beam is carried by optical fiber to PTSX main chamber. The typical laser pulse energy from the eximer laser is about 100 mJ. The dye laser conversion efficiency is about 17%. The typical optical fiber conversion efficiency is about 35%. So the laser

(a) Photo of dye laser

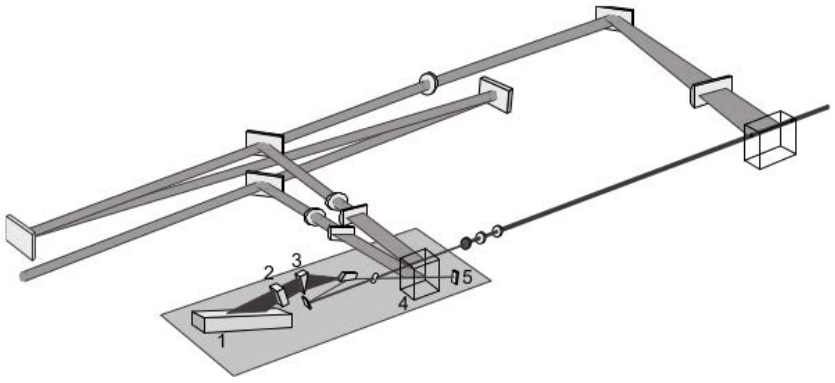

Figure 4: *ScanMate Pro 2E oscillator*

The ScanMate *Pro* oscillator consists of the following components:

- a single grating for wavelength selection covering the UV, VIS and NIR spectral range (see Figure 4, 1),
- an achromatic prism beam expander (3),
- a dye cell (4),
- a highly reflective end mirror coated for UV, VIS and NIR (5),
- an optional IB Options Module for improved linewidth operation or a Fabry-Perot etalon for ultra-narrow linewidth operation (2).

(b) Optical layout of dye laser

Figure 5.17: The dye laser system. The grating shown on (b) is able to select a specific wavelength and filter the other wavelengths. The linewidth for this dye laser is about 0.003 nm.

pulse energy available for the barium ions is about 11.9 mJ, which is enough to excite all the barium ions from the ground state to the excited state (See 5.3.2). At the fiber output, a commercial laser beam line generator has been installed to increase the detection volume and fully utilize the available barium ions. The line generator, which uses a Powell lens, transforms the collimated laser beam into a sheet with a uniform output intensity. A Powell lens with 30° fan angle can result in a detection volume with a width of ~ 11.1 cm near the PTSX center (see Fig. 5.18 (a)). In order to test if the Powell lens is able to make laser sheet, we couple the light from a green test laser into an optical fiber, a collimating lens and the Powell lens sequentially. Figure 5.18 (b) shows the output is a bright green line after the Powell lens, which proves that the Powell lens is working properly. To suppress the stray light, i.e., the part of the incoming laser light reaching the detection system through reflection at windows, electrodes, and the vacuum vessel walls, an anti-reflection coating is applied to the entrance window, a laser collimator is installed, and a stack of razor blades has been employed as a beam dump. In addition, the line generator is enclosed by a light-tight blackened aluminum box so that no background room light enters into the entrance window.

The fluorescence light passes through the $1''$ diameter hole in the central electrode [Fig. 5.18(c)], a glass vacuum window and a C-mount lens with a diameter comparable to the 1-in. O.D. hole. Finally, a Princeton Instruments ICCD-MAX intensified CCD camera captures the fluorescence image digitally. The CCD camera has 16-bit A/D converter with 512×512 pixel resolution, and uses a microchannel plate (MCP) image intensifier fiber-optically coupled to the CCD array. The thermoelectric cooler mounted on the heat removal block and the external fan keep the temperature to -20 °C. In order that the overall detection system has a wide field-of-view (FOV) and covers the entire transverse dimension of the plasma column, a custom-made reentrant viewport [Fig. 5.18(c)] has also been installed.

5.3.2 Signal-to-Noise Ratio Estimation

The fluorescent signal is estimated using the following equation [2]

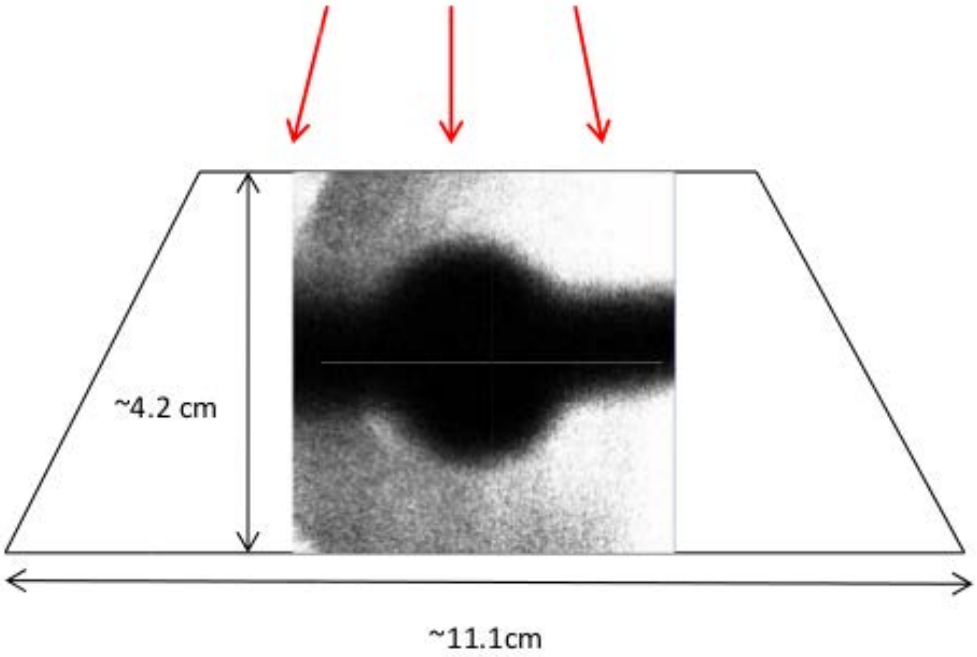

(a) Laser sheet

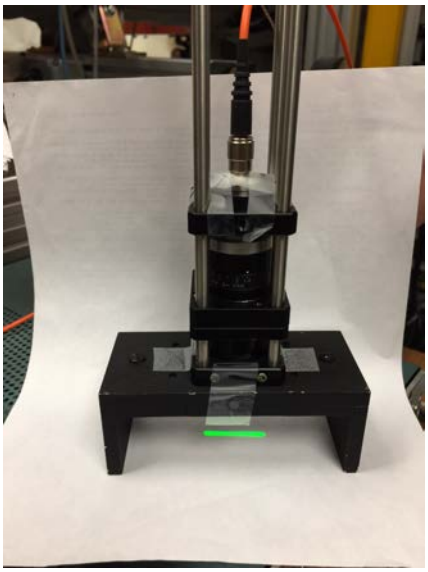

(b) Observation of laser sheet using a test laser

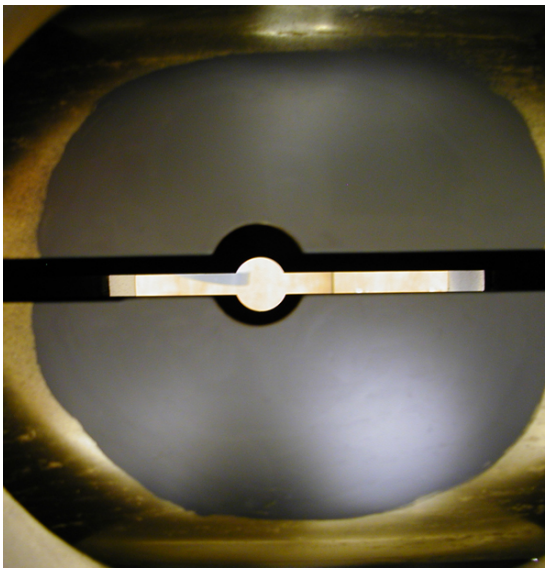

(c) Viewport

Figure 5.18: Initial tests of the laser system showing: (a) the image of the background light including the shape of the laser sheet. (b) display of the laser sheet using a test laser. (c) the viewport from the CCD camera. The dark circle in the image (a) is the inner hole made in the central electrode shown in (c).

$$S \approx \mathrm{n_2 A_{23} V} \frac{\Omega}{4\pi} \eta_{\mathrm{T}} \eta_{\mathrm{Q}} \mathrm{g} \frac{\mathrm{N}_\tau}{\mathrm{N_p}} \tag{5.3}$$

where S is the average number of read-out photoelectrons per pixel, the density of excited state n_2 is assumed radially Gaussian-distributed, A_{23} is the spontaneous transition rate between the excited state and the metastable state, V is the volume from which the signal is collected(assuming a volume of 2.54 mm $\times$ 0.8 mm $\times$ 70 mm), and Ω is the solid angle subtended by the aperture stop in the collection optics. The transition efficiency of the collection optics (glass, filter and lens) η_T is assumed to be 35%, and the quantum efficiency of the intensifier η_Q is about 15%, g is the gain of the CCD camera system, N_τ is the number of pulses and N_p is the number of pixels where photoelectrons are read out.

The major source of background light is the glowing iridium ionizer, which is operated at approximately 1200 °C. To reduce the scattered light from the ion source, the background of the observation path has to appear black. For this purpose, a so-called viewing dump has been installed. In order not to affect the performance of the electrodes, conductive carbon particles (Aquadag) are applied as a coating. This coating reduces the scattered light by two orders of magnitude. The focal length of the lens and the length of the extension tube have been adjusted so that the CCD camera is focused onto the darkest region of the viewing dump.

Another source of noise is the read-out noise from the CCD camera system. For a Princeton Instruments ICCD-MAX intensified CCD camera, that read-out noise, in terms of number of electrons per pixel, is about $1 \sim 2$. The background emission from collisional transitions can be neglected in PTSX. Given another major source of noise, the statistical noise $\sqrt{S}$ is usually much larger than the read-out noise, the signal-to-noise ratio is simplified as $S/\sqrt{S} = \sqrt{S}$. For typical operating parameters PTSX together with the maximum gain of the CCD camera system, the signal-to-noise ratio is estimated to be about 25, which is adequate.

To improve the signal-to-noise ratio, long integration time and high gain are utilized. We can also operate the CCD camera system in a gated mode that allows the CCD camera system to only collect signal when needed, further reducing the background light noise.

5.3.3 Test of the Laser System

The key of the LIF diagnostic is to have a stable pulsed laser output centered at 493.4077 nm. The perfect alignment of the optical components is critical to generating a stable laser output at desired wavelength. The first step is to choose a suitable dye for the dye laser. Coumarin 480 is chosen because it is able to take in the 308 nm pump beam from our excimer laser, but also because its peak wavelength is close to our desired wavelength and the range of wavelength is wide enough to cover our desired wavelength. Note that the detailed peak wavelength and the range of the fluorescence spectrum is depending on the concentration level of the dye. According to the manual, the concentration level of dye in the main dye cell is 1/3 of that in the preamplifier dye cell. The concentration level is fixed at 2.3g/L for the preamplifier dye cell in order that the peak wavelength of the dye fluorescence spectrum in the preamplifier dye cell is centered around 480 nm and the range of the spectrum (460 nm $\sim$ 510 nm) is wide enough to cover the desired wavelength (493.4077 nm). The major diagnostic tool for the laser test discussed in this section is a spectrometer USB2000 from the Ocean Optics. This spectrometer is designed to take in weak signals and in our case, the spectrometer saturates quite often. To verify the fluorescence spectrum of dye in the preamplifier dye cell, an optical fiber is pointed towards the side of the preamplifier dye cell. When the gratings is uncovered, the desired wavelength is selected and be preamplified in the dye cell. Due to the reflection by the dye cell window, some of the the desired laser signal is leaking out of the side window and can be captured by the optical fiber if pointed at the right angle. Figure 5.19 shows the fluorescence spectrum of the dye from the preamplifier dye cell together with the laser signal at the desired wavelength. The peak around 480 nm is the fluorescence peak and the peak near 493 nm is the desired laser signal. It is also noted

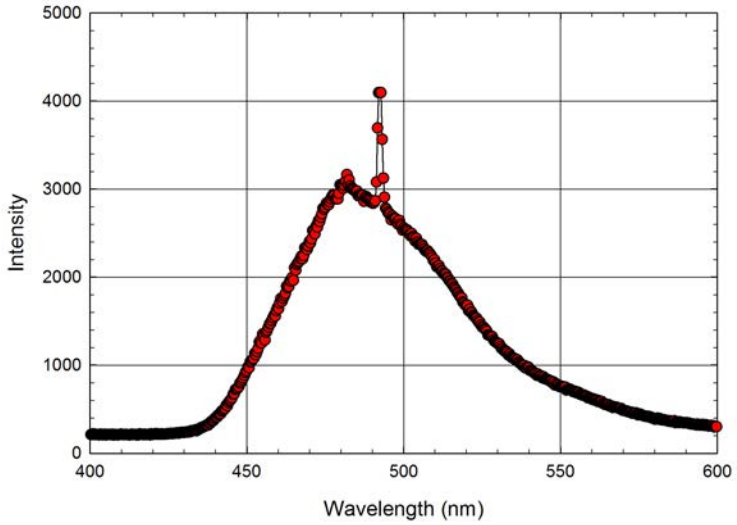

(a) Fluorescence spectrum of the dye from the preamplifier dye cell together with the laser signal at the desired wavelength.

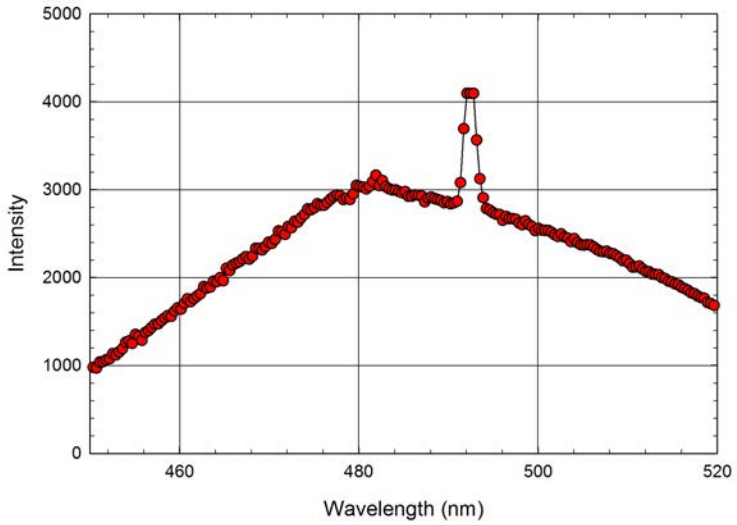

(b) Blowup of Fig. (a) near 480 nm.

Figure 5.19: The fluorescence spectrum of the dye from the preamplifier dye cell is centered around 480 nm and the peak around 493 nm which is saturated is our desired laser signal. The spectrum shows the dye is working properly as expected.

that the peak around 493 nm is saturated which means the real intensity of the laser signal is probably much larger than the fluorescence noise.

To verify that there is desired laser signal, we measured the output right after the preamplifier dye cell before going through the telescope system. We measured the output signal

with and without the grating being blocked. If there is desired laser signal, when the grating is blocked, the desired laser signal will disappear and the whole spectrum of the output signal will be significantly from that measured with the grating unblocked. We chose 493.4077 as our desired wavelength keep in mind that the fluorescence of the dye cell centers around 480 nm. Figure 5.20 shows the output light spectrum right after the preamplifier dye cell with and without the grating being blocked. It is noted that when the grating is open, there is a strong peak near 493.4077 nm, which is our desired wavelength, while there is a small peak near 480 nm, which should be the fluorescence noise from the preamplifier dye cell. When the grating is grating is blocked, the desired laser signal disappeared. The peak near 480 nm is much bigger than when the grating is unblocked. It is noted that both the energy for the desired laser and the energy for the fluorescence come from the pump laser. When no energy goes to the desired laser signal, more energy goes to the fluorescence, making the fluorescence much bigger.

After we verified the laser output in the preamplifier stage, we need to verify the laser output in the main amplifier stage. After all, this is the stage where the laser signal gets significant amplification. Similar to what we did in the preamplifier stage, we measured the output light spectrum right after the main amplifier with and without the grating being blocked. When the grating is unblocked, there is strong peak near 493.4077 nm on the spectrum, while the peak around 480 nm is very small. Since the the desired laser signal is saturated on the spectrum, the real laser signal is at least 10 times stronger than the fluorescence signal. When the grating is unblocked, there is no desired laser signal, and we notice the output light spectrum is a bit different from the fluorescence spectrum from the preamplifier dye cell. There are two close peaks near 480 nm. Since at the main amplifier stage, both the fluorescence spectrums from the preamplifier and the main amplifier stage can be observed, the occurrence of two close peaks is probably due to the different concentration levels of the dye. The dye we used is Coumarin 480, and the fluorescence spectrum of this dye depends on the concentration level. Since the concentration level in the main amplifier

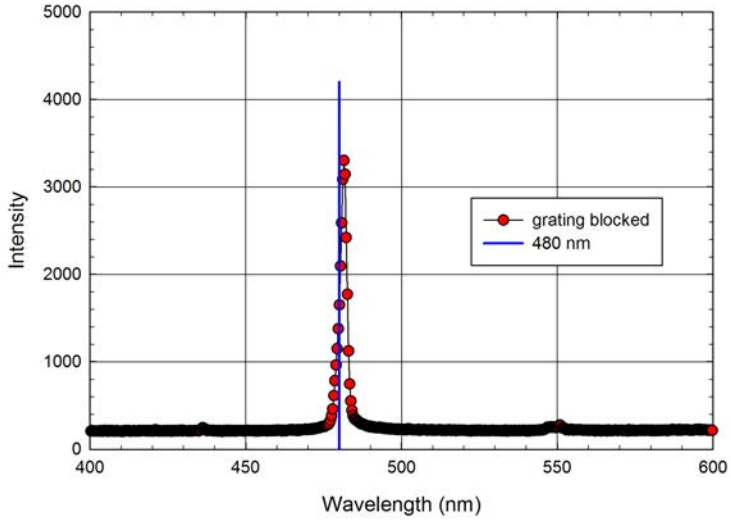

(a) Output light spectrum right after the preamplifier dye cell with the grating blocked.

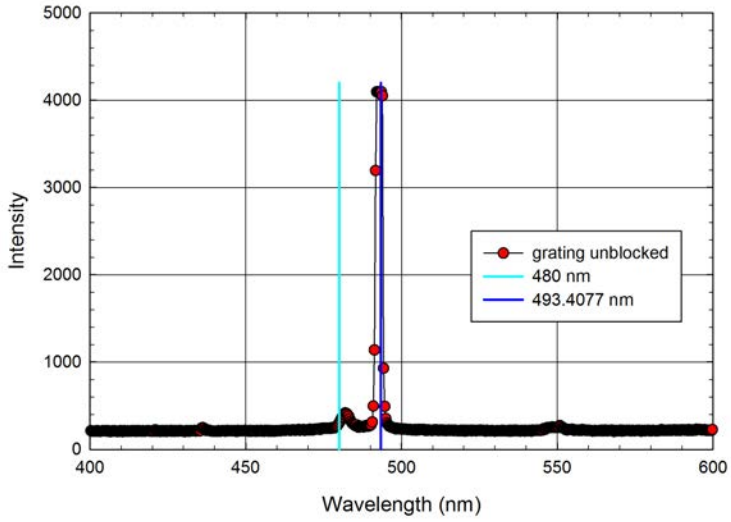

(b) Output light spectrum right after the preamplifier dye cell with the grating unblocked.

Figure 5.20: The output light spectrum right after the preamplifier dye cell differs significantly depending on if the grating is blocked. (a) the grating is blocked, and the desired laser signal disappears, leaving only the fluorescence noise. (b) the grating is unblocked and the desired laser signal is saturated while the fluorescence signal is extremely small. The desired laser signal is at least 10 times stronger than the peak fluorescence signal.

dye cell is only 1/3 of that in the preamplifier dye cell, it is no wonder that the fluorescence spectrums are slightly different.

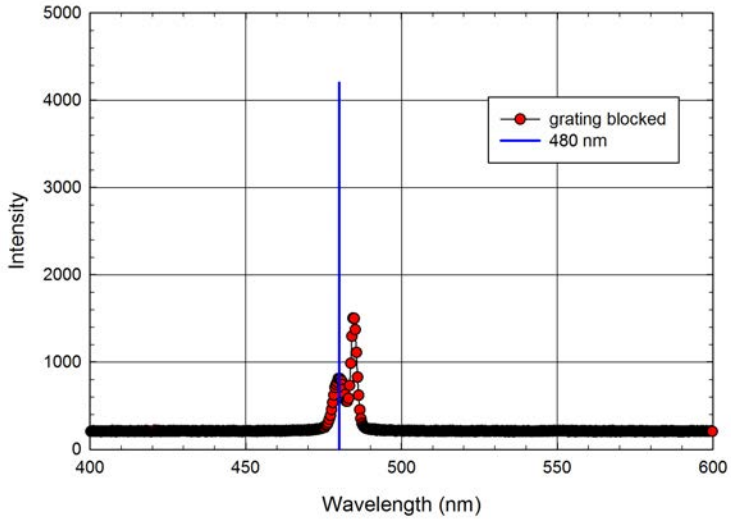

(a) Output light spectrum right after the main amplifier dye cell with the grating blocked.

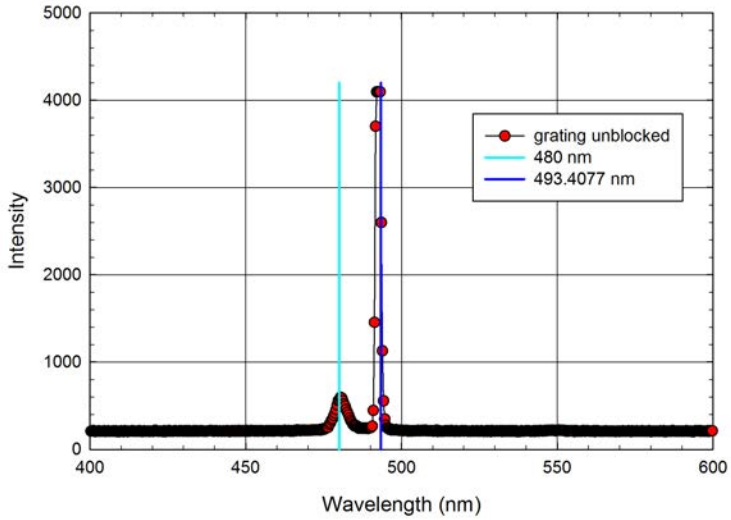

(b) Output light spectrum right after the main amplifier dye cell with the grating unblocked.

Figure 5.21: The output light spectrum right after the amplifier dye cell differs significantly depending on if the grating is blocked. (a) the grating is blocked, and the desired laser signal disappears, leaving only the fluorescence noise. (b) the grating is unblocked and the desired laser signal is saturated while the fluorescence signal is extremely small. The desired laser signal is at least 10 times stronger than the peak fluorescence signal.

The laser signal is coupled into an optical fiber after the main amplifier stage using the coupling system shown in Fig. 5.22 (a) and it travels more than 50 meters before getting the target. The focusing lens has very short focal length (1 cm) to make sure most of the laser beam will be coupled into the fiber before the signal gets too divergent. The optical fiber we used is a step index 0.39 NA TECS-Clad multimode optical fiber shown in Fig. 5.22 (b). The diameter of the silica core of the optical fiber is chosen to be 1 mm to make sure most of the light will be coupled into the fiber. The end of the fiber facing the focusing lens is flat polished and the other end has a FC/PC connector.

The output from the optical fiber should be tested before it is sent into the PTSX chamber. Figure 5.23 shows the laser signal is well preserved during the transmission. Finally, the laser signal from the optical fiber will go through a collimating lens and a Powell lens shown in Fig. 5.24. The laser sheet from the Powell lens enter the PTSX chamber through the glass window below the beam scraper to excite the barium ions. We observed the output after the Powell lens from the dye laser and we did see a bright blue line on a paper. Although we did see a laser sheet coming out of the Powell lens, we were not sure how much the laser pulse energy was because it was very difficult to measure the total energy of a laser sheet.

5.4 LIF Diagnostic in PTSX

The purpose of the LIF diagnostic is to to have a non-destructive diagnostic tool for the charged particle beams and study the beam mismatch, halo formation and etc. While the LIF diagnostic has the potential to be used for measurements of radial density profiles and velocity distribution function [2], the very first step would be reconstructing the radial density profiles. Since we have a stable barium ion source and a working dye laser, we are ready to make them work together and take data. The laser system and the CCD camera are controlled by the external triggering signals. The timing of external triggers is critical since the laser pulse is extremely short (10 ns). The initial tests show that it takes the CCD

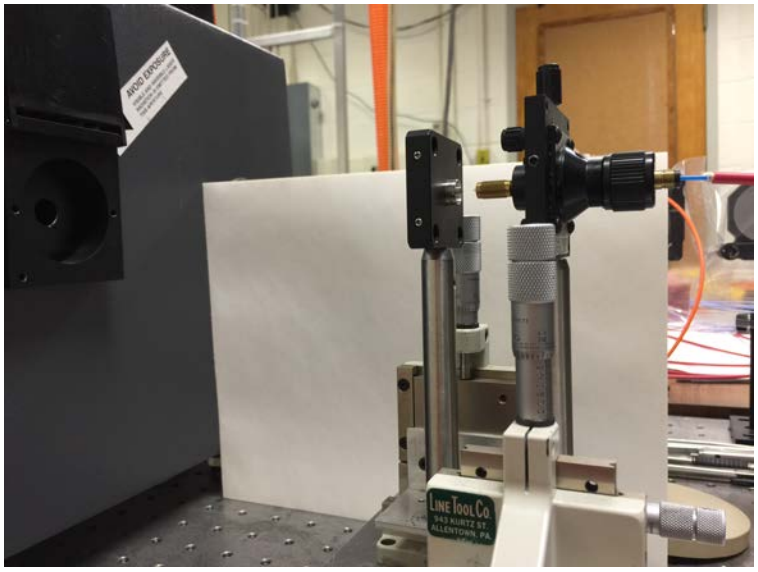

(a)

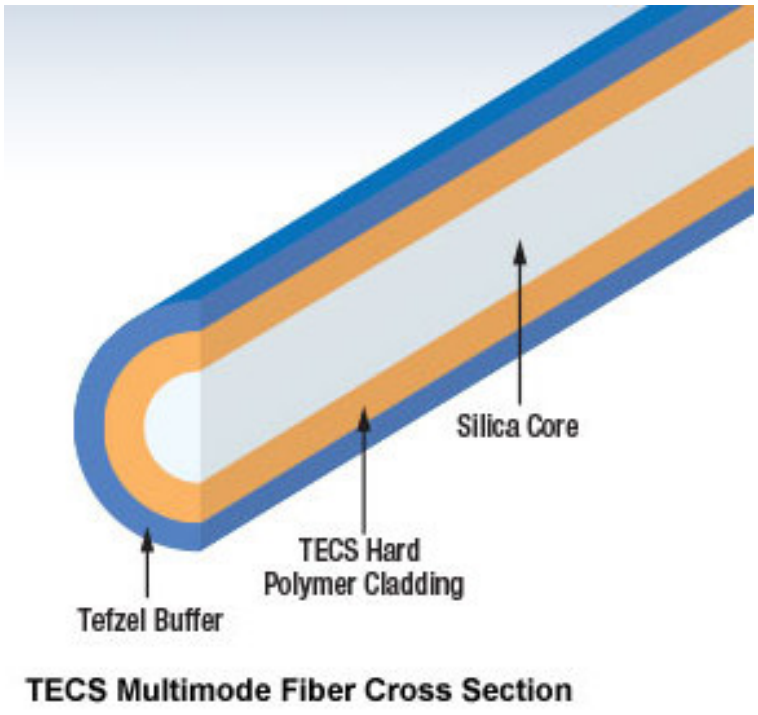

(b)

Figure 5.22: The laser coupling system. (a) The laser beam is focused by a focusing lens with short focal length (1 cm) to a tiny point before entering the optical fiber. The optical fiber has a large numerical aperture (0.39) to make sure even the incident angle of the laser beam is large, it can still be transmitted without significant signal loss. (b) The cross section of the multimode optical fiber. The diameter of the silica core is 1 mm and the numerical aperture is 0.39.

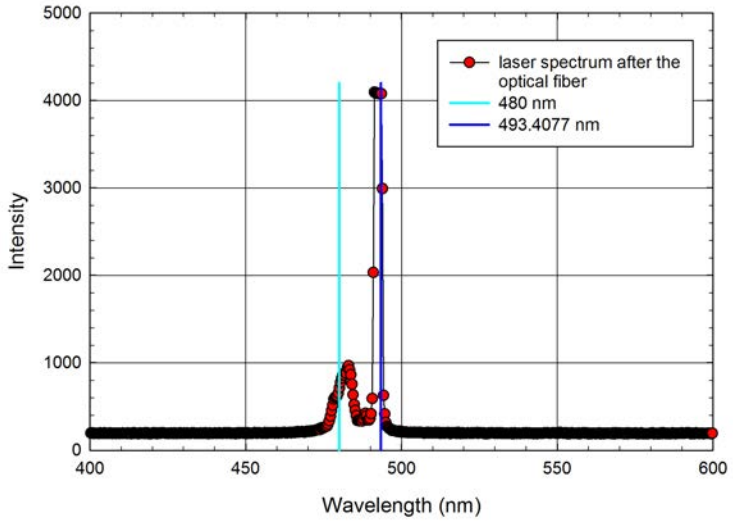

Figure 5.23: The output light spectrum after being transmitted by the optical fiber. The spectrum clearly shows that after being transmitted by the optical fiber, there is still strong desired laser signal, and the fluorescence noise is much smaller compared to the laser signal.

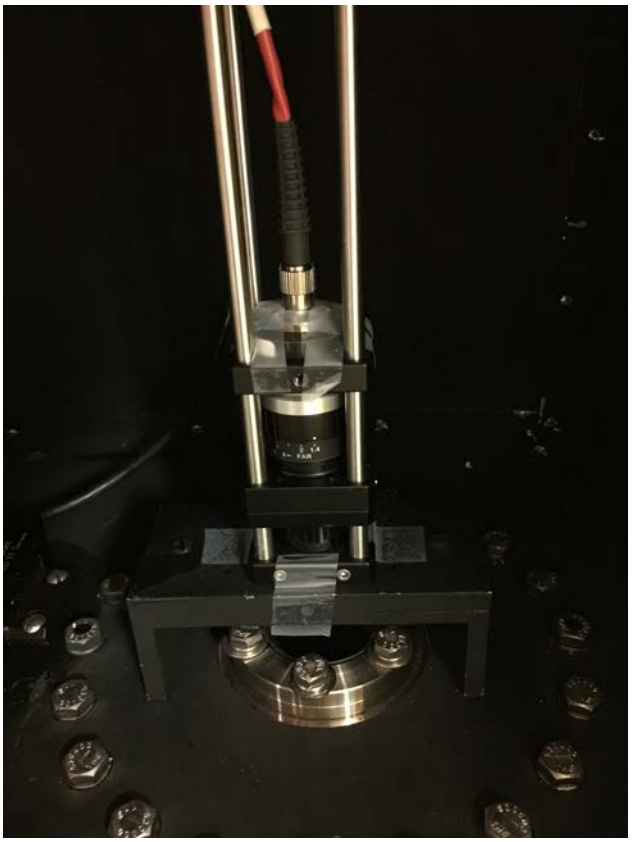

Figure 5.24: The collimating lens and the Powell lens will convert a narrow laser beam into a broad laser sheet.

camera approximately 1 ms to respond to the trigger and get ready to take images, while the laser system has a much faster response. So we allow the camera to be triggered 1 ms ahead of the laser system. The CCD camera is operated in shutter mode and the initial tests showed that the exposure time can be as short as 1 μs to catch the short laser pulse. Theoretically, to minimize the background noise, we could set the exposure time to 1 μs. Practically, we set the exposure time to 10 ms to make sure that we will catch the short laser pulse. The maximum repetition rate is 10 Hz but the CCD camera can operate at most at 2 Hz. So we set the cycle time to be 0.5 s to make sure that the camera have enough time to respond.

Experimental Results

First of all, we need to establish the background noise level. The CCD camera is covered with a black blanket around the lens and the black box where the optical fiber and the Powell lens are mounted is enclosed. In this way, the external stray light is minimized. The background noise is mainly coming from the glowing iridium plate and the reflection of the incident light on the interior surfaces of the PTSX electrodes. The background level is measured with the iridium plate being hot but not allowing any barium ions to enter the PTSX chamber by applying negative bias voltage on the iridium plate. In the mean time, the dye laser is running. In this way, a complete background noise from the glowing iridium plate and the running laser can be captured. The exposure time is set to be 10 ms and the integration time is 50 s. Figure 5.25 (a) shows the accumulated image of 100 shots from the CCD camera. The dark circle in the image is the inner hole made in the central electrode. To obtain the average background level for each shot, we divided this accumulated image by 100. Then in the future, this average background level per short will be subtracted from each incoming shot.

Since the internal linewidth from the dye laser is about 0.003 nm, we need to scan the wavelength near the 493.4077 nm to capture the correct wavelength. Figure **??** shows the

accumulated image of 1000 shots which correspond to 500 s integration time. The background noise is already subtracted for each shot. If there is a strong emission signal from the barium ions decaying from the excited state to the ground state, we should be able to see a series of light belts with different intensities aligned along the horizontal direction. It is because the the radial density profiles are Gaussian distributed, and the light intensity is proportional to the number density. However, we didn't see that pattern from Fig. 5.25 (b), neither did we see the pattern from other images taken at wavelengths near 493.408 nm.

In order to extract meaningful LIF signal from the CCD camera images, we plotted the average line readout from the CCD camera as a function of the distance from the axis. As discussed in Sec. 5.3.1, the CCD camera has 16 bit A/D converter with 512 $\times$ 512 pixel resolution. The distance from the axis is expressed as the number of pixel ranging from 1 to 512 with 256 corresponding to the axis approximately. Figure 5.26 shows the average line output of the background signal and the LIF signals after subtracting the background signal. The wavelength of the input laser was scanned near 493.408 nm at a step of 0.001 nm, in order to compensate the limited linewidth. Figure 5.26 (a) shows the background signal level is very low near the center of the diagnostic area where the barium ions would be. The higher background signal measured away from the center is probably due to the reflection of the input laser from the PTSX electrodes. In Fig. 5.26 (a), the laser signals for various input laser wavelengths, didn't show the bell curve shape corresponding to the radial density profile of the barium ions. Figure 5.26 (b) is a sub-figure of Fig. 5.26 (a), which focuses on the center of the diagnostic area where the barium ions would be. It is quite clear from Fig. 5.26 (b) that no meaningful LIF signal was observed from the CCD camera images. There are a couple of possible reasons why we didn't extract meaningful data from the images. One reason could be the inaccurate wavelength from the dye laser. The wavelength is controlled by a software, and there could be a calibration error. Since the linewidth of the natural transition of the barium ions is extremely small, even a tiny miss-calibration will lead to totally different results. Another reason could be not enough laser power. Although we

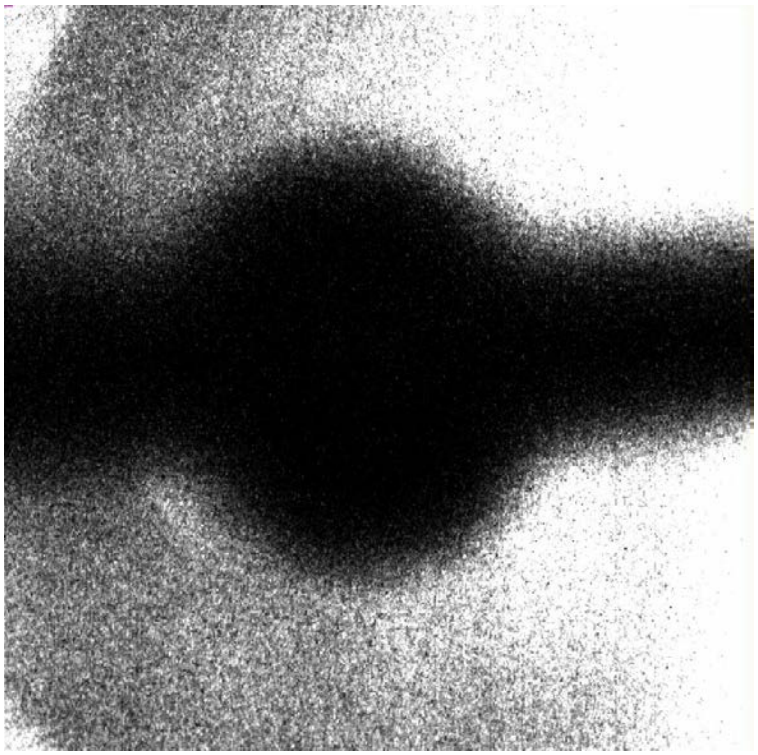

(a)

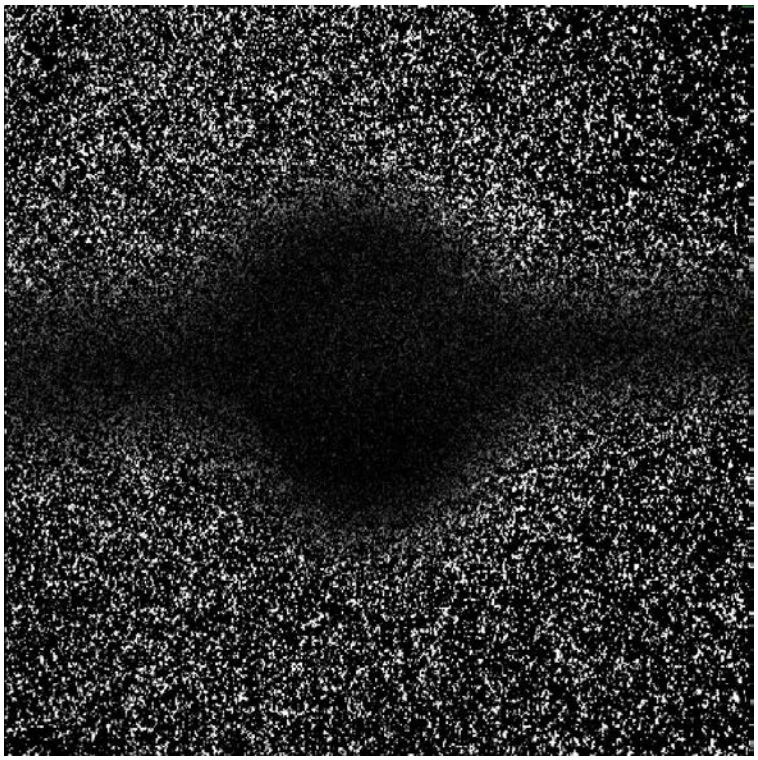

(b)

Figure 5.25: Background and LIF signal images. (a) The background level of the LIF diagnostic. The dark circle in the image corresponds to the inner hole made in the central electrode shown in Fig. 5.18 (c). (b) The image taken at 493.408 nm with background subtracted. The integration time is 500 s. There aren't significantly bright spots in the center of the image.

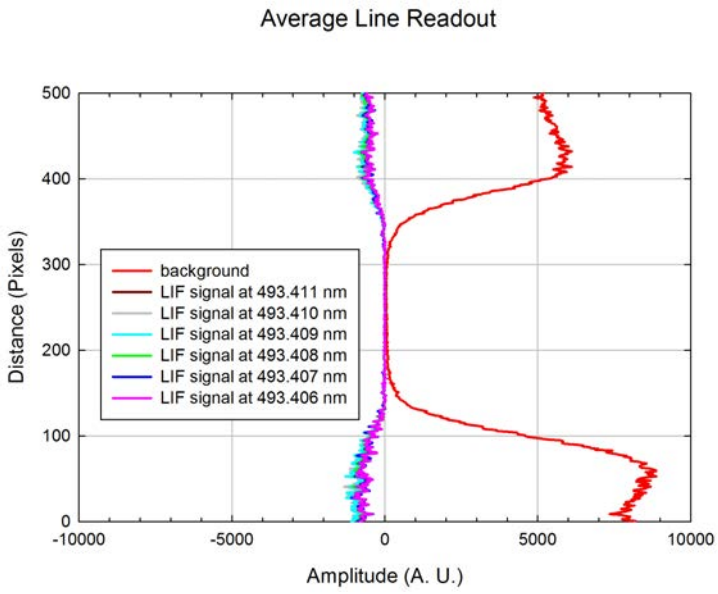

(a)

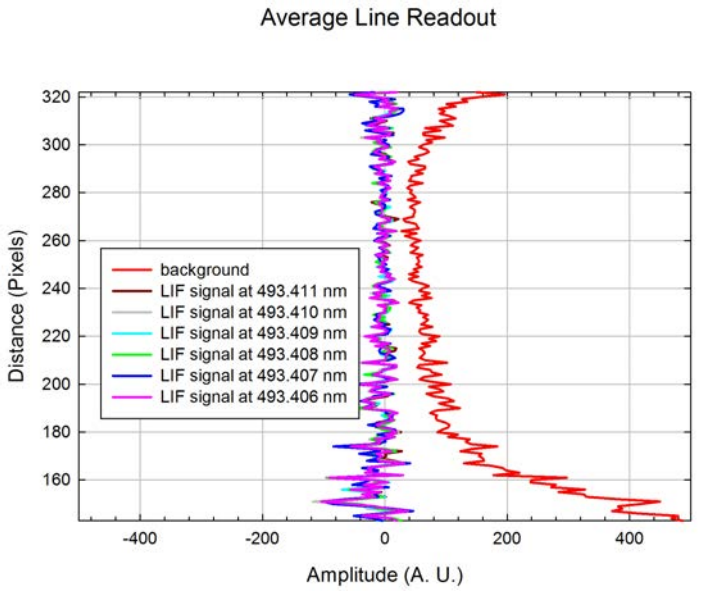

(b)

Figure 5.26: The average line output from the CCD camera. The background signal level near the center is very low, as well as the LIF signal after subtracting the background signal. Fig. (b) is the blow up of Fig. (a) focusing on the center of the image where the barium ions would be. The laser signal didn't show the bell curve shape corresponding to the radial density profile of the barium ions.

did see a bright laser sheet coming out of the Powell lens, we haven't been able to measure the actual output energy due to lack of equipment for measuring pulsed laser energy. It is also possible that the integration time of the CCD camera is not long enough to acquire a stronger LIF signal. Another reason could be the poor alignment of the Powell lens with

respect to the gap between the PTSX electrodes. If the Powell lens is not aligned properly, it is possible that only a small portion of the laser beam goes to the PTSX chamber, resulting a weak signal.

5.5 Summary and Discussion

In this chapter, we talked about the development of the LIF diagnostic. The accompanying barium ion source was developed and tested both independently and in the PTSX chamber. The new barium source is able to be operated for a long period while remaining stable. The excimer pumped dye laser was developed and tested. The experimental results showed that the dye laser was able to produce the laser pulses at the desired wavelength. The Powell lens also seemed to be able to generate a laser sheet to increase the detection volume. The CCD camera was able to capture the laser signal even with 1 μs exposure time. But in the experiment we decided to increase the exposure time to 10 ms to make sure we will catch the signal. Although we haven't been able to reconstruct the radial density profiles yet, we have some ideas about where it could be wrong, and with dedicated effort, we believe the goal of reconstructing the radial density profiles will be achieved in the near future.

Chapter 6

Conclusions and Future Research

Studies of nonlinear dynamics of intense charged particle beams in the Paul Trap Simulator Experiment (PTSX) have been presented in this thesis. Excitation of the quadrupole and dipole modes have been conducted using various external perturbations such as coherent periodic perturbations and random noise. It is demonstrated that the resonances between the collective modes and the external perturbations will cause degradation of charged particle beams and that some effective measures can be taken to prevent these negative effects. As a non-destructive diagnostic, a laser-induced-fluorescent (LIF) diagnostic was developed, as well as the accompanying barium ion source. The initial experiments using LIF technique haven't been able to reconstruct the radial density profiles of the pure ion plasma confined in PTSX.

6.1 Conclusions

In this thesis, several important beam physics topics related to the equilibrium and stability properties of charged particle beams have been explored in the PTSX device. This is achieved based on the equivalence between the physics of charged particle beams and that of nonneutral plasmas. Thanks to the versatility of the PTSX device in controlling the ion

injection and the external focusing fields, the transverse dynamics of charged particle beams with a broad range of characteristic parameters can be studied using the PTSX device.

In **Chapter 4**, excitation of the quadrupole and dipole modes was studied and effects of resonance between the collective modes and the external perturbations on beam equilibrium and stability properties were investigated. It is demonstrated that both quadrupole and dipole modes can be successfully excited and, in order to see a significant resonance effect, not only does the frequency of the external perturbation need to match the mode frequency, but also the spatial structure of the external perturbation must match the collective mode structure. When strong resonance occurs, the resonance serves as an extra energy source which heats the charge bunch and causes transverse expansion. The rms radius is increased due to the expansion and usually particle loss occurs since some particles lose confinement when they drift too far away from the beam center. The collective mode frequency dependence on the normalized intensity parameter $\hat{s}$ as measured from the experimental data was compared to the theoretical prediction using the smooth-focusing model [1]. The smooth-focusing model provides strong explanatory power on the experimental data qualitatively, but there exists quantitative discrepancies between the experimental data and the theoretical predictions. This is probably due to the simplicity of the smooth-focusing model. Particle-in-cell (PIC) simulations were conducted and the simulation results agreed well with the experimental data on quadrupole and dipole modes excitations. Random noise can be viewed as a collection of numerous sine waves at different frequencies under Fourier transformation analysis. The study of machine imperfection effects using random noise indicates that it is the interaction between the collective modes of the charge bunch and the components of random noise at the mode frequencies that causes the strong response of the charge bunch to external random noise. For a specific case of random noise described in Sec. 4.5.2, a rearrangement of the random noise can eliminate the detrimental frequency components at the mode frequencies for the random noise. This discovery has important applications in

making accelerator construction more cost-effective by loosening the field strength tolerance requirements of the magnets.

In **Chapter 5**, a new nondestructive laser-induced-fluorescence diagnostic was described, as well as the development of the accompanying barium ion source. The barium ion source is chosen because barium's optical transition spectrum is more suitable to LIF, as compared to the cesium ion source. It is demonstrated that the new barium ion source is able to provide a stable high-density barium ion source required to perform the LIF measurements. Due to the inherent low signal intensity, strenuous efforts have been made to reduce the background noise. The initial experimental data haven't shown the ability to reconstruct the radial density profiles of the charge bunch confined in the PTSX device. It could be hampered by a low signal-to-noise ratio, or by not selecting the correct wavelength in the dye laser system due to poor calibration of the software.

6.2 Future Research

The PTSX device is a versatile device that can be used study a broad range of nonlinear dynamics topics in charge particle beams propagating in a periodic magnetic transport system. Apart from the topics described in this thesis, several future research tasks can be suggested as follows.

Throughout the thesis, the main experiments on cesium ions have been conducted using a typical normalized intensity $\hat{s} \sim 0.2$, which corresponds to the intense beam characteristic of proton accumulator rings or booster synchrotrons. This is because the charge bunch exhibits long-term stability near $\hat{s} \sim 0.2$. At current settings, higher $\hat{s}$ is achievable but lacks long-term stability. For the next-generation high-intensity accelerators, which has significant space-charge effects, the corresponding normalized intensity parameter $\hat{s}$ is typically much higher than current values. Hence, it is recommended to develop a new ion injection scheme to obtain an initial stable beam equilibrium with higher normalized intensity (e.g., $\hat{s} \geqslant 0.5$).

The typical rms radius at the present settings is larger than the initial beam size. One proposed scheme is to adopt an ion source with larger initial beam size to match the typical rms radius. In that case, we can achiever a higher on-axis charge density, which corresponds to a higher normalized intensity $\hat{s}$.

In this thesis, we use PTSX to simulate dynamics of charged particle beams propagating in the periodic alternating-gradient (AG) magnetic transport systems. The featured magnetic field in this transport system is characterized by Eq. 2.20 and 2.21, and the magnetic field gradient $B'_q(z) = B'_q(z+S)$ has axial periodicity length S. Recently, the study of continuously rotating quadrupole focusing channels has drawn a lot attention and it is expected to be a better focusing system than the conventional AG magnetic transport systems [43]. In the continuously rotating quadrupole focusing channel, the magnetic field gradient is changing continuously in the direction of the beam path (e.g., in z direction). The magnetic field in this case is described as follows [43]

$$\mathbf{B}_q(x,y,z) = B'_q(z)\cos 2\theta_z(y\mathbf{e_x} + x\mathbf{e_y}) - B'_q(z)\sin 2\theta_z(x\mathbf{e_x} - y\mathbf{e_y}) \tag{6.1}$$

where $B'_q(z)$ is the filed gradient defined in Eq. 2.21 and $\theta = 2\pi z/\lambda$. Here, λ is the periodicity of the pole configuration, which is twice the periodicity of the focusing field S, i.e., $\lambda = 2S$. To simulate this magnetic filed configuration, we need two sets of quadrupoles which can be easily achieved by modifying the present PTSX configuration. By further slicing the PTSX cylinders into 8 segments which is described in Fig. 6.1, we can easily simulate the beam dynamics in the focusing channels with continuously rotating quadrupole field. The versatility of the PTSX device has been once again demonstrated.

In **Chapter 5**, we haven't been able to reconstruct the radial density profiles of the pure ion plasmas confined in the PTSX device. There are a couple of areas we can explore to find the solutions. First of all, we have to check the calibration of the software which controls the wavelength selection in the dye laser system. Because the natural linewidth

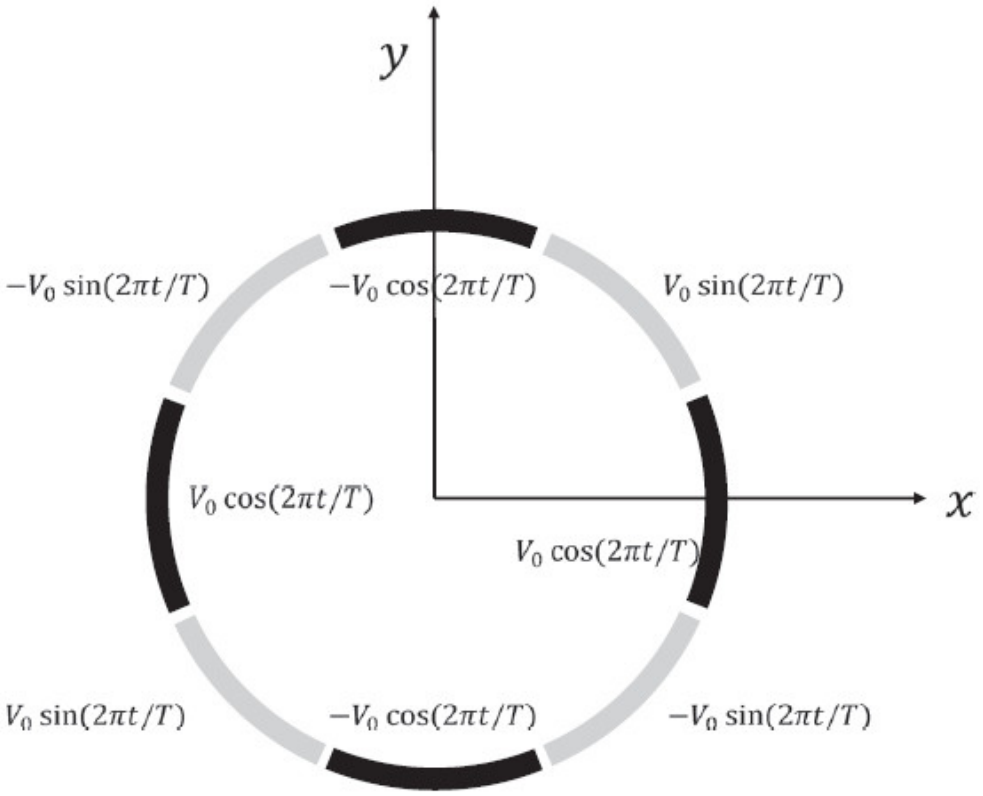

Figure 6.1: Configurations of the linear Paul Trap with eight electrodes to simulate the rotating quadrupole field [43].

of the 493.4077 transition line for the barium ions is extremely small ($\sim 1.0\times10^{-5}$), even a tiny miss-calibration can lead to totally different results. Second of all, we should somehow find a way to check the output laser energy after the laser sheet is coming out of the Powell lens. Although the calculation suggests more than enough energy, we should make sure that is true. Thirdly, we should find a better way to align the Powell lens with respect to PTSX electrodes. The opening between the PTSX electrodes is relatively small and a small mismatch will also lead to undesired results. In order to gain more detailed information of the transverse velocity distribution of the charge bunch, there is much more work to do [88]. With more detailed velocity distribution of the charge bunch, it will provide more insights into improving understanding of the equilibrium and stabilities properties of charge particle beams. This is an important research topic in the future.

Bibliography

[1] R. C. Davidson and H. Qin, *Physics of Intense Charged Particle Beams in High Intensity Accelerators*. Singapore: World Scientific, 2001.

[2] M. Chung, E. P. Gilson, R. C. Davidson, P. C. Efthimion, R. Majeski, and E. Startsev, "Development of laser-induced fluorescence diagnostic for the paul trap simulator experiment," in *Proceedings of the 2005 Particle Accelerator Conference*, p. 2878, IEEE, 2005.

[3] M. Chung, E. P. Gilson, M. Dorf, R. C. Davidson, P. C. Efthimion, and R. Majeski, "Ion injection optimization for a linear paul trap to study intense beam propagation," *Phys. Rev. ST Accel. Beams*, vol. 10, p. 014202, 2007.

[4] M. Chung, E. P. Gilson, M. Dorf, R. C. Davidson, P. C. Efthimion, and R. Majeski, "Experiments on transverse compression of a long charge bunch in a linear paul trap," *Phys. Rev. ST Accel. Beams*, vol. 10, p. 064202, 2007.

[5] M. Chung, E. P. Gilson, R. C. Davidson, P. C. Efthimion, and R. Majeski, "Use of a linear paul trap to study random noise-induced beam degradation in high-intensity accelerators," *Phys. Rev. Lett.*, vol. 102, p. 145003, 2009.

[6] M. Chung, E. P. Gilson, R. C. Davidson, P. C. Efthimion, and R. Majeski, "Experimental investigation of random noise-induced beam degradation in high-intensity accelerators using a linear paul trap," *Phys. Rev. ST Accel. Beams*, vol. 12, p. 054203, 2009.

[7] E. P. Gilson, R. C. Davidson, P. C. Efthimion, R. Majeski, and H. Qin, "The paul trap simulator experiment," *Laser and Particle Beams*, vol. 21, p. 549, 2003.

[8] E. P. Gilson, M. Chung, R. C. Davidson, M. Dorf, P. C. Efthimion, and R. Majeski, "Experimental simulations of beam propagation over large distances in a compact linear paul trap," *Phys. Plasmas*, vol. 13, p. 056705, 2006.

[9] E. P. Gilson, M. Chung, R. C. Davidson, M. Dorf, D. Grote, P. C. Efthimion, R. Majeski, and E. A. Startsev, "Conditions for minimization of halo particle production during transverse compression of intense ion charge bunches in the paul trap simulator experiment (ptsx)," *Nucl. Instrum. and Methods A*, vol. 577, p. 117, 2007.

[10] E. P. Gilson, M. Chung, R. C. Davidson, P. C. Efthimion, and R. Majeski, "Transverse beam compression on the paul trap simulator experiment," *Phys. Rev. ST Accel. Beams*, vol. 10, p. 124201, 2007.

[11] E. P. Gilson, R. C. Davidson, M. Dorf, P. C. Efthimion, R. Majeski, M. Chung, M. S. Gutierrez, and A. N. Kabcenell, "Studies of emittance growth and halo particle production in intense charged particle beams using the paul trap simulator experiment," *Phys. Plasmas*, vol. 17, p. 056707, 2010.

[12] E. P. Gilson, R. C. Davidson, P. C. Efthimion, R. M. E. A. Startsev, H. Wang, S. Koppell, and M. Talley, "Excitation of transverse dipole and quadrupole modes in a pure ion plasma in a linear paul trap to study collective processes in intense beams," *Phys. Plasmas*, vol. 20, p. 055706, 2013.

[13] W. Paul and H. Steinwedel, "Ein neues massemspektrometer ohne magnetfeld," *Z. Naturforsch. A*, vol. 8, p. 448, 1953.

[14] E. P. Gilson, R. C. Davidson, P. C. Efthimion, and R. Majeski, "Paul trap simulator experiment to model intense-beam propagation in alternating-gradient transport systems," *Phys. Rev. Lett.*, vol. 92, p. 155002, 2004.

[15] R. C. Davidson, H. Qin, and G. Shvets, "A paul trap configuration to simulate intense non-neutral beam propagation over large distances through a periodic focusing quadrupole magnetic field," *Phys. Plasmas*, vol. 7, p. 1020, 2000.

[16] R. C. Davidson, *Physics of Nonneutral Plasmas*. Redwood City: Addison-Wesley, 1990.

[17] R. Balescu, *Transport Processes in Plasmas*. Amsterdam: North Holland, 1988.

[18] F. F. Chen, *Plasma Physics and Controlled Fusion*. New York: Plenum Press, 1984.

[19] S. Ichimaru, *Basic Principles of Plasma Physics - A Statistical Approach*. Reading, Massachusetts: Benjamin, 1973.

[20] S. Ichimaru, *Statistical Plasma Physics, Volume I: Basic Principles*. Reading, Massachusetts: Addison-Wesley Publishing Co., 1992.

[21] R. J. Goldston and P. H. Rutherford, *Introduction to Plasma Physics*. Bristol and Philadelphia: Institute of Physics Publishing, 1995.

[22] N. A. Krall and A. W. Trivelpiece, *Principles of plasma physics*. San Francisco: San Francisco Press, Inc., 1986.

[23] D. R. Nicholson, *Introduction to Plasma Theory*. New York: John Wiley and Sons, 1983.

[24] A. Sitenko and V. Malnev, *Plasma Physics Theory*. London: Chapman & Hall, 1995.

[25] T. H. Stix, *Waves in Plasma*. New York: American Institute of Physics, 2006.

[26] J. H. Malmberg and J. S. deGrassie, "Properties of a nonneutral plasma," *Phys. Rev. Lett.*, vol. 35, p. 577, 1975.

[27] G. Dimonte, "Ion langmuir waves in a nonneutral plasma," *Phys. Rev. Lett.*, vol. 46, p. 26, 1981.

[28] M. L. Ott-Rowland, V. Kotsubo, J. Theobald, and G. A. Williams, "Two-dimensioanl plasma resonances in positive ions under the surface of liquid helium," *Phys. Rev. Lett.*, vol. 49, p. 1708, 1982.

[29] S. Hannahs and G. A. Williams, "Plasma wave resonances in positive ions under the surface of liquid helium," *Jpn. J. Appl. Phys.*, vol. 26-3, p. 741, 1987.

[30] C. F. Driscoll, J. H. Malmberg, and K. S. Fine, "Observation of transport to thermal equilibrium in pure electron plasmas," *Phys. Rev. Lett.*, vol. 60, p. 1290, 1988.

[31] F. M. Penning, "Glow discharges at low pressure betweeen coaxial cylinders in an axial magnetic field," *Physica.*, vol. 3, p. 873, 1936.

[32] N. R. Council, *Plasma Science:From Fundamental Research to Technological Applications*. The National Academies Press, 1995.

[33] R. C. Davidson, B. H. Hui, and C. A. Kapetanakos, "Influence of self-fields on the filamentation instability in relativistic beam-plasma systems," *Phys. Fluids*, vol. 104, p. 18, 1975.

[34] T. M. O'Neil, "A confinement theorem for nonneutral plasmas," *Phys. Fluids*, vol. 23, p. 2216, 1980.

[35] R. C. Davidson, "Qusilinear theory of the diocotron instability for nonrelativistic nonneutral electron flow in planar geometry," *Phys. Fluids*, vol. 28, p. 1937, 1985.

[36] H. S. Uhm and R. C. Davidson, "Influence of intense equilibrium self fields on the cyclotron maser instability in high-current gyrotrons," *Phys. Fluids*, vol. 29, p. 2713, 1986.

[37] J. B. Rosenzweig, *Fundamentals of Beam Physics*. New York: Oxford, 2003.

[38] M. Reiser, *Theory and Design of Charged Particle Beams*. New York: Wiley, 1994.

[39] T. Wangler, *RF Linear Accelerators*. New York: Wiley, 1998.

[40] H. Wiedemann, *Particle Accelerator Physics I*. Berlin: Springer, 1999.

[41] C. Chen and R. C. Davidson, "Nonlinear properties of the kapchinskij-vladimirskij equlibrium and envelop equation for an intense beam in a periodic focusing field," *Phys. Rev. E*, vol. 49, p. 5679, 1994.

[42] C. P. Chen, R. Pakter, and R. C. Davidson, "Rigid-rotor vlasov equilibrium for an intense charged-particle beam propagating through a periodic solenoidal magnetic field," *Phys. Rev. Lett.*, p. 225, 1997.

[43] M. Chung, H. Qin, E. P. Gilson, and R. C. Davidson, "Analysis of continuously rotating quadrupole focusing channels using generalized courant-snyder theory," *Phys. Plasmas*, vol. 20, p. 083121, 2013.

[44] R. C. Davidson and C. Chen, "Kinetic description of high intensity beam propagation through a periodic focusing field based on the nonlinear vlasov-maxwell equations," *Part. Accel.*, vol. 59, p. 175, 1998.

[45] R. C. Davidson and H. Qin, "Single-parameter characterization of the thermal equilibrium density profile for intense nonneutral charged particle beams," *Phys. Rev. ST Accel. Beams*, vol. 2, p. 114401, 1999.

[46] R. C. Davidson and H. Qin, "Kinetic description of neutralized drift compression and transverse focusing of intense ion charge bunches," *Phys. Rev. ST Accel. Beams*, vol. 8, p. 064201, 2005.

[47] R. L. Gluckstern, W. H. Cheng, and H. Ye, "Stability of uniform-density breathing beam with circular cross section," *Phys. Rev. Lett.*, vol. 75, p. 2835, 1995.

[48] I. M. Kapchinskij and V. V. Vladimirskij, "Limitations of proton beam current in a strong-focusing linear accelerator associated with the beam space charge," *Proceedings of International Conference on High Energy Accelerators and Instrumentation*, p. 274, 1959.

[49] H. Qin and R. C. Davidson, "Generalized courant-snyder theory and kapchinskij-vladimirskij distribution for high-intensity beams in a coupled transverse focusing lattice," *Phys. Plasmas*, vol. 18, p. 056708, 2011.

[50] H. Qin, R. C. Davidson, M. Chung, and J. W. Burby, "Generalized courant-snyder theory for charged-particle dynamics in general focusing lattices," *Phys. Rev. Lett.*, vol. 111, p. 104801, 2013.

[51] R. C. Davidson, "Nonlinear stability theorem for high-intensity charged particle beams," *Phys. Rev. Lett.*, vol. 81, p. 991, 1998.

[52] R. L. Gluckstern in *Proceedings of the 1970 Proton Linear Accelerator Conference*, (Batavia, IL), p. 811, National Accelerator Laboratory, 1971.

[53] I. Hofmann, L. J. Laslett, L. Smith, and I. Haber, "Stability of the kapchinskij-vladimirskij distribution in long periodic transport systems," *Part. Accel.*, vol. 13, p. 145, 1982.

[54] I. Hofmann and J. Strukmeier, "Generalized three-dimensional equations for the emittance and field energy of high-current beams in periodic focusing structures," *Part. Accel.*, vol. 21, p. 69, 1987.

[55] J. Struckmeier, J. Klabunde, and M. Reiser, "On the stability and emittance growth of different particle phase-space disbribution in a long magnetic quadrupole channel," *Part. Accel.*, vol. 15, p. 47, 1984.

[56] T. S. Wang and L. Smith, "Transverse-longitudinal coupling in intense beams," *Part. Accel.*, vol. 12, p. 247, 1982.

[57] A. Friedman, D. P. Grote, and I. Haber, "Three-dimensional particle simulation of heavy-ion fusion beams," *Phys. Fluids B*, vol. 4, p. 2203, 1992.

[58] S. M. Lund, J. J. Barnard, G. D. Craig, A. Friedman, D. P. Grote, H. S. Hopkins, T. S. Sangster, W. M. Sharp, S. Eylon, T. T. Fessenden, E. henestroza, S.Yu, and I. Haber, "Warm-fluid description of intense beam equilibrium and electrostatic stability proberties," *Nucl. Instrum. and Methods A*, vol. 415, p. 345, 1998.

[59] Q. Qian, W. W. Lee, and R. C. Davidson, "Nonlinear δf-simulation studies of intense ion beam propagation through an alternating-gradient quadrupole focusing field," *Phys. Plasmas Annu. Rev. Fluid. Mech.*, vol. 4, p. 1915, 1997.

[60] H. Qin, R. C. Davidson, and W. W. Lee, "Three-dimensional nonlinear perturbative particle simulations of collective interactions in intense particle beams," *Phys. Rev. ST Accel. Beams*, vol. 3, p. 084401; 109901, 2000.

[61] E. A. Startsev, R. C. Davidson, and H. Qin, "Collective temperature anisotropy instabilities in intense charged particle beams," *Phys. Plasmas*, vol. 14, p. 056705, 2007.

[62] R. C. Davidson, P. Stoltz, and C. Chen, "Intense nonneutral beam propagation in a periodic solenoidal field using a macroscopic fluid model with zero thermal emittance," *Phys. Plasmas*, vol. 4, p. 3710, 1997.

[63] H. Qin, R. C. Davidson, and E. A. Startsev, "Advanced numerical simulations of temperature anisotropy instabilities and collective interaction processes for high-intensity bunched ion beams," *Nucl. Instrum. and Methods A*, vol. 606, p. 37, 2009.

[64] M. Reiser, "Laminar flow equilibria and limiting currents in magnetically focused relativistic beams," *Phys. Fluids*, vol. 20, p. 477, 1977.

[65] S. Strasburg and R. C. Davidson, "Macroscopic description of pressure-anisotropy-driven collective instability in intense charged particle beams," *Phys. Lett. A*, vol. 269, p. 40, 2000.

[66] A. W. Chao, *Physics of Collective Beam Instabilities in High Energy Accelerators*. New York: Wiley, 1993.

[67] A. W. Chao and M. Tigner, *Handbook of Accelerator Physics and Enginerring*. Singapore: World Scientific, 1999.

[68] D. A. Edwards and M. J. Syphers, *An Introduction to the Physics of High Energy Accelerators*. New York: John Wiley & Sons, Inc., 1993.

[69] V. D. Shiltsev, "High energy particle colliders: Past 20 years, next 20 years and beyond," *Physics-Uspekhi*, vol. 55, p. 965, 2012.

[70] M. G. Minty and F. Zimmermann, *Measurements and Control of Charged Particle Beams*. Berlin: Springer, 2003.

[71] P. Strehl, *Beam Instrumentation and Diagnostics*. Berlin: Springer, 2006.

[72] M. Walter, G. Bai, S. Bernal, D. Feldman, T. Godlove, I. Harber, M. Holloway, R. Kishek, P. O'shea, C. Papadopoulous, B. Quinn, M. Reiser, D. Stratakis, C. Tobin, and M. Wilson, "Commissioning of the university of maryland electron ring (umer): Advances toward multiturn operation," *Phys. Plasmas*, vol. 13, p. 056703, 2006.

[73] P. K. Roy, S. S. Yu, S. Eylon, E. Henestroza, A. Anders, F. M. Bieniosek, W. G. Greenway, B. G. Logan, W. L. Waldron, D. L. Vanecek, D. R. Welch, D. V. Rose, R. C. Davidson, P. C. Efthimion, E. P. Gilson, A. B. Sefkow, and W. M. Sharp, "Results on intense beam focusing and neutralization from the neutralized beam experiment," *Phys. Plasmas*, vol. 11, p. 2890, 2004.

[74] B. Beaudoin and R. A. Kishek, "Tune variation and transverse displacement as a diagnostic for profiling beam energy," *Phys. Rev. ST Accel. Beams*, vol. 16, p. 114201, 2013.

[75] B. Beaudoin, I. Haber, R. Kishek, S. Bernal, T. Koeth, D. Sutter, P. OShea, and M. Reiser, "Longitudinal confinement and matching of an intense electron beam," *Phys. Plasmas*, vol. 18, p. 013104, 2011.

[76] A. Friedman, J. Barnard, R. Briggs, R. Davidson, M. Dorf, D. Grote, E. Henestroza, E. Lee, M. Leitner, B. Logan, A. Sefkow, W. Sharp, W. Waldron, D. Welch, and S. Yu, "Toward a physics design for ndcx-ii, an ion accelerator for warm dense matter and hif target physics studies," *Nucl. Instrum. and Methods A*, vol. 606, p. 6, 2009.

[77] R. Kishek, B. Beaudoin, S. Bernal, M. Cornacchia, D. Feldman, R. Fiorito, I. Haber, T. Koeth, Y. Mo, P. OShea, K. P. Rezaei, D. Sutter, and H. Zhang, "The university of maryland electron ring program," *Nucl. Instrum. and Methods A*, vol. 733, p. 233, 2014.

[78] Y. Mo, R. Kishek, D. Feldman, I. Haber, B. Beaudoin, P. O'Shea, and J. Thangaraj, "Experimental observations of soliton wave trains in electron beams," *Phys. Rev. Lett.*, vol. 110, p. 084802, 2013.

[79] R. Abdur, O. O. Gerlits, J. Gan, J. Jiang, J. Salon, A. Y. Kovalevsky, A. A. Chumanevich, I. T. Webter, and Z. Huang, "Novel complex mad phasing and rnase h structural insights using selenium oligonucleotides," *Acta Crystallographica Section D: Biological Crystallography*, vol. 70, pp. 354–361, 2014.

[80] C. L. Armstrong, W. haussler, T. Seydel, J. Katsaras, and M. C. Rheinstädter, "Nanosecond lipid dynamics in membranes containing cholesterol," *Soft Matter*, vol. 10, pp. 2600–2611, 2014.

[81] J. L. Banuelos, G. Feng, P. F. Fulvio, S. Li, G. Rother, S. Dai, P. T. Cummings, and D. J. Wesolowski, "Densification of ionic liquid molecules within a hierarchical nanoporous carbon structure revealed by small angle scattering and molecular dynamics simulation," *Chemistry of Materials*, vol. 26, pp. 1144–1153, 2014.

[82] S. M. Lidia, T. Schenkel, W. G. Greenway, K. Murphy, T. Schenkel, C. D. Weis, and W. L. Waldron, "Commissioning and initial experiments on ndcx-ii," in *Proceedings of the 2013 Particle Accelerator Conference*, p. 108, IEEE, 2013.

[83] P. K. Roy, S. S. Yu, E. Henestroza, S. Eylon, W. L. Waldron, F. M. Bieniosek, M. Leitner, D. Shuman, W. G. Greenway, D. L. Vanecek, J. Coleman, D. Baca, B. G. Logan, D. R. Welch, D. V. Rose, C. Thoma, R. C. Davidson, P. C. Efthimion, I. Kaganovich, E. Gilson, A. B. Sefkow, and W. M. Sharp, "Initial results on neutralized drift compression experiments (ndcx-ia) for high intensity ion beam," in *Proceedings of the 2005 Particle Accelerator Conference*, p. 3856, IEEE, 2005.

[84] E. P. Gilson, "Plasma source development for the NDCX-I and NDCX-II neutralized drift compression experiments." Invited Talk, 18^{th} International Symposium on Heavy Ion Intertial Fusion, Technische Universität and GSI Darmstadt, Germany, August 30 - September 3, 2010.

[85] J. D. Jackson, *Classical Electrodynmaics Third Edition*. Beijing: Wiley, 2001.

[86] H. Okamoto and H. Tanaka, "Proposed experiments for the study of beam halo formation," *Nucl. Instrum. and Methods A*, vol. 437, p. 178, 1999.

[87] N. Kjærgaard and M. Drewsen, "Crystalline beam emulations in a pulse-excited linear paul trap," *Phys. Plasmas*, vol. 8, p. 1371, 2001.

[88] M. Chung, *Studies of Charged Particle Beam Dynamics on the Paul Trap Simulator Experiment Pure Ion Plasma*. PhD thesis, Princeton University, 2008.

[89] J. D. Huba, *NRL Plasma Formulary*. Washington, DC: Naval Research Laboratory, 2004.

[90] E. P. Gilson, R. C. Davidson, P. C. Efthimion, R. Majeski, and H. Qin, "Recent results from the paul trap simulator experiment," in *Proceedings of the 2003 Particle Accelerator Conference*, p. 2655, IEEE Catalog No. 03CH37423C, 2003.

[91] A. S. M. Abramowitz, *Handbook of Mathematical Functions*. National Bureau Standards, 1972.

[92] C. K. Allen and M. Reiser, "Image effects of cylindrical pipes on continuous beams," *Phys. Rev. E*, vol. 54, p. 2884, 1996.

[93] J. Qiang, R. D. Ryne, B. Blind, J. H. Billen, T. Bhatia, R. W. Garnett, G. Neuschaefer, and H. Takeda, "Image-charge effects on the envelope dynamics of an unbunched intense charged-particle beam," *Phys. Rev. ST Accel. Beams*, vol. 6, p. 014201, 2003.

[94] P. M. Lapostolle, "Possible emittance increase through filamentation due to space charge in continuous beams," *ieeetns*, p. 1101, 1971.

[95] F. J. Sacherer, "Rms envelope equations with space charge," *IEEE Trans. Nucl. Sci.*, vol. NS-18, p. 1105, 1971.

[96] Q. Qian, *Nonlinear Dynamics of an Intense Nonneutral Ion Beam Propogating through an Alternating Gradient Focusing Lattice*. PhD thesis, Princeton University, 1995.

[97] E. D. Courant and H. S. Snyder, "Theory of the alternating-gradient synchrotron," *Annals of Physics*, vol. 3, p. 1, 1958.

[98] M. Reiser, "Free energy and emittance growth in nonstationary charged particle beams," *J. Appl. Phys.*, vol. 70, p. 1919, 1991.

[99] L. Friedland, "Spatial autoresonance:enhancement of mode conversion due to nonlinear phase locking," *Phys. Fluids B*, vol. 4, p. 3199, 1992.

[100] J. R. Pierce, "Rectilinear electron flow in beams," *J. Appl. Phys.*, vol. 11, p. 548, 1940.

[101] S. Humphries, *Charged Particle Beams*. New York: Wiley, 1990.

[102] E. P. Gilson, M. Chung, R. C. Davidson, P. C. Efthimion, R. Majeski, and E. A. Startsev, "Simulations of long-distance beam propagation in the paul trap simulator experiment," *Nucl. Instrum. and Methods A*, vol. 544, p. 171, 2005.

[103] Keithley, *Modeel 6514 System Electrometer Instruction Manual*. Cleveland: Keithley Instrument, 1998.

[104] Keithley, *Low Level Measurements Handbook*. Cleveland: Keithley Instrument, 2004.

[105] R. C. Davidson, "Three-dimensional kinetic stability theorem for high-intensity charged particle beams," *Phys. Plasmas*, vol. 5, p. 3459, 1998.

[106] R. C. Davidson, H. Qin, P. H. Stoltz, and T. S. Wang, "Kinetic description of electron-proton instability in high-inensity proton linacs and storage rings based on the vlasov-maxwell equations," *Phys. Rev. ST Accel. Beams*, vol. 2, p. 054401, 1999.

[107] R. C. Davidson and H. S. Uhm, "Influence of finite ion larmor radius effects on the ion resonance instability in a nonneutral plasma column," *Phys. Fluids*, vol. 21, p. 60, 1978.

[108] S. M. Lund and R. C. Davidson, "Warm-fluid description of intense beam equilibrium and electrostatic stability proberties," *Phys. Plasmas*, vol. 5, p. 3028, 1998.

[109] H. S. Uhm and R. C. Davidson, "Low-frequency flute perturbations in intense nonneutral electron and ion beams," *Phys. Fluids*, vol. 23, p. 1586, 1980.

[110] C. L. Bohn and I. V. Sideris, "Fluctuations do matter: Large noise-enhanced halos in charged-particle beams," *Phys. Rev. Lett.*, vol. 91, p. 264801, 2003.

[111] F. Gerigk *Phys. Rev. ST Accel. Beams*, vol. 7, p. 064202, 2004.

[112] J. Qiang, R. D. Ryne, B. Blind, J. H. Billen, T. Bhatia, R. W. Garnett, G. Neuschaefer, and H. Takeda, "Mott electron polarimetry," *Nucl. Instrum. and Methods A*, vol. 457, p. 1, 2001.

[113] P. S. Yoon, W. Chou, and C. L. Bohn, "Simulations of error-induced beam degradation in fermilab's booster synchrotron," in *Proceedings of the 2005 Particle Accelerator Conference, Knoxville, Tennessee*, (Piscataway, NJ), p. 117, IEEE, 2005.

[114] M. Chung, E. P. Gilson, R. C. Davidson, P. C. Efthimion, R. Majeski, and E. A. Startsev, "Laser-induced fluorescence diagnostic of barium ion plasmas in the paul trap simulator experiment," *Nucl. Instrum. and Methods B*, vol. 544, p. 514, 2005.

[115] M. Chung, E. P. Gilson, R. C. Davidson, P. C. Efthimion, and R. Majeski, "Initial density profile measurements using a laser-induced fluorescence diagnostic in the paul trap simulator experiment," in *Proceedings of the 2007 Particle Accelerator Conference*, p. 3666, IEEE, 2007.

[116] T. W. Koerber, M. H. Schacht, K. R. G. Hendrickson, W. Nagourney, and E. N. Fortson *Phys. Rev. Lett.*, p. 143002.

[117] I. Langmuir and K. H. Kingdon, "A theory of vortex merger," *Proc. R. Soc. Lond. A.*, vol. 107, p. 61, 1925.

[118] R. G. Wilson and G. R. Brewer, *Ion Beams*. New York: Wiley, 1973.

[119] M. Kaminsky, *Atomic and Ionic Impact Phenomena on Metal Surfaces*. Berlin: Springer-Verlag, 1965.

[120] K. Muraoka and M. Maeda, *Laser-Aided Diagnostics of Plasmas and Gases*. Bristol and Philadelphia: Institute of Physics Publishing, 2001.